Hydrocarbon Lakes on Titan and Their Role in the Methane Cycle

Thesis by

Alexander G. Hayes

In Partial Fulfillment of the Requirements

for the Degree of

Doctor of Philosophy

California Institute of Technology

Pasadena, California

2011

(Defended April 4th, 2011)

I dedicate this thesis to the next generation of professional armchair explorers.

Acknowledgements

Over the course of the past decade it has been my unbelievably good fortune to have been welcomed into the science teams of two planetary spacecraft missions and have acess to three more. As an explorer at heart, I have savored every moment of this time and recognize that is was only possible due to the generosity and intellectual guidance of a great number of people along the way.

First, I would like to thank Steve Squyres and Jim Bell of Cornell University. Steve introduced me to the field of planetary science and, despite my ~~arrogance~~ naivety, offered me a job on his science team that ultimately made me realize my passion for planetary exploration. Jim handed over the keys to the camera instruments on the Mars Exploration Rovers (MER) and let me run wild. Similar gratitude goes out to the remainder of the MER science team, most notably Ken Herkenhoff and Phil Christensen, who provided me with access to their instruments as well. The camaraderie I experienced within the MER science team during my time at Cornell and JPL motivated my decision to pursue a career in planetary science.

Upon entering the doctoral program at Caltech, I found both an intellectual mentor and friend in my advisor Oded Aharonson. Oded challenged me from day one, and I am ever grateful for his guidance and leadership. Perhaps I am most indebted to Oded for

his treatment of me as colleague, not a student, forcing me to develop the skills needed as a professional scientist. Over the course of my doctoral career, Oded ensured that every conceivable resource was at my feet before I even realized I needed it. Furthermore, Oded's intellectual criticism help me develop the invaluable ability to strip problems down to their fundamental questions. I can only hope that he has enjoyed and benefited from our frequent intellectual debates as much as I have.

I also wish to thank the remainder of my thesis committee at Caltech. Most notably, my fellowship advisor Charles Elachi. Charles provided unrestricted access to the Cassini RADAR instrument and ensured that every door I came across was not only unlocked, but held open so I could venture in and out at my leisure. John Grotzinger, my co-advisor, was an intellectual force who introduced me to the world of geology and sedimentology. George Rossman provided countless hours of intellectual discussion that transcended the field of mineral spectroscopy and reached life in general. I am honored to consider him a friend. David Stevenson excited an academic rigor in my work for which I will always be grateful. Finally, Andy Ingersoll was ever patient and vigilant in his quest to teach me the importance of simplicity. I must also thank the GPS staff, most notably Nora Oshima and Scott Dungan, for their assistance with a myriad of technical and administrative difficulties.

The camaraderie and fellowship that I experience among the MER science team can only be matched by that which I felt as part of the Cassini RADAR Science Team (CRST). The members of the CRST welcomed me with open arms and provided significant support for all of the work presented in this thesis. Specifically, I would like to thank my collaborators Steve Wall, Jonathan Lunine, Randy Kirk, Ralph Lorenz, Elizabeth Turtle, Rosaly

Lopes, Michael Janssen, Larry Soderblom, Howard Zebker, Jason Barnes, Phil Callahan, Alice Le Gall, Lauren Wye, Karl Mitchell, and Philippe Paillou. Your contributions are directly reflected in the both the quality and style of my work. My gratitude for your support is surpassed only by my regret at not having the space to adequately thank you in this document. I look forward to our future collaborations.

Despite the significant support I have enjoyed from both my advisors and collaborators, my professional development would have be woefully inadequate were it not for daily interactions with fellow graduate students and friends. Kevin Lewis, Alejandro Soto, Aaron Wolf, and Margarita Maranova have acted as both technical advisors and psychological counselors. I only hope that I have helped you as much as you have helped me. I must also thank my friend, confidant, and gym partner Troy Hudson and his successor Konstantin Batygin. Jason Soderblom and Jascha Sohl-Dickstein have been with me since Cornell and I am ever-grateful for their support. I also thank Wes Watters, Antoine Lucas, Ajay Limaye, Meg Rosenburg, Megan Schwamb, and Lauren Edgar for intellectually stimulating collaborations. If we continue working together as we have, I am confident that we will take the field of planetary science by storm.

Most importantly, I must thank my family for their unyielding support. My parents, Al and Mariann, have nurtured my academic pursuits since birth and always pushed me to accomplish more than I thought possible. My uncle, Joseph, acted like a second father and can be credited with invigorating my intellectual curiosity.

Finally, my wife Lindsey has been my partner in all things, and I can think of no one better with whom to share both the joys of success and lessons of failure. She has been ever patient with me during this process and vigilant in her quest to remind me of the things that matter most; The best of example of this being our daughter, Noelle Marie.

In closing, I reiterate my thanks to everyone who has supported me during this journey. I hope to emulate your support and encouragement to others during the course of my career. In this respect, I remember Steve Squyres' response whenever I thanked him for a particular research opportunity:

> "Don't thank me, just make sure you do it for someone else when you find yourself in my position."

Abstract

Saturn's moon Titan is the only extraterrestrial body currently known to support standing bodies of liquid on its surface and, along with Earth and Mars, is one of only three places that we know to posses or have possessed an active hydrologic cycle. Understanding the nature of Titan's hydrologic system will teach us about the history of volatile compounds across the solar system and help define Earth's place within it. Titan's hydrologic cycle represents a simpler version of Earth's water cycle, lacking an ocean as a global sink of liquid and heat, and acts as a model for the evolution of planets around other stars, as its methane-based system may be more common than Earth's water-based system.

This thesis combines several studies related to Titan's hydrologic system, particularly focusing on the role of lacustrine deposits. Following an introduction that discusses Titan's place in the solar system and the importance of studying its methane cycle, chapter two describes the lakes' geographic distribution and models interaction with a porous regolith. The chapter also discusses the implications of a hemispheric asymmetry in lake distribution, which has been attributed to an asymmetry in the intensity of Titan's seasons. The evolution of the orbital parameters that generate this asymmetry provide a mechanism for transferring not only methane, but also less volatile species such as ethane, from pole to pole over tens of thousands of years.

Chapter three discusses lake properties through an examination of Ontario Lacus, the largest lake in Titan's southern pole. The complex dielectric properties of Ontario's near-shore region are derived through a combined analysis of radar altimetry and backscatter. The analysis is performed within multiple regions around Ontario's shore, producing a near-shore bathymetry map. The results of this study are then used to measure seasonal variation in chapter four. Shoreline recession at Ontario Lacus and smaller lakes which disappeared between repeat observations suggest an average meter-per-year loss rate between southern summer solstice and autumnal equinox. These observations demonstrate that Titan's surface plays an active role in its methane cycle and can be used to describe the evolution of its hydrologic system.

Contents

List of Figures

List of Tables

List of Acronyms

BAE British Aerospace Engineering Systems

CI Confidence Interval

CRST Cassini RADAR Science Team

DEM Digital Elevation Model

DTM Digital Terrain Model

ESA European Space Agency

ExM Exponential Attenuation Model

GCM Global Circulation Model

HiSAR High Altitude Synthetic Aperature Radar

ISS Imaging Science Subsystem

JGR Journal of Geophysical Research

JPL Jet Propulsion Laboratory

LM Linear Mixing Model

LNG Liquid Natural Gas

MER Mars Exploration Rover

NASA National Aeronautics and Space Administration

NE Noise Equivalent

PWA Permittivity, Waves, and Altimetry

QS Model Quasi-Specular Backscatter Model

RADAR Radio Detection and Ranging

RH Relative Humidity

RMS Root-Mean-Square

RSS Radio Science Subsystem

SAR Synthetic Aperture Radar

SAR-Topo Synthetic Aperture Radar Topography

SLD Shoreline Development

SNR Signal-to-Noise Ratio

USGS U.S. Geological Survey

VIMS Visual and Infrared Mapping Spectrometer

Chapter 1

Introduction: Exploring Lakes on Titan

Originally published in

Hayes, A. G. Exploring Lakes on Titan. Astronomy Beat, Astronomy Society of the Pacific, 20, September 2010

Picture yourself standing at the shoreline of lake. In the calm water, you see a mirror like reflection of the sky just before it begins to rain. The surrounding terrain contains a collection of similar lakes, some with long meandering channels flowing into them. Now let the surrounding vegetation disappear, leaving behind a landscape you find in the rocky deserts of southern Arizona. The temperature is dropping too, all the way down to a bone-chilling −288°F (95 K). The lake surface is now reflecting a hazy orange sky. The air around you feels thicker, although you yourself feel lighter, courtesy of reduced gravity. Lastly the rain drops are falling slower and are bigger than normal, splashing large amounts liquid every time one impacts your hand. If you can picture all of this, welcome to Saturn's moon, Titan. The ground you are standing on is a porous mixture of broken up water ice and organic particulates. The liquid in the lake is not water, but a combination of methane, ethane, and other hydrocarbons you might find in your car's gas tank. While the surrounding air is nitrogen based like Earth, there are no traces of oxygen.

Titan is the only extraterrestrial body currently known to support standing bodies of liquid on its surface. It is also a world of intriguing mysteries, with a history of presenting more questions than answers since its discovery by the Dutch astronomer Christiaan Huygens in 1655 [Huygens, 1659]. The most pressing of these questions arose when a dense atmosphere was suggested by Spanish astronomer Josep Comas Sola, who observed limb darkening on Titan in 1903 [Sola, 1904]. Confirmations of Sola's observations came from the spectroscopic discovery of gaseous methane by Gerard Kuiper in 1944 [Kuiper, 1944]. Kuiper's discovery led to even more questions as methane is destroyed by ultraviolet solar photons, cosmic rays, and magnetospheric particles by photolysis in the upper atmosphere. The continued presence of methane in Titan's atmosphere suggests an active process replenishing what has been lost over the age of the solar system.

Pioneer 11 obtained the first close-up image of Titan in 1979, proving without a doubt that it has a thick atmosphere [Gehrels et al., 1980]. To investigate further, the trajectory of the Voyager I spacecraft was modified so that it could make a close encounter with Titan in 1980 [Smith et al., 1981]. Through radio occultation, Voyager was able to determine the surface pressure and temperature at 1.5 bars and 95 K [Lindal et al., 1983]. These results were exciting because, for a methane mixing ratio of a few percent at the surface [Hunten, 1978], they place methane's partial pressure near its triple point. Thus, like water on Earth, solid, liquid, and gaseous methane can coexist in Titan's environment. Ethane, which is the main product of methane photolysis, is also a liquid under these conditions. Unfortunately, the visible cameras onboard Voyager were unable to penetrate Titan's thick atmosphere (Figure 1.1). So, while we knew liquid methane and ethane were raining out and stable on

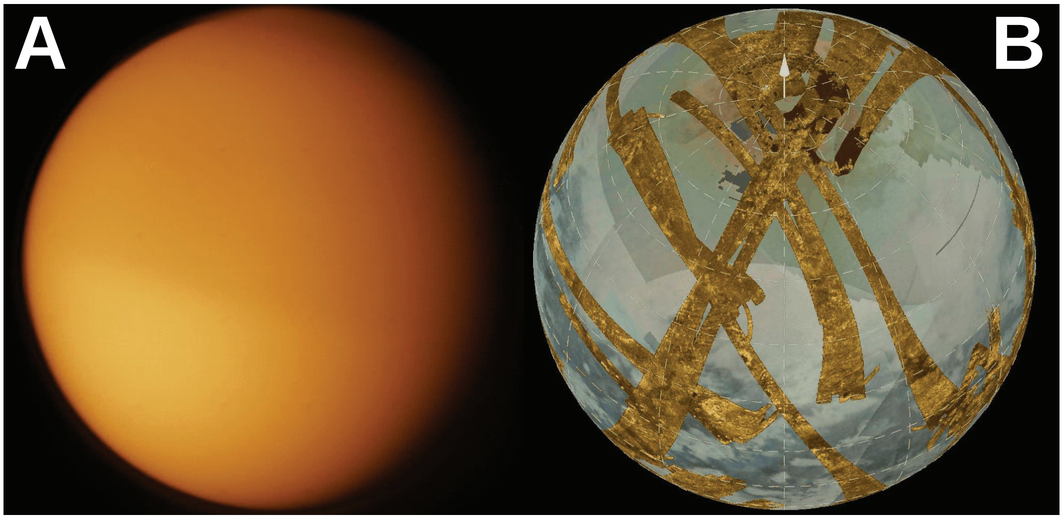

Figure 1.1: Images of Titan obtained by the Voyager (A) and Cassini (B) spacecrafts. Voyager's camera could not see through the opaque atmosphere. The Cassini image is a mosaic of RADAR swaths, shown in false color, on top of ISS and VIMS global mosaics. The RADAR swaths are long and thin because Cassini is in orbit around Saturn, not Titan.

the surface, we could not see how they were distributed.

Prompted by the exciting results of the Voyager mission and the nearly two decades of ground-based imaging campaigns which followed, NASA/ESA launched the Cassini/Huygens mission to Saturn in 1997. In order to penetrate Titan's thick atmosphere, Cassini is equipped with a Ku-band radar capable of obtaining images of the surface at a scale of 300 meters (Figure 1.1). Cassini's instrument suite also inlcudes the Imaging Science Subsystem (ISS) and Visual and Infrared Mapping Spectrometer (VIMS), which are camera systems that operate at infrared wavelengths. While these instruments can see down to the surface by utilizing gaps in the methane absorption spectrum, their resolution (500 m to 15 km) is limited by atmospheric scattering.

The RADAR discovered evidence for liquid hydrocarbon lakes in Titan's north polar region during a flyby in July 2006 [Stofan et al., 2007a]. The work presented in this thesis

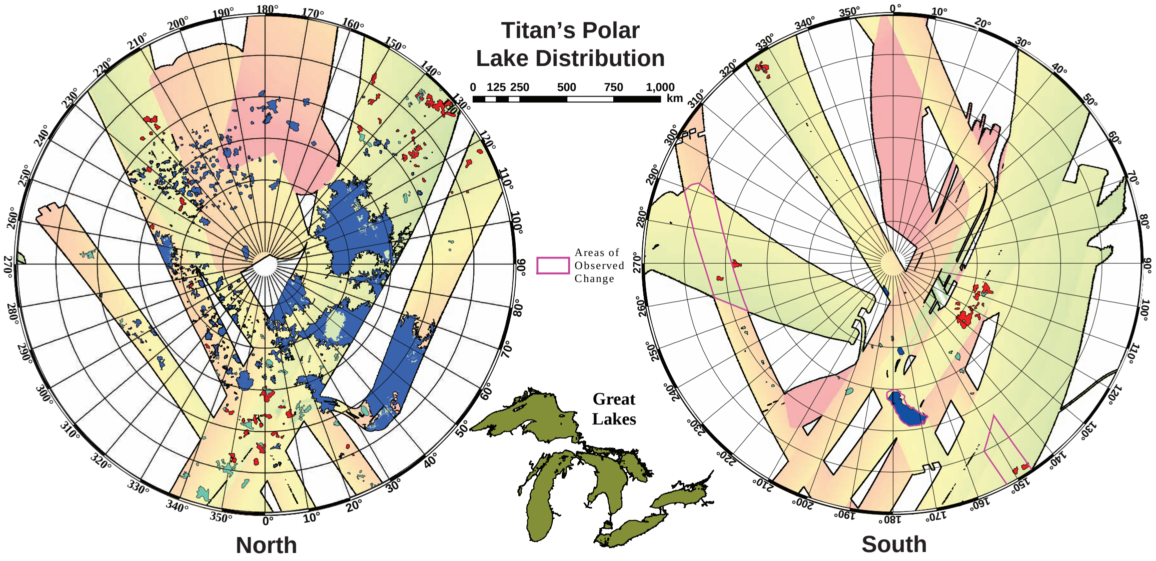

Figure 1.2: Distribution of lakes on Titan poleward of 60°. Filled lakes are blue and cyan while empty lakes are red. Background color corresponds to incidence angle during data acquisition. Note the outline of the Earth's Great Lakes for scale. Areas where changes have been observed are outlined in magenta. The details of the lake distribution is presented in chapter 2.

began when the RADAR Team leader, Dr. Charles Elachi, visited Caltech and unrolled a twenty foot long by two foot wide print out of the July 2006 radar swath down a first-floor hallway in South Mudd Laboratory. Dr. Elachi, Professor Oded Aharonson, and I all took off our shoes and walked around on the image, pointing out various geologic features. Thinking back on it, you could argue that we were the first scientists to walk on the surface of Titan. Between September 2006 and April 2007 the radar obtained an additional five images of Titan's north polar region, covering more than half of the area poleward of 60°N [Hayes et al., 2008a].

For the next several months, we mapped hundreds of lakes found in the radar data and discovered evidence for multiple classes which spanned the range of observed morphologies on Earth (Figure 1.2). This research is presented in chapter 2 of this thesis. Polygonal

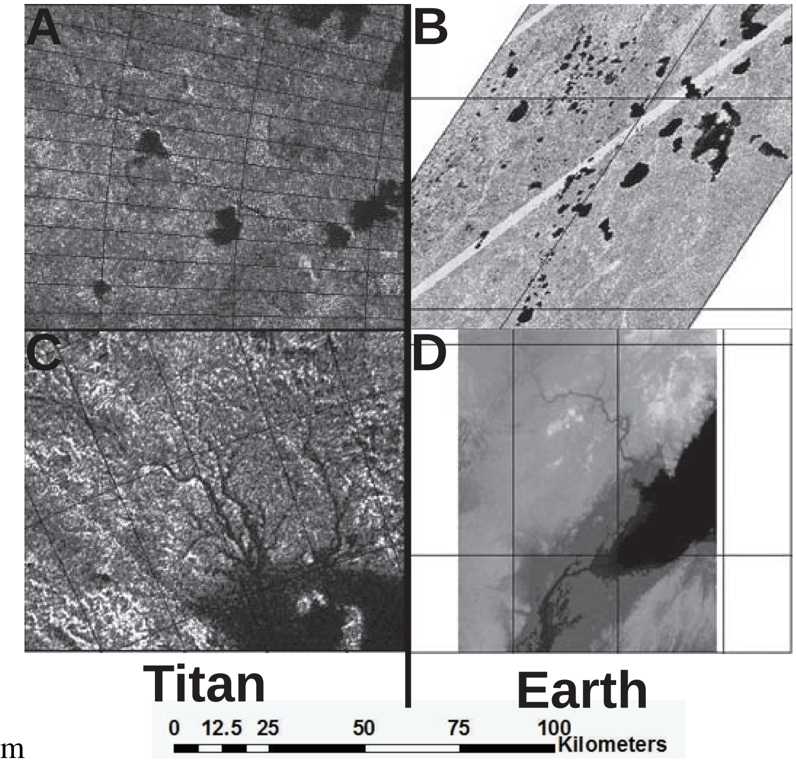

mm

Figure 1.3: Radar images of lakes on Titan taken by the Cassini RADAR (Panels A and C) and Earth taken during the Shuttle Radar Topography Mission (Panels B and D). Panels A and B are examples of seepage lakes while panels C and D are examples of lakes in runoff dominated terrain. Panel B is from the Everglades region of Florida and panel D is from northern Minnesota.

lakes with complex shorelines and associated channels were similar to terrestrial drainage lakes you might expect to see in northern Minnesota (Figure 1.3CD). Lakes with comparatively smooth and distinct shorelines and no associated channels were consistent with seepage lakes interacting with a local groundwater system, like you might see in the Everglades region of Florida (Figure 1.3AB). The largest lakes were found to be similar in size to the Great Lakes (Figure 1.2). When coupled with observations of longitudinal dunes near the equator, Titan was turning out to be a strange, yet familiar, place whose surface was dominated by the same geological processes we see here on Earth, even though the material and thermal conditions are vastly difference.

While we had a good picture of the north polar region by spring 2007, there was very little radar data available in the south. There were animated discussions within the science team, throughout 2007, regarding predictions for the density of lakes in the south. In the end the south was found to contain fewer lakes, with liquid covering a total surface area twenty-five times smaller than in the north. However, the reasons for this asymmetric distribution were not those commonly predicted, as the effect was too extreme to be explained by seasonal variation alone. In Aharonson et al. [2009], we suggested that this dichotomy is a result of non-symmetric seasons inherent to Titan's orbit. The details of this theory are explained in Chapter 2, Section 5, of this work.

The peak solar flux in the south is about twenty-five percent greater than that in the north. The difference arises from the fact that Saturn, with Titan along for the ride, has an eccentric orbit. It so happens that southern summer, which currently occurs when Titan's southern hemisphere is tilted toward the sun, coincides with perihelion, when Saturn is closest to the sun in its orbit. The more intense sunlight of southern summer can result in a net flux of methane and ethane from the south to the north over many seasonal cycles, potentially creating the observed lake dichotomy. An interesting implication of this explanation is that it must change over time, as the orbital parameters which create the situation are slowly evolving over tens of thousands of years. This scenario is analogous to Earth's Milankovich Cycles, which are credited with causing periodic climate change and driving cycles in the distribution of our own volatile deposits (glaciers).

While studying the distribution of Titan's lakes gave us a greater understanding of Titan's hydrologic system, there was little known about how they varied seasonally. This changed in the summer of 2009, when the RADAR obtained is first images of Ontario Lacus. Ontario Lacus, Titan's largest southern lake, was originally observed by the ISS instrument in 2004 and 2005 [Turtle et al., 2009a]. It was also observed by the VIMS instrument in late 2007, which produced spectra that identified liquid ethane in its composition [Brown et al., 2008]. In the RADAR images, Ontario Lacus looked smaller than it did in 2005. This was confirmed by lower resolution ISS images from March 2009 [Turtle et al., 2011]. By combining the RADAR images with altimetry data obtained the previous December, we were able to show that places along the shore with the most shoreline recession corresponded to the shallowest section of the lake and that, in general, shoreline recession followed relative changes in near-shore slope. This is exactly what you would expect if the lake level dropped by a constant amount. Around the same time we were analyzing Ontario, we were also investigating smaller southern lakes which disappeared between flybys in 2007 and 2008/2009. By using the Ontario data to calibrate the RADAR's absorption through the liquid, we were able to derive average loss rates for both Ontario and the small lakes of approximately one meter per year. These results were very exciting because we were not only able to confirm the presence of an active hydrologic cycle; we were able to see it in action! A discussion of these investigations are presented in Chapters 3 and 4 of this work and were published in a pair of papers submitted to the journals Icarus and JGR Planets in 2010 [Hayes et al., 2011, 2010]. These observations represent the first direct evidence for surface liquid playing an active role in Titan's hydrologic system.

The Cassini mission is now in its second extended mission, with Titan flybys planned out to 2017. Until recently, the RADAR held a monopoly on Titan's north pole as higher latitudes were in darkness during northern winter. As the north moves into spring and sunlight begins shining again, Cassini's passive imaging instruments will begin to observe the north polar lake district. We can look forward to a set of exciting new discoveries over the next few years as VIMS and ISS provide spectral information on the lakes and RADAR obtains repeat observations over many years, showing us how the system evolves. A summary of upcoming observations relevant to lacustrine science is presented in Chapter 5. Personally, I have been honored to be a part of this exciting time in Titan science and look forward to continuing to work with the diverse and highly talented scientists on the Cassini science teams.

Titan's surface is morphologically sculpted by a rich variety of aeolian, pluvial, fluvial, lacustrine, tectonic, endogenic, and exogenic processes. Both Titan and Earth have wind, rain, evaporation, erosion, standing bodies of liquid, and groundwater flow. Understanding methane flow on Titan teaches us about the development of Earth-like planets in both our own solar system as well as around other stars, and provides context for future discoveries in the field of extra-solar planets. Results from Cassini have even led some scientists to believe that the lakes may represent a habitable environment in which an exotic form of life could have evolved. For these and other reasons, Titan remains a high priority target for future spacecraft missions. Currently proposed mission designs for studying Titan include orbiters, balloons, planes, landers, and most interesting from a lakes perspective, boats and submersibles.

Chapter 2

Lake Distribution

Portions originally published in

A. G. Hayes, O. Aharonson, P. Callahan, C. Elachi, Y. Gim, R. Kirk, K. Lewis, R. Lopes, R. Lorenz, J. Lunine, K. Mitchell, G. Mitri, E. Stofan, and S. Wall. Hydrocarbon lakes on Titan: Distribution and interaction with a porous regolith. Geophysical Research Letters, 35:9204–9208, May 2008a. doi: 10.1029/2008GL033409

O. Aharonson, Hayes, A.G., J.I. Lunine, R.D. Lorenz, M.D. Allison, and C. Elachi. An asymmetric distribution of lakes on Titan as a possible consequence of orbital forcing. Nature Geosciences, 2:851–854, November 2009. doi: 10.1038/ngeo698

Abstract

Synthetic Aperture Radar (SAR) images of Titan's north polar region reveal quasi-circular to complex features which are interpreted to be liquid hydrocarbon lakes. We investigate methane transport in Titan's hydrologic cycle using the global distribution of lake features. As of July 2010, the SAR dataset covers $\sim 48\%$ of the surface and indicates multiple lake morphologies which are correlated across the polar region. Lakes are limited to latitudes poleward of 55° and vary from < 10 to more than 10^5 km^2. The size and location of lakes provide constraints on parameters associated with subsurface transport. Using porous media properties inferred from Huygens probe observations, timescales for flow into and out of observed lakes are shown to be in the tens of years, similar to seasonal cycles.

Derived timescales are compared to the time between collocated SAR observations in order to consider the role of subsurface transport in Titan's hydrologic cycle.

2.1 Introduction

Recent results from Cassini have suggested the presence of liquid hydrocarbons in Titan's northern latitudes and the presence of a liquid-bearing porous medium near its equator [Stofan et al., 2007a, Lorenz et al., 2006]. Analogous to water on Earth, surface conditions on Titan are near the triple point of methane, suggesting a methane-based hydrologic cycle which may incorporate solid, liquid, and gaseous phases. Observations of hydrologic features can be used to investigate transport in Titan's methane cycle through atmospheric evaporation [Mitri et al., 2007], surface flow, and subsurface drainage. In this chapter, we describe the interaction between a porous medium and the potential hydrocarbon lakes discovered by Cassini.

2.2 Lake Distribution

The $\mathrm{K_u}$ band Radar (2.17 cm wavelength) on the Cassini spacecraft is a multi-mode (imaging, altimetry, radiometry, and scatterometry) instrument designed to penetrate Titan's optically opaque atmosphere. When operating in imaging mode, high resolution (300-720 m/pixel with a cross-track range of 120-460 km) is obtained by applying Synthetic Aperture Radar (SAR) processing to the echo bursts [Elachi et al., 2004].

The first hydrocarbon lake features were identified in July 2006 and reported in Stofan

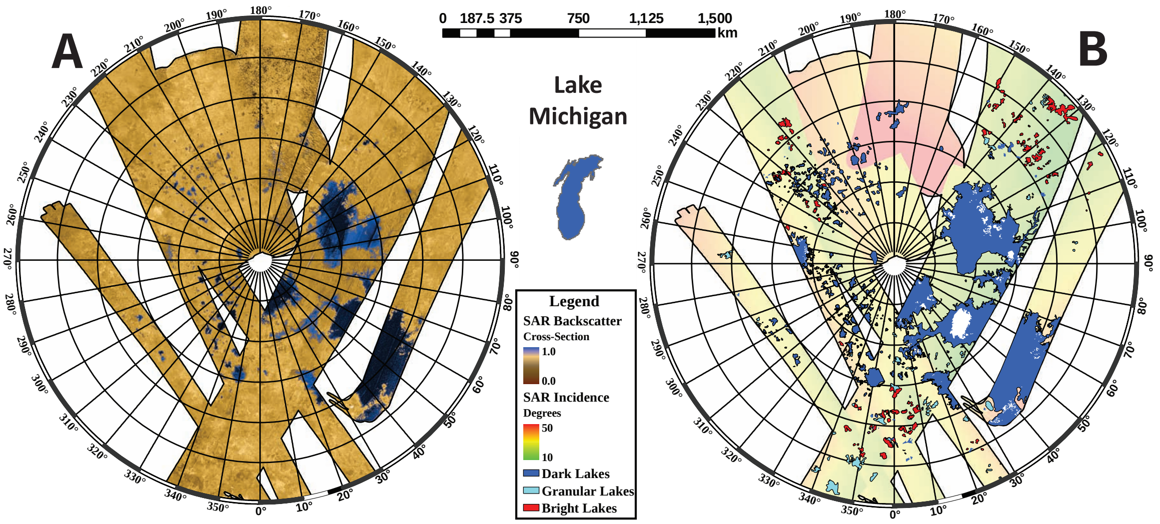

Figure 2.1: Distribution of lake features above $60°$N: A) Mosaic of Cassini SAR swaths through May 2007, B) Distribution of mapping units, dark lakes are blue, granular lakes are cyan, and bright lakes are red. Background color represents incidence angle during acquisition. Note outline of Lake Michigan for relative scale.

et al. [2007a]. The backscatter cross-sections in the dark patches are low compared to their surroundings, suggesting a smooth surface at a scale of 2 cm. Radiometric brightness differences are consistent with a flat surface with low dielectric constant, such as liquid hydrocarbons, surrounded by a water ice regolith [Stofan et al., 2007b]. Observed lake features are confined to latitudes poleward of $55°$, where 56.5% of the surface has been observed in the north and 62.3% of the surface has been observed in the south. Global SAR coverage (as of July 2010) encompasses 48% of the surface, 1.2% of which is covered by lakes. Overlapping swath sections, which total 21.8% of coverage above $55°$N and 24.9% of coverage below $55°$S, can be used to study temporal variation in observed features.

2.2.1 Mapping Unit Distribution

2.2.1.1 North Polar Region

We have identified 655 lake features in SAR data from 7 Titan flybys between July 2006 and May 2007 in Titan's north polar region. Lake-like features are separated into 3 classes; dark lakes, granular lakes, and bright lakes (see Figure 2.2B-D). Dark lakes are seen above $65°$N, where they take up 15% of the observed surface area. Granular lakes are distinguished from dark lakes by a relative increase in backscatter, although there is no distinct transition between these two units (see Figure 2.2A). Bright lakes are morphologically similar to dark and granular lakes, but have an interior with equal or higher backscatter than their immediate surroundings. Dark lakes are interpreted as liquid filled while bright lakes are interpreted as empty basins. Based on backscatter and location, granular lakes are inferred as transitional between dark and bright lake features. Figure 2.1 shows the spatial distribution of mapping units.

Dark lakes account for 394 of the 655 mapped lake features and 84% of the area of all lake units in the north polar region. The distribution of dark lakes surface area is approximately log normal with a mean of $87\ \mathrm{km}^2$. Lakes with areas in excess of $10^4\ \mathrm{km}^2$ represent 73% of the dark lake area and are generally confined to a region between $0°$E and $140°$E. For mapping purposes, dark lakes are defined as having ratios between median incidence-angle-corrected backscatter cross-sections inside and immediately outside the feature of ≤ 0.6. There is a trend toward lower ratios with increasing latitude (Figure 2.2A), suggesting radiation is either better reflected (specular) or absorbed by lakes closer to the pole. This behavior is expected if lakes are deeper at higher latitudes. Granular lakes, defined as having backscatter ratios between 0.6 and 1.0, represent a smooth transition from dark lakes. Bright lakes, which have ratios of ≥ 1, show distinct separation from granular lakes in backscatter ratio.

Granular lakes are found below 77°N and represent 6% of the total mapped lake area. The latitudinal emergence of granular lakes coincides with that of bright lake features. In almost all areas of Titan granular lakes are found in close proximity to bright lakes, suggesting an evolutionary relationship. Granular lakes show an increase in nonuniformity and relative backscatter ratio, consistent with radiation penetrating a liquid layer and interacting with the lake bottom. A histogram of the 109 granular lake areas is approximately log normal with a mean of $147\ \mathrm{km}^2$.

Bright lakes are interpreted as 200-300 m deep empty basins. Bright lakes, of which 152 have been mapped, represent 10% of lake features in the north. The areal distribution of bright lakes, which is also log normal, has a mean of $273\ \mathrm{km}^2$. The increase in characteristic area between dark, granular, and bright lakes may be related to the balance between evaporation and subsurface transport.

During the May 2007 flyby, altimetry data, coincident with previous SAR swaths, were obtained during closest approach. Figure 2.3 shows the position of the altimetry footprints on top of SAR imagery. The footprints coincide with two bright lake features. Surface heights are reported as the centroid of the altimetry waveforms and confirm that the bright lakes are depressions with 200-300 m walls. The sloping nature of the lake profile is a byproduct of topographic averaging within altimetry footprints. The integration of received power within an altimetry echo is proportional to nadir backscatter cross-section.

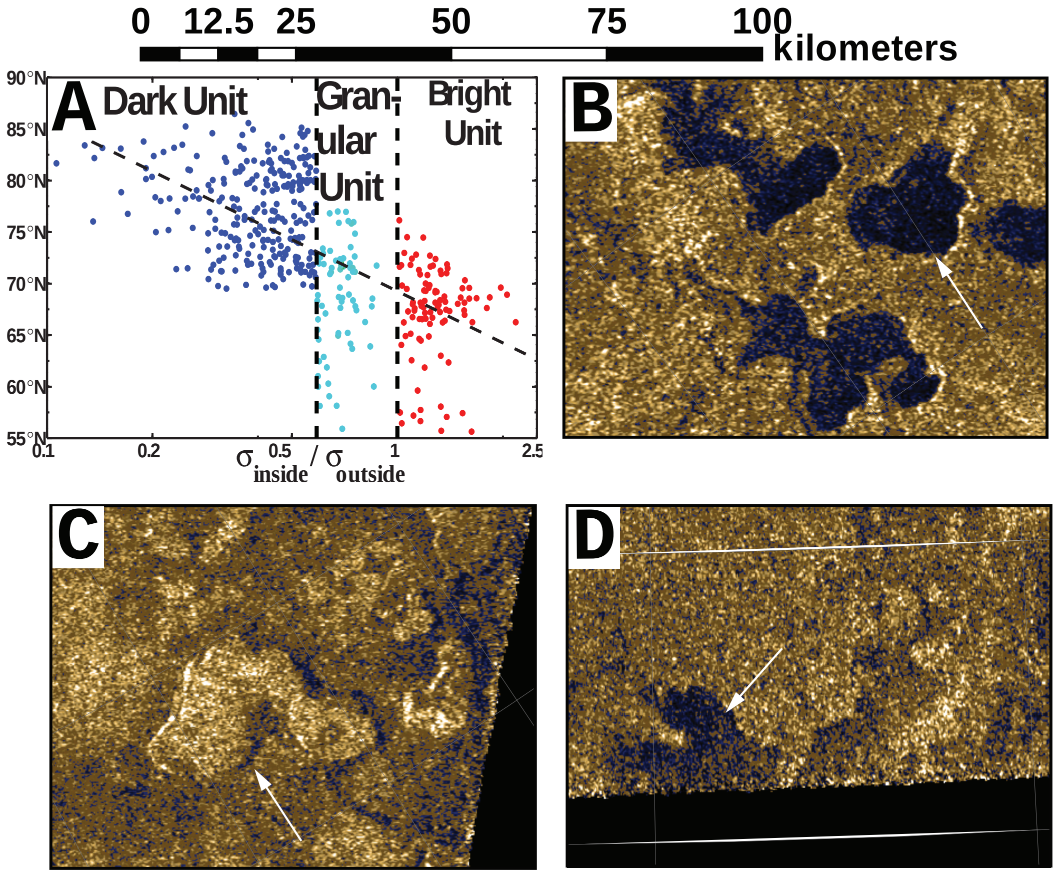

Figure 2.2: Mapping Units: A) Ratio between median incidence-angle-corrected off-axis backscatter within and immediately surrounding feature, B) Dark Unit, C) Bright Unit, D) Granular Unit.

For each bright lake the interior is brighter than the surroundings in both off-axis and nadir backscatter, suggesting that the radar-bright nature of empty lakes is compositional or due to volume scattering effects, as opposed to differences in roughness at $2\ \mathrm{cm}$. A liquid-filled lake would be expected to have high nadir and low off-axis backscatter.

2.2.1.2 South Polar Region

Extending lacustrine feature mapping into the south polar region reveals that the lake density is 26 times more sparse than in the north. Furthermore, as of July 2010, 95% of the

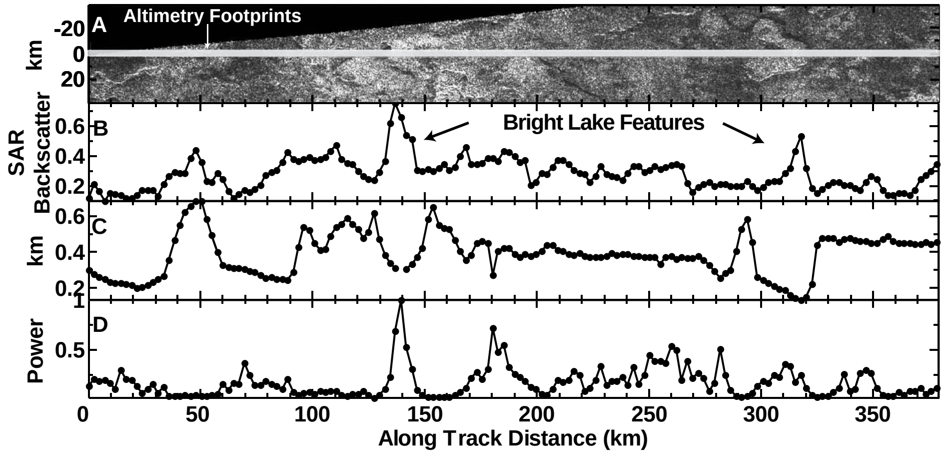

Figure 2.3: A) SAR backscatter with altimetry footprints overlain, B) Median SAR backscatter within altimetry footprints, C) Centroid of altimetry waveforms (average height above 2575 km); D) Integrated altimetry waveform power (normalized), which is proportional to nadir backscatter. Note correlated peaks / dips at ~ 140 and ~ 320 km corresponding to bright lake features.

areal lake coverage observed by radar in the south is accounted for by Ontario Lacus (Figure 2.4). Ontario Lacus is a dark-albedo feature initially observed by Imaging Science Subsystem (ISS) and recently confirmed to contain liquid ethane by Brown et al. [2008] using data from the Visual and Infrared Mapping Spectrometer (VIMS). The properties of Ontario Lacus are the subject of Chapter 3 of this work. Dark lakes account for 0.4% of the coverage area poleward of $55°$ in the south, as compared to 10.5% in the north. Granular and empty lakes take up 0.1% and 0.4% of the area in south polar region and 0.7% and 1.2% of the north polar region, respectively. Figure 2.4 shows the distribution of southern lacustrine features. The morphology of lacustrine features in the south is notably different from the north, lacking both the large mare and clustered groupings of smaller lakes which are characteristic of northern terrain. Also of note are dark areas, morphologically similar to terrestrial mudflats [Lopes et al., 2010], found near (150°E, 80°S) and (0°E, 75°S).

Table 2.1: Lacustrine feature coverage statistics. Values represent percentage of observed coverage area.

Feature	Global	North (55°N-90°)	South (55°N-90°)
Swath Coverage	47.8%	56.2%	62.8%
Filled Lakes	1.2%	10.5%	0.4%
Granular Lakes	0.1%	0.7%	0.1%
Empty Lakes	0.2%	1.2%	0.4%

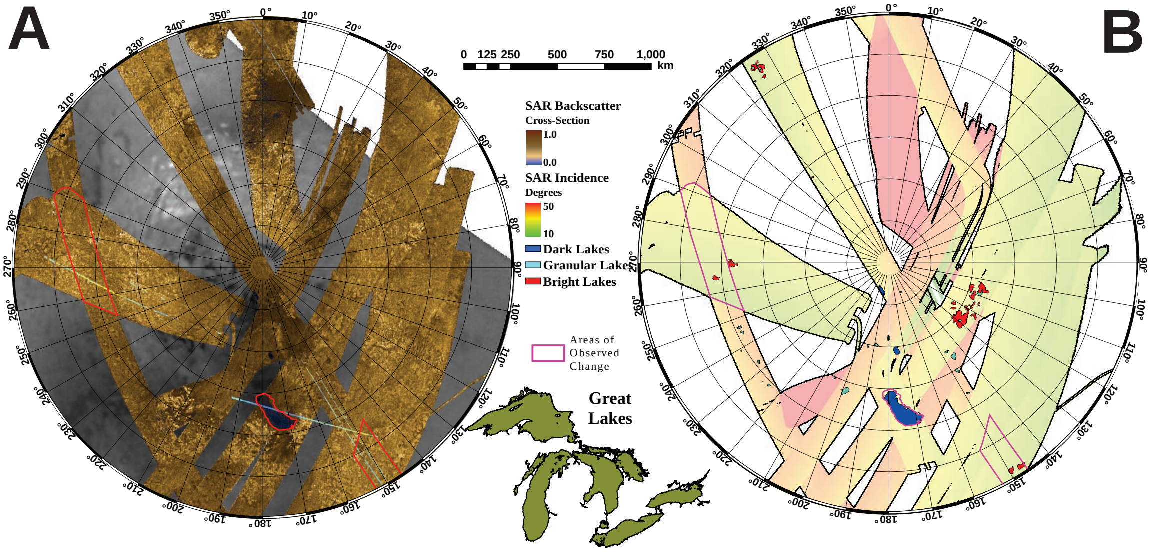

Figure 2.4: Distribution of lake features poleward of 60°S: A) Mosaic of Cassini SAR swaths through July 2010, B) Distribution of mapping units, Dark lakes are blue, granular lakes are cyan, and bright lakes are red. Background color represents incidence angle during acquisition. Note outline of the Great Lakes for relative scale.

Limited topography from SAR-Topo measurements [Stiles et al., 2009, Zebker et al., 2009] suggests these features are located in the lowest elevations of the south polar region (Figure 2.4). When referenced to estimates of Titan's geoid [Iess et al., 2010], these areas have comparable elevations to north polar mare shorelines reported in Kirk et al. [submitted].

2.2.2 Morphology

The morphology of lakes on Titan span the range of observed morphologies on Earth. Lakes with distinctly polygonal shapes, rough shoreline geometries, and associated channels are similar to terrestrial drainage lakes dominated by surface flow. Comparatively rounded lake boundaries with sharp shorelines and no associated channel networks are consistent with seepage lakes interacting with a local ground-methane system. Other lakes seem to be dendritic or branching in nature and have similar morphology to flooded river valleys [Stofan et al., 2008]. Observed lakes appear to be in varying states of evolution, ranging from slightly underfilled (dark/granular lakes) to completely empty (bright lakes). Granular and bright lakes are not seen poleward of 77° and are almost always found within close proximity of each other. A notable exception is between 180°E and 240°E in the north polar region, where bright lakes are found in the absence of granular lakes. This region is also characterized by a large density of small circular features consistent with a network of seepage lakes interacting with a subsurface alkanofer, the analog of an aquifer on Earth.

2.2.3 Implications for Change on Orbital Timescales

Potential explanations for the hemispherical dichotomy in lake distribution are discussed in Aharonson et al. [2009] and include seasonal effects, topographic differences between the poles, and energetic effects resulting from variations in solar insolation. While seasonal effects may seem the most obvious, the paucity of both empty and filled lakes point to a process with longer timescales. The empty lakes in the north are consistently observed to be 200-300 m depressions. Masking the signature of such a depression would be difficult over the 29.5 yr Titan season. A regional topographic difference in which the south polar region is raised relative to the equipotential surface or there exists some impermeable subsurface boundary preventing subsurface flow is also possible. However, the global topography and gravity data available as of July 2010 do not support this theory [Zebker et al., 2009, Iess et al., 2010]. In fact, the best-fit ellipsoid for the current data set suggests that the difference between northern and southern polar topography is an order of magnitude smaller than the topographic variation within the polar regions themselves.

A third possibility is that the asymmetry in lakes is caused by the asymmetry is Titan's season due to Saturn's eccentricity and obliquity. The solar longitude (L_s) of Titan's southern summer solstice is currently within 6° of Saturn's perihelion. Conversely, northern summer solstice occurs within 6° of aphelion, when Titan is 1 AU further from the sun. Due to this geometry Titan's southern summers are shorter and more intense than its northern summers, with a peak insolation difference of $\sim 25\%$ at the top of the atmosphere. This energy difference, when propagated through the atmosphere, can provide a forcing for net movement of both methane and less volatile species, such as ethane, to the north pole over tens of thousands of years. Current Global Climate Models (GCMs), such as Graves et al. [submitted], predict the observed lake dichotomy when this orbital configuration is incorporated into the model.

However, Saturn's orbital elements are not constant. The currently situation was reversed $\sim$ 32 kyr ago, with northern summer experiencing a $\sim 25\%$ higher peak insolation than the south. The variation of Saturn's orbital parameters are such that the seasonal asymmetry will reverse over periods of $\sim$ 50 kyr, requiring Titan's polar surfaces to be

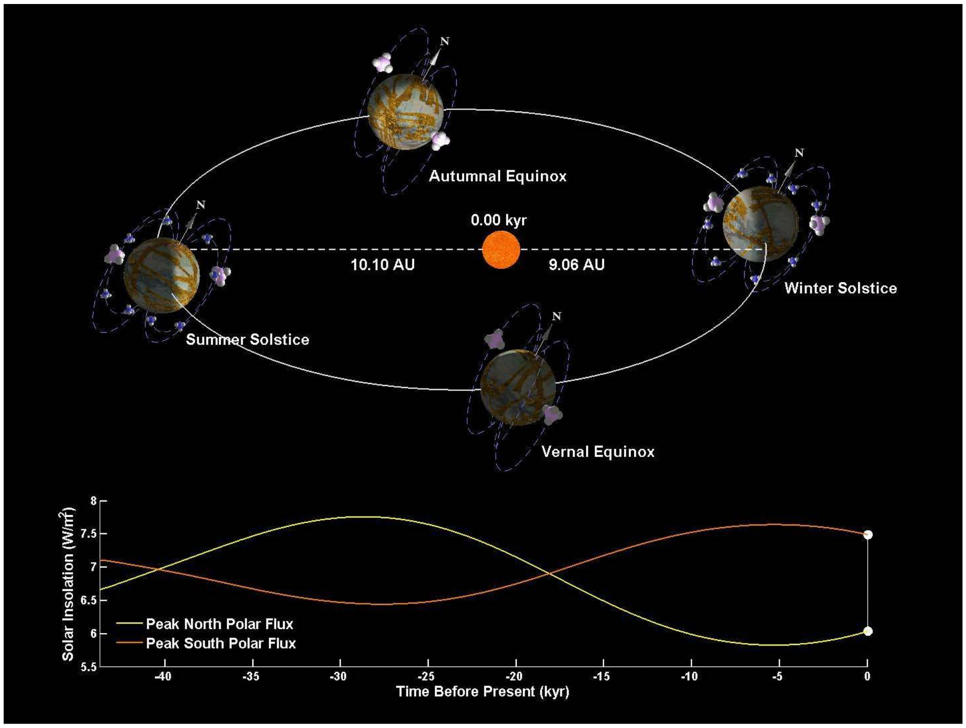

Figure 2.5: Position of Titan's seasons relative to Saturn's orbit. Summer solstice currently coincides with perihelion, resulting in a 25% peak insolation difference between southern and northern polar summer. As the orbital elements evolve, so does the insolation difference.

modified on timescales of tens of thousands of years [Aharonson et al., 2009]. While the lack of observed craters in the polar regions of Titan may support this theory, the masking of 200-300 m depressions in 50 kyr timescales is still difficult. Regardless, this hypothesis is consistent with the observed lake distribution, magnitude of dynamic changes observed by the ISS and radar instruments, and VIMS detection of ethane in Ontario Lacus (see Chapter 4).

2.3 Shoreline Complexity

Historically, lake shorelines have been described through a parameter known as Shoreline Development (SLD) [Johnson, 1919]. SLD is defined as the ratio between the perimeter of a lake and the perimeter of a circle with equal area:

$$SLD = \frac{P_{Lake}}{2\sqrt{\pi A_{Lake}}} \tag{2.1}$$

For lakes whose shorelines can be mapped at consistent m-scale resolution SLD is a useful metric for shoreline complexity. On Titan, image resolutions are not constant, and measurement elements are limited to 300 m or greater. The value of SLD varies as a function of the size and phasing of the resolution element used to measure lake perimeters. A more robust morphometric index for quantifying shoreline complexity is the Minkowski-Bouligand fractal dimension, which describes how space filling an object is. Under ideal conditions, the fractal dimension is independent of the limiting resolution element for a pseudofractal object. Fractal geometry was first applied to the coastline of Britain and has since become widely used to study the self-similar nature of geologic structures [Mandelbrot and Mulvey, 1980]. It has been shown that geological processes, operating uninterrupted at a particular length scale, will give rise to fractal geometries [Mandelbrot, 1977].

The fractal dimension can be empirically calculated if an allometric relationship exists between length or area and the size of the measurement element used to determine it. In one-dimension a smooth curve would have a fractal dimension of one, while a curve with increasing convolution would converge toward a fractal dimension of two [Mandelbrot, 1977]. For closed shapes, such as a lake shoreline, the most intuitive method for calculating the fractal dimension (D) is the relationship between perimeter (L) and the measurement element (s) used to calculate it:

$$L(s) \propto s^{(1-D)} \tag{2.2}$$

For a set of polygons with similar fractal dimension, there are also relationships between the area and perimeter of shapes within the set:

$$F(A) \propto A^{-<D>/2} \tag{2.3}$$

$$C_0 = \frac{L^{1/<D>}}{2\sqrt{\pi A}} \tag{2.4}$$

Equation (2.3) is known as Korcak's fractal law and $F(A)$ is the fraction of objects in the set which have area greater than A [Korcak, 1940]. Equation (2.4) is derived by Mandelbrot [1977] and shows that SLD is simply a biased measure of the fractal dimension.

The fractal nature of shoreline structure on Titan can be tested through the linearity of logarithmic plots of lake perimeters vs. measurement elements. An independent test of applicability can be made through the comparison with fractal dimensions calculated using Equations (2.3) and (2.4). The fractal dimension of dark lake shorelines derived from Equation (2.2) range from 1.0 for circular features to > 1.4 for the most complex geometries. The median fractal dimension of the mapped dark lakes is 1.16 and the standard deviation is 0.04. Equations (2.3) and (2.4) yield characteristic fractal dimensions for the set of 1.16 ± 0.03 and 1.17 ± 0.02. The agreement between the fractal dimensions derived from all three methods suggest that fractal patterns are present in shoreline geometries on

Titan. A histogram of the individual fractal dimensions (Figure 2.6) does not show any multi-modal nature, which would have been indicative of multiple lake formation or evolution mechanisms. Fractal dimensions calculated for set of lakes in Wisconsin varied from 1.10 to 1.40 and were found to be related to lake classification (ex: seepage vs. runoff).

For dark lake features, logarithmic plots of lake perimeter vs. measurement element show linear and bilinear relationships. Most of the lakes exhibit a linear (albeit slightly sinuous) profile, suggesting a similar complexity at all length scales. Some plots, however, show an increase in slope after passing a knee in the profile, suggesting that small scale structure has a lower complexity than large scale structure. For some lake features the knee corresponds to the value of the limiting resolution in the SAR data. For lakes in which the knee cannot be explained by a limiting resolution, they consistently lie between 1.2 and 1.5 km and corresponds to the dark lakes radiometrically near the granular unit transition. Most of the granular and empty lakes shows bilinear behavior with knee locations in the vicinity of 1.5 km, suggesting a process which smooths small scale structure below $\sim$ 1 km. This process may be related to the transition from dark to empty lakes. Alternatively, the effect could be related to a measurement bias driven by borders that do not represent a solid / liquid boundary.

Sharma and Byrne [2010] present a detailed independent study of the fractal character of Titan's lakes. They find a one sigma range of fractal dimensions between 1.17 and 1.42, as compared to 1.12 and 1.20 for the distribution described above. While both Sharma and Byrne [2010] and this study utilize the divider method [Klinkenberg and Goodchild, 1992] for determining the fractal dimension, there are a number of differences that can potentially contribute to the observed discrepancy. First and foremost is the fact that lake shorelines were mapped manually in both studies. Differences in shoreline selection decisions and mapping scales can significantly affect the resulting fractal dimension, especially considering the nature of multiplicative speckle noise inherent to SAR processing [Goodman, 1976] (see Chapter 3). In addition, Sharma and Byrne [2010] mapped portions of larger lakes, which were observed over multiple SAR swaths, as individual features. In the present study lake polygons, which were also mapped from individual SAR swaths, were projected and combined prior to calculating their fractal dimension. As the larger lakes typically have more complex shorelines, incorporating multiple segments from these features will trend the histogram of fractal dimensions presented in Sharma and Byrne [2010] toward higher values as compared to this study. Lastly, Sharma and Byrne [2010] do not make a distinction between the dark and granular lake classes. Granular lakes are commonly observed to exhibit bi-linear behavior in their allometric relationships and characteristically have higher fractal dimensions than dark lakes. Granular lakes were excluded from the histogram presented in Figure 2.6, further distinguishing it from the more inclusive histogram presented by Sharma and Byrne [2010]. However, despite these differences, the qualitative results of Sharma and Byrne [2010] are in agreement with the present study, namely:

- The shorelines of Titan's lakes can be described as self-similar fractals, similar to lacustrine features on Earth.
- Fractal dimension correlates with lake morphology. Features similar to terrestrial seepage lakes have lower fractal dimensions than features similar to lakes dominated by surface runoff.
- Some shorelines, most notably those of the granular and empty lakes, exhibit bi-linear behavior in their allometric relationship. This may imply that there are multiple surface processes which act predominantly at different spatial scales. Alternatively, the behavior could be related to measurement bias driven by the complexity of radar scattering in Titan's polar terrain.

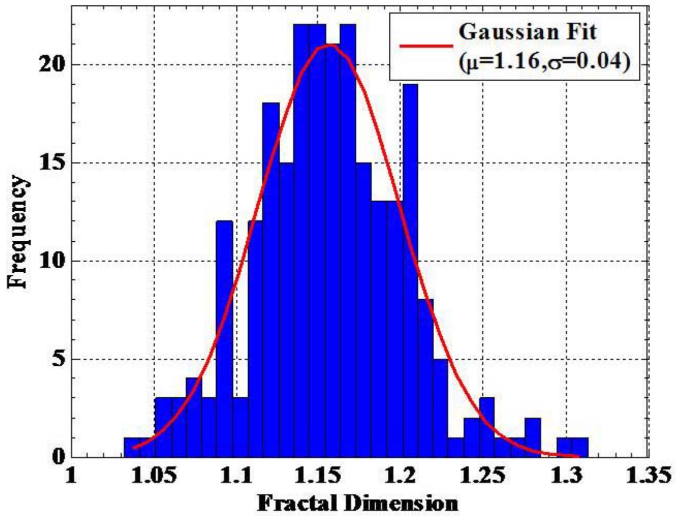

Figure 2.6: Histogram of observed fractal dimensions calculated using Equation (2.2).

To further examine the quantitative differences between Sharma and Byrne [2010] and the present study, the specific algorithms and mapping polygons used for each would need to be compared in detail.

2.4 Preliminary Topography

A physically rigorous sensor model is required to reliably estimate three dimensional coordinates from matching points in coincident SAR swaths [Kirk et al., 2007]. Such a model has recently been developed by the U.S. Geological Survey (USGS) for use with the Socet Set stereogrammetry software package marketed by BAE Systems [Kirk et al., submitted]. In addition to stereogrammetry, topography is also available from radar altimetry and a new technique known as SAR-Topo [Stiles et al., 2009]. SAR-Topo is a stereo processing technique which makes use of the overlapping beam patterns of the Cassini Radar. The height of a point on the surface within the beam overlap area can be estimated by the relative return measured in each beam. Initial comparisons between altimetry, stereo, and SAR-Topo have shown promising correlations between the various techniques [Stiles et al., 2009]. SAR-Topo strips are available for nearly every SAR swath and provide a sparsely populated map of global topography.

As expected, the large northern seas, or mare, are located in the lowest topographic region and their shoreline elevations are self-consistent to within the ~ 150 m absolute accuracy of the available data [Kirk et al., submitted]. While this does not conclusively show that the mare shorelines share an equipotential surface, it is not inconsistent with such a hypothesis. Further support for shared mare shoreline elevations is provided by the apparent connection between the largest mare, as viewed by ISS and VIMS [Turtle et al., 2009a]. The area of empty and granular lakes, which flanks the mare to the south, lie ~ 400 m above the mare shorelines. The area of small lakes located between $120°$W and $160°$W lie 600-800 m above the mare shorelines, producing a potential hydrologic head for subsurface transport. The regional slope between the small lakes and the mare is ~ 0.04 degrees. Empty lakes observed in varying locations throughout the north polar region are seen as 200-300 m depressions by all three topographic techniques (Figure 2.7). The 1 km variation in topography near the northern mare may help to generate lake-effect clouds recently observed by VIMS [Brown et al., 2009a].

While lakes near the mare exhibit elevations that are arguable consistent with the sea shorelines distant lakes, on the other hand, are topographically elevated by 400-800 m (Figure 2.7). In some cases, these lakes even lie in a state of local hydrologic disequilibrium. It will be important to observe these areas again during the Cassini extended missions in

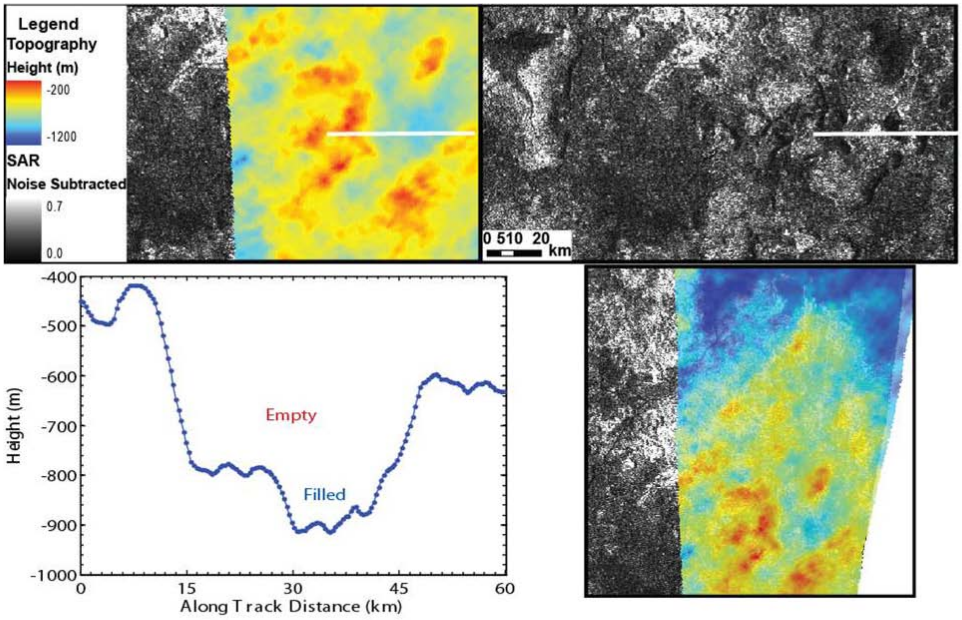

Figure 2.7: Topography derived from stereo analysis of T25 and T28 SAR swaths showing empty lakes to be 200-300 m depressions and sea shorelines lying at similar elevations.

order to see how they temporally evolve. As discussed in the next section, the evolution of lakes of different sizes in these areas can provide constraints on the properties of the local porous regolith. Under simplifying assumptions, small lakes are dominated by interaction with the subsurface (infiltration) while large lakes are dominated by interaction with the atmosphere (evaporation).

2.5 Flow Through Porous Media

The rate of liquid inflow or outflow from a lake through the subsurface is governed by regional topography and the properties of the local porous medium and, if present, saturated alkanofer (the hydrocarbon equivalent of groundwater on Earth). The Huygens Probe provided information constraining soil properties near (168°E, 10°S) and suggested the presence of a damp porous medium consisting of loosely packed particles between the sizes of silt to medium sand [Lorenz et al., 2006, Zarnecki et al., 2005]. The material properties observed by Huygens are used as a starting point to model subsurface transport in Titan's northern latitudes. Flow is assumed to be primarily horizontal and approximately described by a one-dimensional representation of the groundwater flow equation in cylindrical geometry, presented as a modified form of the Boussinesq equation:

$$\frac{\partial h}{\partial t} = \frac{1}{\phi r}\frac{\partial}{\partial r}\left(Krh\frac{\partial h}{\partial r}\right) + P \tag{2.5}$$

where h is the height of the alkanofer surface, t is time, ϕ is porosity, r is distance from the lake center, and K is the hydraulic conductivity ($K = \kappa\rho g/\mu$). Hydraulic conductivity, which describes the ability of liquid to flow through pore space, depends on the permeability of the porous medium (κ), liquid density (ρ), gravity (g), and dynamic viscosity (μ). Permeability can vary by up to 6 orders of magnitude for the grain sizes observed by Huygens. For simplicity, flow is modeled using methane as the primary constituent and results are investigated for a significant range of permeabilities: 10^{-4} (medium sand) to 10^{-10} (silt) cm^2.

Equation (2.5) is modified from its standard form only in the addition of P, which is the next loss/gain from precipitation and evaporation . The evaporation rate is taken to be $0.3\ \mathrm{m/yr}$, consistent with an average surface wind speed of $0.1\ \mathrm{m/s}$, methane mixing ratio of 0.35 in the lakes, and methane relative humidity (RH) of 50% [Tomasko et al., 2005], although RH is likely greater because of a 2-3 K temperature drop between the equator and poles. Evaporation rates are derived by balancing latent and sensible heat fluxes, as in

Mitri et al. [2007], and depend linearly on surface wind speed, methane mixing ratio, and deviation from saturation ($1 - \mathrm{RH}$). A wind speed of $0.1\ \mathrm{m/s}$ is consistent with the lack of observed wave activity on lake surfaces and cooling rates of the Huygens probe [Lorenz, 2006]. Vertical infiltration is characteristically 2 orders of magnitude faster than horizontal seepage and is approximated by the hydraulic conductivity. Complete vertical infiltration would occur on a timescale of $\sim H/K$, where H is the lake depth and K varies from 1 to 10^6 m/yr for the permeability range mentioned above ($\kappa = 10^{-6}\ \mathrm{cm}^2$ corresponds to $K = 10^4\ \mathrm{m/yr}$). The persistence of lakes between repeat observations in the north suggests that a methane table or impermeable boundary exists within a distance of H/ϕ from the bottom of the lake and that subsurface flow is predominantly horizontal. Moreover, the presence of lakes in singular observations alone suggests the presence of a boundary limiting complete vertical infiltration, unless data acquisition temporally coincides with a precipitation event or the regolith is highly impermeable. However, regional scale vertical infiltration, linked to changes in the phreatic surface, may be more common and can result in ephemeral lakes similar to those observed in the south and discussed in Chapter 4.

Permeability can be a strong function of length scale; dominated by the porous medium over small scales and cracks and caverns over large scales. For the purposes of this work, permeability is assumed homogeneous and isotropic. Hydraulic conductivity is usually anisotropic, and flows tend to partially disperse horizontally and refract vertically at contacts in horizontally graded soils. In the absence of crustal stirring, non-volatile products of photolysis, which settle down to Titan's surface [Yung et al., 1984], may have formed a 10-100 m scale layer above a more permeable regolith derived from early meteoric bombardment.

Figure 2.8 describes two endmembers in a range of case studies investigating the interaction between a hydrocarbon lake and its surrounding porous medium. The first (Figure 2.8A) represents a lake, initially filled, with the saturated zone existing a distance b beneath the lake bottom. The second case represents a lake coincident with the saturated zone, which can be created from Figure 2.8A by setting $h = D$. The temporal evolution of each system can be described by Equation (2.5) using appropriate initial conditions and assuming no flow lines penetrate the saturated zone. The solutions shown in Figure 2.8 can be approximately scaled to varying initial conditions using:

$$\tau_{1/2} \sim \left[\pm \frac{4KH}{R^2} \left((1+\frac{b}{H})^2 + \frac{SR}{H}(1+\frac{b}{H}) \right) + \frac{2P}{H} \right]^{-1} \tag{2.6}$$

where S is the slope of the methane table and Equation (2.6) is the harmonic average of characteristic timescales for evaporation and infiltration. The sign of the first term is determined by the direction of subsurface flow, positive for outflow and negative for inflow. In the case where the methane table is coincident with the lake surface, $b = 0$ and the first term is negative. Under the assumption that no flow lines penetrate into the saturated zone, subsurface loss is proportional to the area of the lake walls, while evaporative loss scales with surface area. Hence, the ratio of these fluxes scale with lake radius, the dominant loss term transitioning from subsurface transport for small lakes to evaporative loss for large lakes. Note that while evaporation will remove liquid methane, liquid ethane and nitrogen are comparatively stable at Titan's surface.

The first case study (Figure 2.8A) is a simplified example of a drainage lake, which is emptied by both subsurface transport and evaporation. When the methane table is located below the lake bottom, it is assumed that the liquid will vertically infiltrate to the level of the table, creating a cylindrical volume that will radially diffuse out of the regolith. Drainage timescales for $100\ \mathrm{km}^2$ lakes (median dark lake size), located 0 and $10\ \mathrm{m}$ above the methane table are depicted in Figure 2.8B. A lake depth of $10\ \mathrm{m}$ is chosen [Paillou et al., 2008b]. For permeabilities of $< 10^{-6}\ \mathrm{cm}^2$, evaporation begins to dominate and drainage timescales are limited to of order 10 years, similar to seasonal timescales. The interpretation of this result is that disequilibrium conditions can persist over timescales exceeding 10 years for porous media properties consistent with Huygens probe observations. Drainage timescales for lakes located in highly permeable environments ($\kappa > 10^{-4}\ \mathrm{cm}^2$) are dominated by infiltration while impermeable environments ($\kappa < 10^{-7}\ \mathrm{cm}^2$) are dominated by evaporation.

In the second case study, which represents an ideal seepage morphology, evaporation removes liquid methane while infiltration replenishes it until the local alkanofer is depleted. In Figure 2.8C, the dependance of removal timescales on lake areas for a seepage dominated morphology is shown. For large lakes, evaporation dominates and removal timescales are similar to cases where the surrounding medium is unsaturated. For each permeability, however, there exists a size threshold below which influx from the regolith can balance evaporation in a quasi-stable state over multiple seasonal cycles. For the region consistent with a seepage morphology between $240°$E and $180°$E, where the dark lakes are $\sim 100\ \mathrm{km}^2$ and bright lakes are characteristically $\sim 200\ \mathrm{km}^2$, this suggests a permeability of order 10^{-5} or $10^{-6}\ \mathrm{cm}^2$ if we assume that equilibrium has been reached. Repeat observations during the Cassini extended missions may help test this hypothesis.

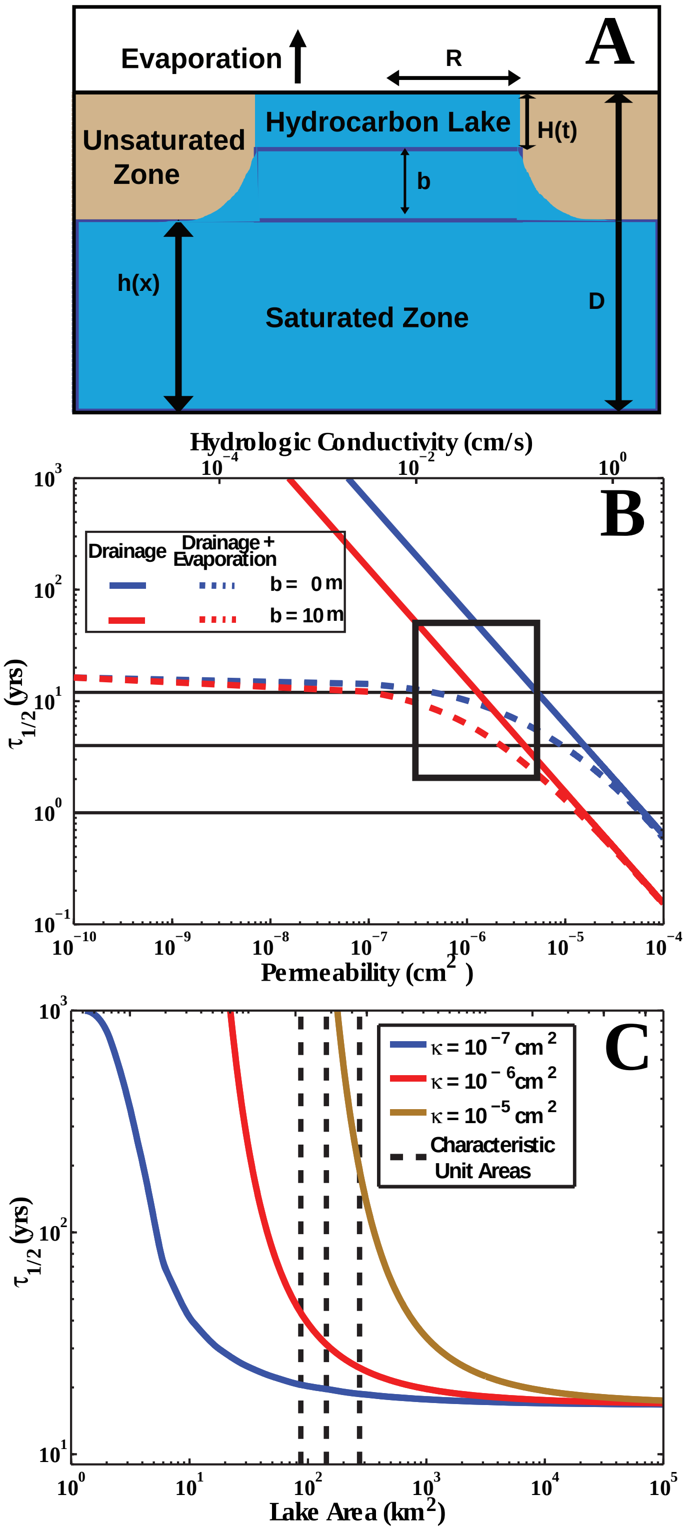

Figure 2.8: Interaction between a single lake and its immediate surroundings: A) Model parameters; Lake resting in regolith with a saturated alkanofer a distance b from its bottom. $h = D$ when the alkanofer is coincident with the surface and $(D - h) \geq H$ when the lake is sitting in unsaturated regolith, B) Drainage timescales for horizontal diffusion into an unsaturated regolith. Black lines represent the current overlap ($\sim$ 1 yr), nominal mission ($\sim$ 4 yrs), and maximum mission ($\sim$ 12 yrs) lengths. The highlighted region is the most probable permeability range based on Huygens data, C) Removal timescale versus lake area when the methane table is coincident with the lake surface. Vertical lines are the characteristic areas of dark, granular, and bright lakes.

2.6 Summary

Lake size and distribution illuminate aspects of hydrologic activity in the polar regions of Titan. Dark lakes are found poleward of $70°$, showing a general trend of decreased off-axis backscatter toward the pole. Granular lakes emerge at $\sim 77°$ and are found at absolute latitudes as low as $55°$. Backscatter ratio variation between dark and granular lakes suggest a smooth transition between the two classifications. Bright and granular lakes are found interspersed in the same latitude ranges. Integration of altimetry waveforms show that bright lakes are radar bright in both nadir and off-axis backscatter, suggesting they have similar roughness length scales to surrounding terrain but different material properties. Potential explanations include the collection of micron-sized atmospheric fallout particles or evaporative products into the lakes or mm to cm-scale porosity structures beneath the lake beds, possibly created by dissolution chemistry.

The distribution and character of lake-like features can be used to constrain parameters associated with subsurface flow. Basic case studies suggest that timescales for lake drainage are of order 10 years for permeabilities $< 10^{-6}\ \mathrm{cm}^2$, similar to seasonal timescales. A region consistent with seepage morphology between $240°$ E and $180°$ E in the north polar region suggests that permeabilities in the local area are of order 10^{-5} or $10^{-6}\ \mathrm{cm}^2$. Theoretical vertical seepage rates suggest that lake floors are within H/ϕ of the methane table or an impermeable boundary. Continued observations over the lifetime of the Cassini mission will place upper bounds on the effective permeability in the north polar region. If changes are observed, lower bounds can be estimated as well. Topographic information is currently being used to incorporate mapped lake distributions into subsurface flow models.

This will allow the study of the interaction between the surface and subsurface and its role in generating observed morphologies.

Acknowledgements

The authors would like to thank Tom Farr, Ronald Blom, and Michael Janssen of JPL and David Stevenson of Caltech for helpful discussions, and the Cassini engineering team, without whom the data presented here would not have been possible.

Chapter 3

Lake Properties: Ontario Lacus Bathymetry and Absorptivity

Originally published in

A. G. Hayes, A. S. Wolf, O. Aharonson, H. Zebker, R. Lorenz, R. L. Kirk, P. Paillou, J. I. Lunine, L. Wye, P. Callahan, S. Wall, and C. Elachi. Bathymetry and Absorptivity of Titan's Ontario Lacus. Journal of Geophysical Research: Planets, 115:E09009, 2010. doi: 10.1029/2009JE003557

Abstract

Ontario Lacus is the largest and best characterized lake in Titan's south polar region. In June and July 2009, the Cassini RADAR acquired its first Synthetic Aperture Radar (SAR) images of the area. Together with closest-approach altimetry acquired in December 2008, these observations provide a unique opportunity to study the lake's near-shore bathymetry and complex refractive properties.

Average radar backscatter is observed to decrease exponentially with distance from the local shoreline. This behavior is consistent with attenuation through a deepening layer of liquid and, if local topography is known, can be used to derive absorptive dielectric properties. Accordingly, we estimate near-shore topography from a radar altimetry profile

that intersects the shoreline on the east and west sides of the lake. We then analyze SAR backscatter in these regions to determine the imaginary component of the liquid's complex index of refraction (κ). The derived value, $\kappa = (6.1^{+1.7}_{-1.3}) \times 10^{-4}$, corresponds to a loss tangent of $\tan\Delta = (9.2^{+2.5}_{-2.0}) \times 10^{-4}$ and is consistent with a composition dominated by liquid hydrocarbons. This value can be used to test compositional models once the microwave optical properties of candidate materials have been measured.

In areas that do not intersect altimetry profiles, relative slopes can be calculated assuming the index of refraction is constant throughout the liquid. Accordingly, we construct a coarse bathymetry map for the near-shore region by measuring bathymetric slopes for eleven additional areas around the lake. These slopes vary by a factor of $\sim$5 and correlate well with observed shoreline morphologies.

3.1 Introduction

Ontario Lacus, originally imaged by the Instrument Science Subsystem (ISS) in July 2004 and June 2005 [Turtle et al., 2009a], was Cassini's first glimpse into Titan's surface hydrocarbon inventory. With an area of 15,600 km^2, it remains the largest lake observed in the south polar region. The Visual and Infrared Mapping Spectrometer (VIMS) observed Ontario in December 2007 and spectrally confirmed the presence of liquid ethane [Brown et al., 2008]. Infrared mapping of the shoreline at a resolution of 330-2500 m/pixel suggested the presence of surrounding annuli which Barnes et al. [2009] interpreted as evidence for changes in lake level. Recent observations by ISS in March 2009 [Turtle et al., 2009b] and Radar in June/July 2009 [Hayes et al., 2011] have detected shoreline recession, confirming Ontario is an active feature. Lorenz et al. [2010a] discuss morphologic and hydrologic similarities between Ontario Lacus and Racetrack Playa, an ephemeral lake located in Death Valley National Park, CA USA. In this work, we derive the imaginary component of Ontario's complex refractive index and create a near-shore bathymetry map using a combination of radar backscatter and altimetry.

Cassini has observed Ontario Lacus with multiple instruments between July 2004 and January 2010, making it the best characterized lacustrine feature on Titan. Synthetic Aperture Radar (SAR) images were acquired on June 22, 2009 (Titan flyby T57), July 8, 2009 (T58), and January 12, 2010 (T65). Closest-approach altimetry observations were obtained in December 21, 2008 (T49). The SAR images have a resolution of 260-350 m/pixel and show varied shoreline morphologies including landforms similar to drowned river valleys and wave-dominated beachheads [Wall et al., 2010]. Passive microwave radiometry, obtained coincident with active SAR, shows Ontario is colder than both its local surroundings and northern counterparts, suggesting either evaporative cooling or a lower emissivity [Wall et al., 2010, Mitri et al., 2007]. Altimetry returns from the lake surface are specular in nature and place an upper limit of 3 mm on the root-mean-square (RMS) height of any surface waves over the 100 m Fresnel zone of radar beam footprints during the December 2008 flyby [Wye et al., 2009].

The combination of closest-approach altimetry and high resolution SAR observations presents a unique opportunity to study Ontario Lacus. The normalized radar backscatter cross-section (σ_o) drops off exponentially with distance from shoreline. This behavior is consistent with attenuation through a deepening liquid medium and, if the local topography is known, can be used to estimate the imaginary component of the complex index of refraction (κ). The complex refractive index at microwave wavelength determines the depth to which radar waves can penetrate lakes on Titan, and is a function of liquid composition. Complex refractive indices are calculated in two areas where altimetry profiles intersect the lake shoreline. To within errors, both measurements are consistent and are bounded by the expected attenuation properties of liquid hydrocarbon at 90 K.

The observed exponential fall off in radar return is further used to estimate local bathymetric slopes in areas where the topography was not sampled by altimetry. These slopes are used to generate a coarse near-shore bathymetry map assuming that refractive properties are uniform throughout the lake. Using this method, we estimate bathymetric slopes for eleven additional areas around the lake, ranging from $(0.5 - 2.7) \times 10^{-3}$.

We present our analysis in four parts: data reduction, model fitting, model validation, and discussion of results. Data-processing steps taken for calculating lake depth and average radar return are described in Section 3.2. We develop the best-fit model to the reduced data in Section 3.3, and assess the validity of the model and its sensitivity to underlying assumptions in Section 3.4. Interpretation of model results, including morphological and compositional implications, are presented in Section 3.5.

3.2 Data Reduction

The Cassini RADAR measures the normalized backscatter cross-section (σ_o) of Titan's surface at 2.16 cm. The normalized backscatter cross-section is a nondimensional quantity that describes the reflected power received by the radar. For every element on the surface, the measured power is converted into the effective area of an isotropic scattering surface that would produce the observed signal. This effective area is then divided by the imaged surface area yielding a non-dimensional σ_o value for each pixel [Ulaby et al., 1982]. For a given wavelength, polarization, and incidence angle, σ_o is an intrinsic property of the surface and can be used to distinguish between different terrain models. Unfortunately single measurements, or looks, of σ_o are highly dependent on small-scale structure in the terrain, and thus temporal or spatial averaging is required before analyzing the effects of material properties or large-scale structure. For Ontario Lacus, the average σ_o as function of distance from shore is used to determine microwave absorption coefficients and determine local bathymetric slopes.

Noise in measurements of σ_o have two common sources: speckle noise and instrument noise. Speckle noise is produced by mutually interfering electromagnetic waves that are scattered off of a surface that is rough on the order of the wavelength, and is thus embedded in the radar signal. Conversely, instrument noise results primarily from thermal noise in the antenna receiver, and is thus an artifact of radar signal measurement. Instrument noise is nominally subtracted during SAR processing and reported as the noise equivalent backscatter ($\sigma_\mathrm{o}^{(\mathrm{ne})}$). Speckle noise for single-look data follows an exponential probability distribution of the form [Goodman, 1976]:

$$P(\sigma_\mathrm{o})d\sigma_o = (1/\sigma_\mathrm{o}^{(\mathrm{t})})e^{-\sigma_\mathrm{o}/\sigma_\mathrm{o}^{(\mathrm{t})}}d\sigma_o \tag{3.1}$$

where $\sigma_\mathrm{o}^{(\mathrm{t})}$ is the mean backscatter from the surface. Speckle noise is typically suppressed by averaging multiple looks of the same surface element. As the number of looks becomes large, $P(\sigma_\mathrm{o})$ approaches a normal distribution in accordance with the central limit theorem. For the T57, T58, and T65 radar observations, the number of looks varied from 1 to 4 and the average σ_o, reported after subtraction of $\sigma_\mathrm{o}^{(\mathrm{ne})}$, is -22.3 ± 0.1, -20.29 ± 0.03 and -18.25 ± 0.02 dB, respectively. This difference in average lake backscatter is not surprising given differences in incidence angle between flybys: $42°$-$44°$ for T57, $26°$-$32°$ for T58, and $21°$-$29°$ for T65. For a single look, the 95% confidence interval (CI) varies from -15.9 dB to $+5.7$ dB about the mean value $\sigma_\mathrm{o}^{(\mathrm{t})}$; for four looks, this interval is reduced to only -5.6 dB to $+3.4$ dB. These intervals span the total backscatter variation observed in Ontario's near-shore region (-10 to -20 dB) and have significant probability of being below the average radar noise floor, which varies between flybys: -17.46 ± 0.04 for T57, -20.09 ± 0.05 for T58, and -18.97 ± 0.01 dB for T65. Within ~ 10 km of the shore, these σ_o values can be modeled as radiation penetrating a liquid layer and interacting with the lakebed [Hayes et al., 2008a, 2011, Paillou et al., 2006, 2008b,a, Ventura et al., 2009].

For observations with few looks, additional averaging is required to further reduce speckle noise. This is typically achieved through spatial averaging using box filters, which is reasonable assuming small spatial gradients in σ_o [Elachi and van Zyl, 2006]. In our study of Ontario's near-shore region, however, box filtering would average over the exponential falloff with distance from shoreline. Therefore, we modify the usual box averaging approach by using long and narrow boxes oriented parallel to shoreline (Figure 3.1 inset). Averaging in these along-shore bins reduces speckle noise while minimally affecting the expected exponential decay in the near-shore region. The error in estimates of the bin-averaged backscatter $\langle\sigma_\mathrm{o}\rangle$ are calculated using a boot-strap Monte Carlo technique [Press et al., 1992]. This technique involves creating a large number of synthetic data sets (1000) by randomly selecting, with replacement, values from the observed data within a given distance bin. Additionally, we calculate statistical metrics, such as the mean and skewness, for each synthetic data set. The 95% confidence interval (CI) of these distributions are reported as the error in the equivalent metrics for the observed data. After binning and averaging, $\langle\sigma_\mathrm{o}\rangle$ exhibits normally distributed errors, enabling the use of chi-square minimization as a maximum likelihood estimator for model parameters (see Section 3.3).

In order to ensure a robust result, we calculate the distance from shore using both simple and complex shorelines. Simple shorelines are defined by two points connected by a line in the region of interest, which is 15 km in along-shore length, while the complex shorelines consist of many points with an average separation distance equal to the image resolution (260-350 m). Sensitivity to shoreline selection is not large and is discussed in Section 3.4. Bin averaging is performed at a resolution 3 times finer than the observed data. To accomplish this, the raw data are nearest-neighbor sub-sampled to higher resolution, where depths are calculated for each sub-pixel by multiplying distance from shoreline with regional slope, as discussed below. Averaging in this high-resolution space reduces artifacts introduced by finite pixel size, allowing pixels to be fractionally apportioned into appropriate depth bins.

Closest-approach altimetry observations obtained in December 2008 (T49) show a constant topographic slope of $S = (1.22 \pm 0.03) \times 10^{-3}$ for $\sim$100 km leading up to Ontario Lacus (Figure 3.2). Assuming this measured slope extends at least a few kilometers into the lake and that the direction of steepest topographic descent is perpendicular to the shoreline, we estimate the local bathymetric slope, or dip, as $D = S/\cos\psi$, where ψ is the angle between the altimetry track and the local normal to shoreline. Given the bathymetric slope, we can obtain the depth of the lakebed $d = Dr$, where r is the distance from the shoreline. In the southeast altimetry intersection (region A Figure 3.1) $S_{\mathrm{A}} = (1.22 \pm 0.03) \times 10^{-3}$ and $\psi_{\mathrm{A}} = 51.5 \pm 1.5°$. In the northwest altimetry intersection (region L of Figure 3.1) $S_{\mathrm{L}} = (1.7 \pm 0.6) \times 10^{-4}$ and $\psi_{\mathrm{L}} = 80 \pm 3°$. Correcting for orientation, the estimated bathymetric slopes are $D_{\mathrm{A}} = (2 \pm 0.1) \times 10^{-3}$ and $D_{\mathrm{L}} = (1 \pm 0.5) \times 10^{-3}$, similar to the topographic slopes in the lakebed of Racetrack Playa on Earth [Lorenz et al., 2010a]. For the remainder of this manuscript, topographic slopes will refer to measure slopes on the landward side of a shoreline while bathymetric slopes will refer to slopes in the near-shore region of a lakebed.

Terrestrial examples support the assumption that near-shore bathymetry contours are parallel to lake shores and, in the absence of human intervention, are typically similar on land and lake-sides of a shoreline [Brunskill and Schindler, 1971, Waples et al., 2005, USGS, 2001]. Near-shore slopes of Lake Tahoe in northeastern California, for example, are maintained for multiple kilometers away from the shore in both directions [USGS, 2001]. The consistent topographic slope, which extends for 100 km beginning immediately offshore of region A in Ontario Lacus, suggests that the lake lies in a shallow regional basin and that the slope would likely continue a few kilometers into the lake. This necessary assumption, while uncertain, is supported by the exponential fall off of $\langle \sigma_{\mathrm{o}} \rangle$ with distance from shore and the consistency between derived bathymetric slopes and observed morphologies (see Section 3.5). In Section 3.4, we test the significance of this assumption using a fractal model for small-scale topography and find that, in this case, its effects are minimal.

3.3 Model

Together, observed SAR backscatter and estimated near-shore lake depth provide a method for measuring the complex index of refraction of Ontario Lacus. Assuming the liquid surface and lake bottom have similar backscatter properties between SAR pixels, the variation in radar-return can be described by a simple two-layer model

$$\sigma_{\mathrm{o}}^{(\mathrm{m})} = \sigma_{\mathrm{o}}^{(1)} + \sigma_{\mathrm{o}}^{(2)}\, e^{-8\pi\kappa d \sec\theta_{\mathrm{liq}}/\lambda} \tag{3.2}$$

where κ is the imaginary component of the index of refraction and λ is the SAR wavelength in vacuum. The incidence angle in liquid hydrocarbon (θ_{liq}) is given by Snell's law

$$\theta_{\mathrm{liq}} = \sin^{-1}\left(n_{\mathrm{atm}}/n_{\mathrm{liq}}\ \sin\theta\right) \tag{3.3}$$

where the real components of the refractive indices for the liquid and atmosphere at 13.6 GHz are approximately $n_{\mathrm{liq}} \approx 1.3$ and $n_{\mathrm{atm}} \approx 1$. The three unknown parameters in this model are the combination of residual noise and backscatter from the liquid surface ($\sigma_{\mathrm{o}}^{(1)}$), the lakebed backscatter at zero depth ($\sigma_{\mathrm{o}}^{(2)}$), and the imaginary component of the refractive index (κ). The offset term $\sigma_{\mathrm{o}}^{(1)}$ is likely composed of residual instrument noise, and any surface backscatter from Bragg waves, or other small-scale roughness on the liquid surface [Wright, 1968]. Small shifts in local shoreline selection primarily add an offset to lake

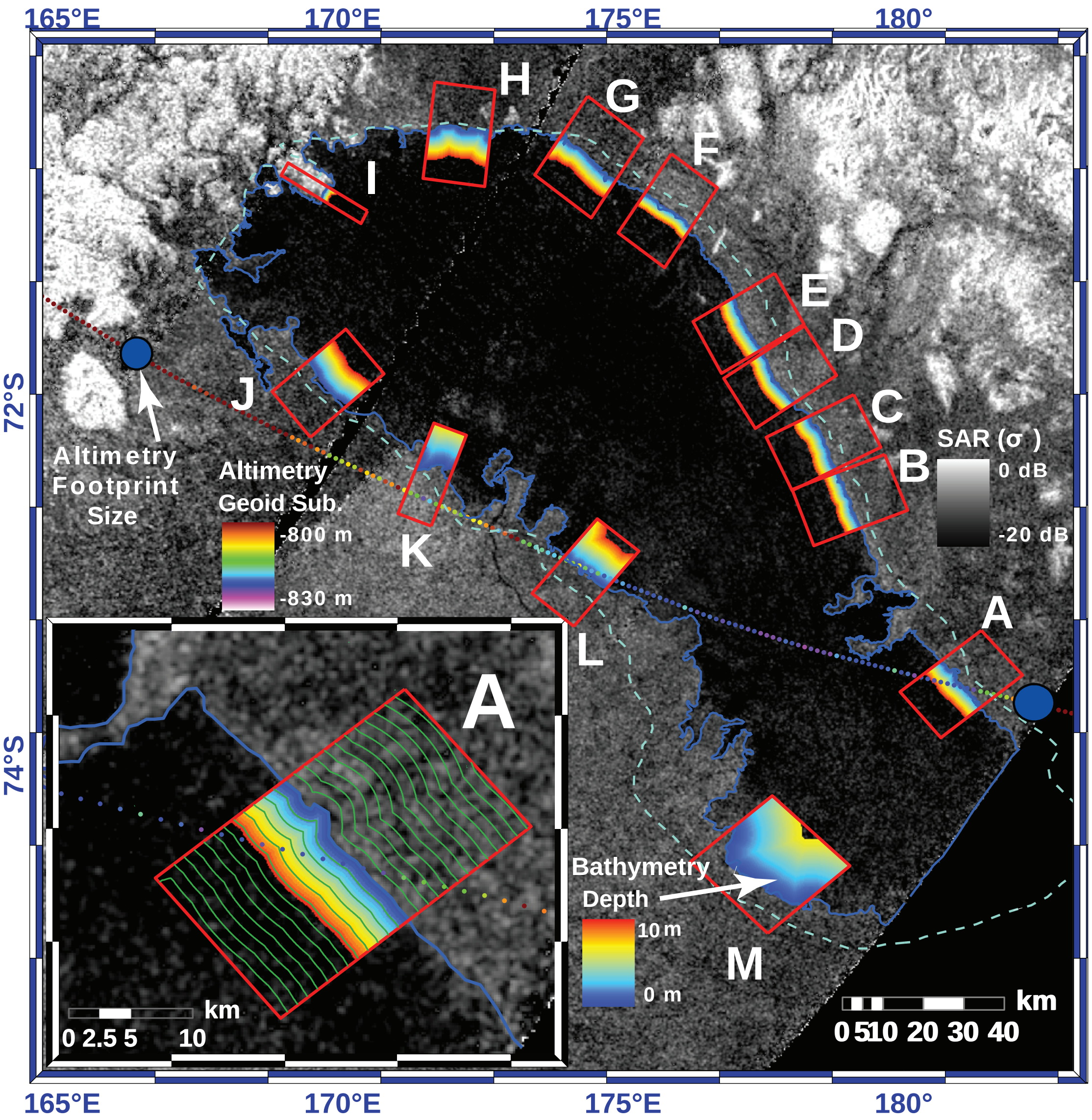

Figure 3.1: Equidistant cylindrical projection of Ontario Lacus centered at at 72°S. Study areas A through M are outlined in red. T49 altimetry footprint centers are plotted over SAR data. Blue circles represent the size of altimetry footprints. SAR and ISS outlines of the lake are shown in blue and cyan, respectively. Near-shore bathymetry is presented within each region of interest. Regions of interest (excluding G, I, and M) are $\sim 15 \times 24$ km and contain $\sim 10^4$ pixels. Regions G, I, and M have along-shore dimensions of 20, 4, and 30 km, respectively. Each distance bin contains $\sim 10^2$ pixels. Regions H, I, and J are located within T57 while the remaining regions are located in T58. Inset; Region A with contours of constant distance from shoreline. Bin size was increased by a factor of 3 as compared to analysis bin sizes for visualization purposes.

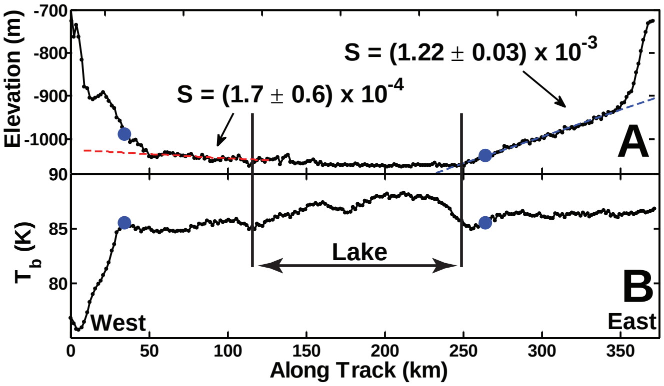

Figure 3.2: Analysis of December 2008 (T49) altimetry track. Blue circles correspond to positions marked in Figure 3.1.; A: Geoid subtracted altimetry using radar echo center of mass. Geoid values obtained from Iess et al. [2010]. Local slopes near altimetry intersections with Ontario Lacus are shown.; B: Brightness temperature from passive radiometry experiments. Highest value in Ontario is ∼87 K, which is colder than the northern lakes.

depth affecting $\sigma_{\mathrm{o}}^{(2)}$ but do not appreciably change the value of κ, which is our primary focus. It should be noted that we cannot disentangle the effects of composition and particulate scattering in the total value of κ for the liquid medium.

We fit the depth-bin averaged σ_{o} values and their associated uncertainties to Equation 3.1 using the Levenberg-Marquardt method for non-linear least squares estimation [Levenberg, 1944, Marquardt, 1963]. To find the best fit, we minimize the reduced chi-square fitness metric, defined as

$$\chi_\nu^2 = \frac{1}{N_{\mathrm{dof}}} \sum_{i=1}^{N} \frac{\left(\langle\sigma_{\mathrm{o}}\rangle - \sigma_{\mathrm{o}}^{(\mathrm{m})}\right)^2}{\left(\mathrm{var}(\langle\sigma_{\mathrm{o}}\rangle) + \left(\frac{\partial\sigma_{\mathrm{o}}^{(\mathrm{m})}}{\partial \mathrm{d}}\right)^2 \mathrm{var}(d)\right)} \tag{3.4}$$

where the modeled value $\sigma_{\mathrm{o}}^{(\mathrm{m})}$ is defined by Equation (3.2), $\mathrm{var}(x)$ is the variance in x, N is the number of points in the transition region, and N_{dof} is the number of degrees of freedom. Uncertainties in $\langle\sigma_{\mathrm{o}}\rangle$ are estimated using the Monte Carlo routine described in Section 3.2.

Variance in depth, $\mathrm{var}(d)$, is controlled by the combination of errors in shoreline selection and unknown small-scale roughness of the lakebed. We fit assuming both perfect shoreline selection ($\mathrm{var}(d) = 0$) and 1 pixel error in shoreline estimation ($\mathrm{var}(d) = (\mathrm{D}\ \Delta\mathrm{x}_{\mathrm{pix}})^2$, where Δx_{pix} is the pixel resolution which varies from 260-350 m).

We estimate confidence intervals using a bootstrap Monte Carlo technique and report the maximum extent of the 95% confidence ellipses in parameter space [Press et al., 1992]. Using a bathymetric dip of $(2 \pm 0.1) \times 10^{-3}$ to calculate lake depth, we find the imaginary component of the complex index of refraction for region A (Figure 3.3; top) to be $\kappa_{\mathrm{A}} = (6.1^{+1.7}_{-1.3}) \times 10^{-4}$. The reduced chi-square value of the fit, assuming no error in depth estimation, is $\chi^2_\nu = 5.0$. Allowing for 1 pixel errors on the distance from shoreline or equivalent vertical noise, the reduced chi-square is $\chi^2_\nu = 1.2$. Incorporating $\sim$1 pixel errors in shoreline position does not, to within errors, alter the values of the best-fit coefficients (see Section 3.4). Fitting the average radar return from region F, using a slope $D_{\mathrm{L}} = (1 \pm 0.5) \times 10^{-3}$, the best-fit complex index of refraction is $\kappa_{\mathrm{L}} = (6.2^{+3.5}_{-2.5}) \times 10^{-4}$, consistent with region A. Region L has a reduced chi-square value of $\chi^2_\nu = 9.0$ assuming perfect shoreline position and $\chi^2_\nu = 1.4$ assuming 1 pixel error in shoreline position or equivalent vertical noise. The highly oblique angle between the altimetry track and shoreline near region L, however, makes our determination of slope much more uncertain.

In all regions around the lake backscatter variation can be split into three components: shore response, near-shore transition, and lake response. Figure 3.3 shows $\langle \sigma_{\mathrm{o}} \rangle$ vs. d for regions A and L plotted alongside the models for the best fit and 95% confidence intervals. The two plateaus for large distances from the transition region are the shore and lake response, respectively. We fit the two-layer model to data in the transition region, which is bounded by vertical lines. Correlated noise arising from low signal-to-noise ratio (SNR) and structure in the lake interior increases χ^2_ν when the transition region is extended further offshore. The fit error can be reduced in these regions by omitting outliers in the darkest portions of the lake. The best fit coefficients, however, are not significantly affected by this structure. Increased amplitude of the noise structure outside the transition region begins where the real aperture radar footprint includes only dark lake pixels, thus hindering echo phase determination during SAR processing.

We determined fit coefficients for thirteen locations around the lake (Figure 3.1 A-M), and present results in Table 3.1. In regions other than A or L, where the altimetry track intersects the shoreline, the resulting exponential coefficient represents the product of the imaginary index of refraction multiplied by the ratio of the local bathymetric slope to the measured topographic slope in A. Assuming that the index of refraction does not vary around the lake, the difference in fit coefficients are equal to the relative slope, representing a coarse lake bathymetry. Morphologic correlations with variations in relative bathymetric slope are discussed in Section 3.5.

The reported model coefficients are derived using the T57 and T58 SAR data. The T65 SAR data was acquired while this manuscript was in review and the final calibration was not available at the time of publication. Preliminary analysis of T65 data, however, returns similar results for κ and bathymetric slope despite differences in viewing geometry, adding confidence to the results reported here.

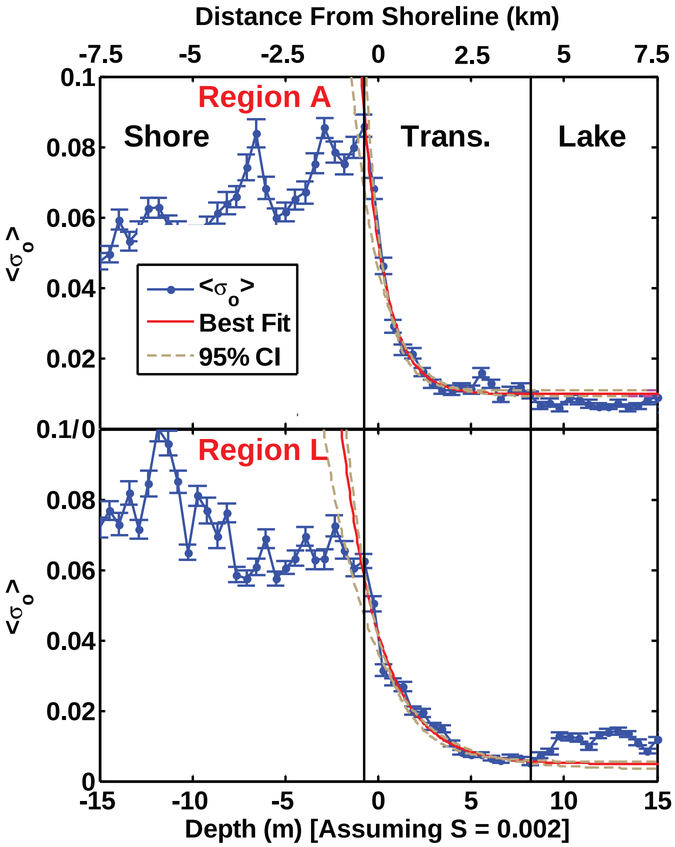

Figure 3.3: Top: Along-shore averaged radar backscatter and model fits for Region A; Bottom: Along-shore averaged radar backscatter and model fits for Region L. The red and brown lines represents the best-fit and 95% CI models within the transition region. Data from within the lake and on the shoreline were not used in fitting. The left-edge of the transition region was selected by hand. Zero depth corresponds to pixels lying along the Ontario shoreline derived from image data and does not necessarily correspond to the left edge of the transition region.

Table 3.1: Model fitting results for regions A-M. Coefficient errors are 95% confidence intervals. Local bathymetric dip (D) is determined by referencing to the observed on-land topographic dip at region A ($D_{\mathrm{A}} = (2 \pm 0.1) \times 10^{-3}$) and assuming the imaginary component of the index of refraction (κ) is uniform throughout the lake. * denotes that the slopes are measured using on-land Altimetry measurements (Regions A and L) as opposed to estimated using the model coefficients. † denotes areas where there are less than four depth bins within the first two exponential skin depths of the transition region. The model parameters $\sigma_{\mathrm{o}}^{(1)}$ and $\sigma_{\mathrm{o}}^{(2)}$ represent the surface backscatter and zero-depth lakebed backscatter as defined by Equation 3.2 and discussed in Section 3.3. Chi-square goodness-of-fit metrics (χ_ν) are reported for the data, Linear Mixing Model (LM), and Exponential Attenuation Model (ExM) as described in Section 3.4.

Region	$\sigma_{\mathrm{o}}^{(1)}$			$\sigma_{\mathrm{o}}^{(2)}$			D ($\times 10^{-3}$)			χ_ν^2 Fit	χ_ν^2 LM	χ_ν^2 ExM
	Mean	95% CI		Mean	95% CI		Mean	95% CI				
A	0.009	0.0080	0.0098	0.044	0.038	0.052	2.00*	1.90*	2.10*	1.2	5.9	1.4
B	0.018	0.0099	0.022	0.055	0.026	0.073	2.52	0.86	3.98	2.3	3.4	2.6
C	0.023	0.015	0.027	0.049	0.027	0.064	2.29	1.25	3.71	2.6	5.2	2.7
D	0.019	0.017	0.020	0.040	0.027	0.053	2.34	1.43	4.05	14.2	9.9	3.7
E	0.016	0.004	0.019	0.039	0.021	0.107	2.23	1.33	4.62	9.92	10.9	2.8
F	0.01	0.009	0.012	0.054	0.044	0.063	2.68	2.12	3.44	8.6	9.8	3.9
G	0.009	0.0082	0.010	0.022	0.016	0.027	1.85	1.56	2.52	8.9	23.6	5.5
H	0.0056	0.0037	0.0072	0.033	0.029	0.037	1.40	0.83	1.96	8.0	47.1	6.9
I†	0.0097	0.0075	0.012	0.070	0.029	0.092	4.85	2.83	5.87	3.6	33.1	2.4
J	0.013	0.0046	0.021	0.026	0.018	0.036	1.24	0.71	2.16	6.5	7.0	3.4
K	0.0038	0.0014	0.007	0.056	0.047	0.065	0.74	0.60	0.88	8.7	75.0	6.9
L	0.0021	0.00056	0.048	0.041	0.037	0.046	1.00*	0.50*	1.50*	1.4	50.2	2.4
M	0.021	0.018	0.025	0.026	0.038	0.033	0.46	0.39	0.61	6.6	5.1	2.3

3.4 Model Validation

In order to model the observed near-shore backscatter as exponential attenuation through a deepening liquid medium, we assumed both that the shoreline is accurately determined and that bathymetric contours are parallel to the local shoreline. As shown in the previous section, we can model the observed data well using these assumptions. Nevertheless, it is important to explore how violations of these assumptions might bias our results. In the following section, we examine how errors in shore-line selection and realistic small-scale lakebed topography might affect our analysis. We demonstrate for both of these cases that error sources large enough to significantly change our results also noticeably alter the pixel brightness distribution statistics within our SAR images, imprinting them with identifiable markers. We do not find evidence for these markers in our observed data, suggesting such significant errors are not present.

The variance in SAR pixel backscatter due to speckle noise confounds shoreline selection. It is thus reasonable to expect some mixing of true lake and shore pixels in the transition region when using an uncertain shoreline. Linear mixing of bright and dark values may imitate the expected backscatter fall off with distance from shore. Therefore, it is important to limit the polluting effects of linear mixing by restricting our analysis to regions of low shoreline complexity (Figure 3.1 A-M). Additionally, we characterize the effects of improper shoreline selection to ensure that linear mixing is not skewing the results. This is accomplished by analyzing the shape of backscatter distributions within each depth bin. We find that small errors in shoreline selection do not significantly affect the results, and large errors can be ruled out by the changes they induce in distribution characteristics within the transition region.

As a first test for the dependence of our analysis on shoreline selection, we use both straight-line (within the region of interest) and smoothly varying shorelines to calculate pixel depths. The resulting best-fit coefficients do not vary outside their error between the straight-line and smoothly varying cases, though the reduced chi-square and parameter variances for the straight-line fits are characteristically larger. In order to confidently rule out linear mixing, a more careful study was performed by comparing the data to two end-member models. The first model uses a highly complex shoreline and synthesizes images based on linear mixing alone. In the second model, we assume the backscatter in the transition region between shore and lake pixels results purely from exponential decay through a deepening liquid medium. Each model is two-dimensional and generates images that are processed using the same data reduction and modeling techniques outlined in Sections 3.2 and 3.3. The characteristics of the pixel distributions for both models within each distance bin are then compared to the observed data.

The Linear Mixing Model (LM) uses a complex shoreline created by following contours of σ_{o} around Ontario Lacus. Constant values for lake (σ_{lake}) and shore (σ_{shore}) backscatter are obtained using least-squares minimization, matching the backscatter inside and outside the lake far from the transition region (Figure 3.3). For each distance bin, we record the extent of mixing that results from the meandering of the complex shoreline relative the smoothly varying shoreline discussed in Section 3.3. A synthetic two dimensional image at the resolution of the SAR data is generated by assigning lake or shore identities to each pixel according to the complex shoreline, while distance bins for along-shore averaging are generated using the smooth shoreline. The backscatter of a pixel is then determined by averaging random draws from a speckle noise distribution centered at σ_{lake} or σ_{shore} (Equation (3.1). The number of draws are determined by the number of looks for each pixel in the original data.

In contrast to LM, the Exponential Attenuation Model (ExM) assumes no linear mixing. ExM generates a two dimensional image using average backscatter values determined by the best-fit coefficients from Equation 3.2 for the smooth shoreline defined in Section 3.3. The purpose of ExM is to understand the expected variation in σ_{o} assuming exponential attenuation through a deepening liquid medium. Similar to LM, pixel values are assigned by averaging random draws from an appropriate speckle noise distribution, where the number of draws are given by the number of looks in the actual data. In order to understand noise-induced variations, each model is generated many times and the distributions of statistical metrics are recorded.

While the effect of linear mixing on the average backscatter in the transition region can be similar to exponential attenuation, it causes large changes to the shape of the pixel distributions for even small degrees of contamination. One metric for the shape of a distribution is the skewness (γ_1), which is a measure of asymmetry about the mean [Press et al., 1992]. For single-look observations, speckle noise skewness is 1.6-2.6 (95% CI), regardless of $\sigma_{\mathrm{o}}^{(\mathrm{t})}$, and decreases with the square root of the total number of looks. When draws are made from two or more speckle noise distributions, such as in LM, data skewness can increase to values of 8 or greater. Skewness is most sensitive to small percentages of shore contamination in a bin mostly composed of lake pixels. Other statistical metrics, such as the relative

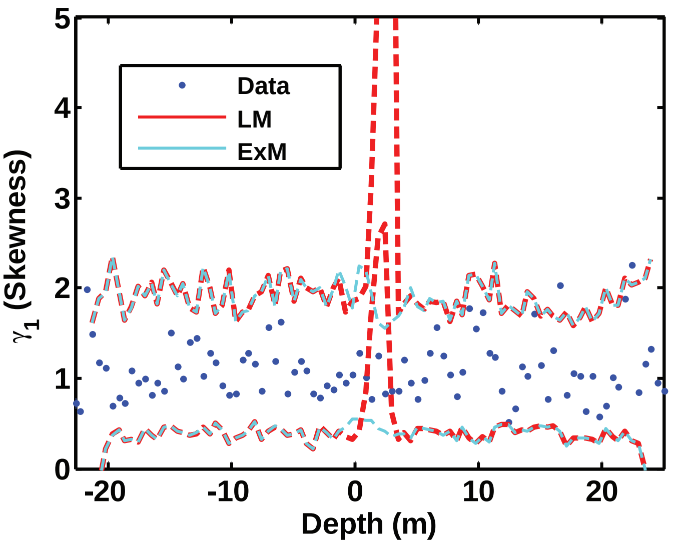

Figure 3.4: Skewness (γ_1) for region A. The observed data is plotted in blue. Skewness for the Linear Mixing Model (LM) and Exponential Attenuation Model (ExM) is shown in red and cyan, respectively. The lines are the lower and upper bounds of the 95% CI for each model. Note the LM shows a large increase in skewness within the transition region that is not observed in the data, or ExM. This suggests that the data set does not have significant mixing of shore and lake pixels within the same distance bin.

mean difference, non-uniformity, and kurtosis, are sensitive to greater percentages of contamination. Skewness in region A, for the observed data and both backscatter models, is shown in Figure 3.4. As expected, LM shows a large increase in skewness within the transition region. In contrast, ExM and observed data have similarly low values of skewness in all regions, suggesting that the observed data is dominated by exponential attenuation rather than linear mixing. This relationship holds true for all regions of interest.

The reduced chi-square between the ExM and observed data in region A is 1.4, in agreement with the 1D fits using Equation 3.2. Goodness of fit between LM and observed data, however, is significantly poorer ($\chi^2_\nu = 5.9$). Reduced chi-square values comparing ExM and LM to observed data in other regions are listed in Table (3.1)1. Areas where the transition region is as narrow as 1-2 pixels, such as the northern mountainous terrain, reinforces the interpretation that exponential attenuation in variable lake depth is responsible for more gradual transitions, which can be as wide as ~ 40 pixels in region M.

While the above test rules out pure linear mixing, it relies on a particular choice for the smooth and complex shorelines. In order to test sensitivity and error in shoreline selection, we examine adding varying amounts of noise to the nominal hand-selected shoreline position. Obtaining meaningful results, however, requires generating potential shorelines which have characteristics that are similar to the actual shoreline. We show in the following paragraphs that the traced shoreline of Ontario Lacus is well described as a fractal, and that results are robust with respect to plausible alternate shoreline tracings generated with similar fractal character.

It is well established that natural landscapes can often be described using a fractal relationship between measurement length-scale and the amplitude of topographic variation [Mandelbrot and Wheeler, 1983, Turcotte, 1997]. One of the first and simplest applications of fractal analysis to natural geomorphic phenomena was the analysis of the British coastline by Mandelbrot [1967]. In this and many subsequent investigations (e.g. Phillips [1986], Jiang and Plotnick [1998], Schwimmer [2008], Sharma and Byrne [2008]), researchers have noticed that coastlines are often found to follow an allometric relationship:

$$L(s) \propto s^{1-D} \tag{3.5}$$

where $L(s)$ is the observed length of a section of coastline using a measure stick of length s, and D is the fractal dimension of the coastline. We have observed an allometric relationship for the extended smooth region of Ontario's eastern shoreline using the divider method

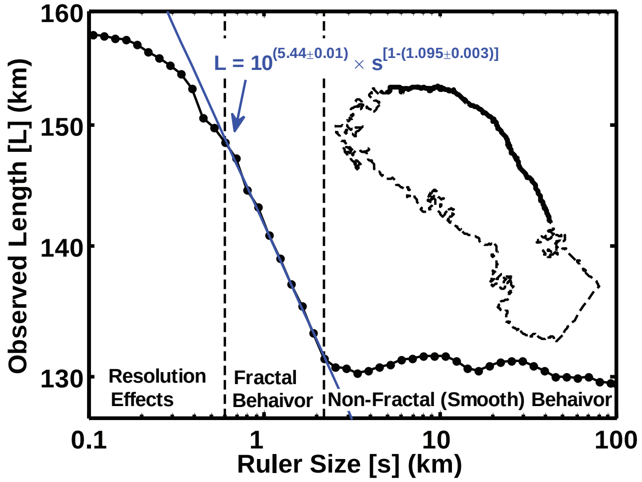

Figure 3.5: Allometric relationship between ruler size (s) and observed length (L) for the eastern shore of Ontario Lacus. Fractal behavior is observed between SAR image resolution (few hundred meters) and s ∼2 km with a fractal dimension $D = 1.095 \pm 0.003$. The analyzed section Ontario's shoreline is shown in bold on the dashed outline.

defined in Klinkenberg and Goodchild [1992]. From Figure 3.5, it is clear that the shoreline trace is well described as a fractal with $D = 1.095 \pm 0.003$ on length-scales between the SAR image resolution (260-350 m) and $\sim$ 2 km. At length-scales larger than this crossover length, fractal behavior breaks down yielding a smooth shoreline. While we do not investigate the cause of this behavior here, it may be the result of wave action or some other erosional mechanism operating predominantly at larger length-scales.

We generate fractals using the spectral method described in Saupe [1988] in order to test our sensitivity to shoreline selection. This method is based on how the scale dependence of a fractal feature expresses itself in the features's power spectrum. Saupe [1988] shows that the power spectral density of a fractal curve can be expressed as

$$P(k) = Ak^{-\beta} \tag{3.6}$$

where k is the spatial frequency and the exponent is related to the fractal dimension D with $\beta \equiv 2(1-D)+3n_{\mathrm{d}}$, where n_{d} is the spatial dimension. The integral of $P(k)$ (total power) is equal to the integral of the square of a given realization (Parseval's Theorem) and is used to set A for a given RMS amplitude. Using this relation, we generate a random fractal by creating a power spectrum with the desired fractal and spatial dimensions, and then taking the inverse Fourier transform after randomizing the phases of each frequency. This procedure is applied down to the fractal crossover of $\sim$ 2 km, with zero power at lower frequencies. In the following paragraphs, we use this method in one and two dimensions in order to explore model sensitivity to shoreline selection and small-scale lakebed topography.

Sensitivity to shoreline selection is studied using one-dimensional fractals as realistic noise sources added perpendicular to the local shoreline trend. Alongshore-averaged backscatter and best-fit parameters to Equation 3.2 are evaluated using distance bins recalculated for the new shoreline. The calculation is repeated 100 times for each noise amplitude. Figure 3.6A shows the percentage of shoreline models whose skewness values are inconsistent with exponential attenuation in region A. For shorelines with RMS noise amplitudes of >0.7 km, 95% of the models are inconsistent with ExM, requiring draws from multiple $\sigma_{\mathrm{o}}^{(\mathrm{t})}$ distributions. Pixel resolution varies from 280-350 m in range and 260-280 m in azimuth, suggesting shorelines were selected to better than ~2 pixel accuracy. The best-fit imaginary refractive index (Figure 3.6B), which decreases with added shoreline noise, varies only slightly below the lower bound of its 95% CI over this region (4.6 vs. 4.8×10^{-4} for 95% detectability confidence, see Figure 3.6). LMs generated using the artificially noisy shorelines have large skewness, similar to Figure 3.4, and are hence all distinguishable from exponential attenuation. While this method of adding noise does not completely capture realistic variations in shoreline selection, as would a double-blind control experiment, it does provide a reasonable representation that offers the advantage of numerical convenience and speed.

In addition to assuming accurate shoreline selection, we also asserted that bathymetry contours are parallel to the local shoreline. The amplitude of small-scale variations in lakebed depth, which result in deviations from this assumption, are the second primary source of error in our analysis. Speckle noise prevents measuring small-scale variations in lakebed topography from σ_{o} itself, thus we investigate its effects using two-dimensional fractal surfaces which are added to an average local slope following Equation 3.6. After generating the surfaces, we test how the fractal dimension of the topographic model relates to the fractal character of its shoreline using a range of noise amplitudes and fractal dimensions. We find that if the underlying topography model is assumed to be fractal up to the crossover length-scale, we can easily detect this as a break in fractal slope of the shoreline as is observed for Ontario. Conversely, when we generate topographic models that are fractal at all length-scales, we find no break in slope for the corresponding shoreline. This suggests that the underlying topographic deviations from the local slope in the near-shore region of Ontario likely contains a fractal crossover at $\sim$ 2 km, which can be verified visually. We also observe that the fractal dimension of the topographic noise model is not necessarily equivalent to the fractal dimension of the resulting shoreline. Accordingly, we adopt a practical approach of assuming a range of plausible fractal dimensions for the noise to test the robustness of results. While the actual fractal dimension of the topography surrounding Ontario is interesting and may warrant further investigation, we do not attempt to calculate it here. Instead, the fractal model is used to verify the validity of our assumptions against reasonable topographic variations.

Using a fractal surface to approximate topographic noise, we now test our sensitivity to local variations in lake depth. We perform this test using a range fractal dimensions between $D = 2.05$ and $D = 2.5$ up to the crossover at 2 km. The validity of our model is tested by generating fractal noise surfaces, which are then added with varying amplitude to constant local slopes. For each model, SAR images are generated using backscatter values determined from Equation 3.2 with the best-fit coefficients for region A and a high-resolution depth map from the fractal noise model. After adding speckle noise, images are analyzed using the same process described in Sections 3.2 and 3.3 by assuming that depth bins lie parallel to the local shoreline. For each model, we assess how added topographic noise affects both the best-fit parameters and recorded statistical metrics in each depth-bin. For the two-dimensional equivalent of the observed fractal dimension of Ontario's eastern shore, we find that the best-fit value for κ does not vary outside its observed 95% CI for RMS noise amplitudes of up to 1.2 m (Figure 3.7). For larger noise amplitudes, there was greater than a 95% probability that skewness values of depth-bins in synthetic SAR images would be greater than the upper 95% CI of those generated by ExM. For other fractal dimensions, the noise amplitude for 95% detectability confidence (Figure 3.7 caption) varied slightly, but the best-fit values of κ never exceeded the observed 95% CI prior to crossing this threshold. This suggests that small-scale variation in lakebed backscatter would produce detectable increases in skewness before affecting the best-fit value of κ.

In summary, the combination of differences in skewness and residual chi-square favor backscatter values dominated by exponential attenuation in a deepening liquid medium, as opposed to either linear mixing or significant small-scale topographic deviation from a smooth plane. When the amount of linear mixing or amplitude of small-scale lakebed topography becomes large enough to significantly impact the derived model parameters, the skewness of pixel distributions in the transition region becomes identifiably large. These results justify the simplifying assumptions of accurate shoreline determination and bathymetry contours which are parallel to the local shoreline. The morphologic correlation between relative slope and shoreline features, discussed Section 3.5, also supports the validity of our analysis.

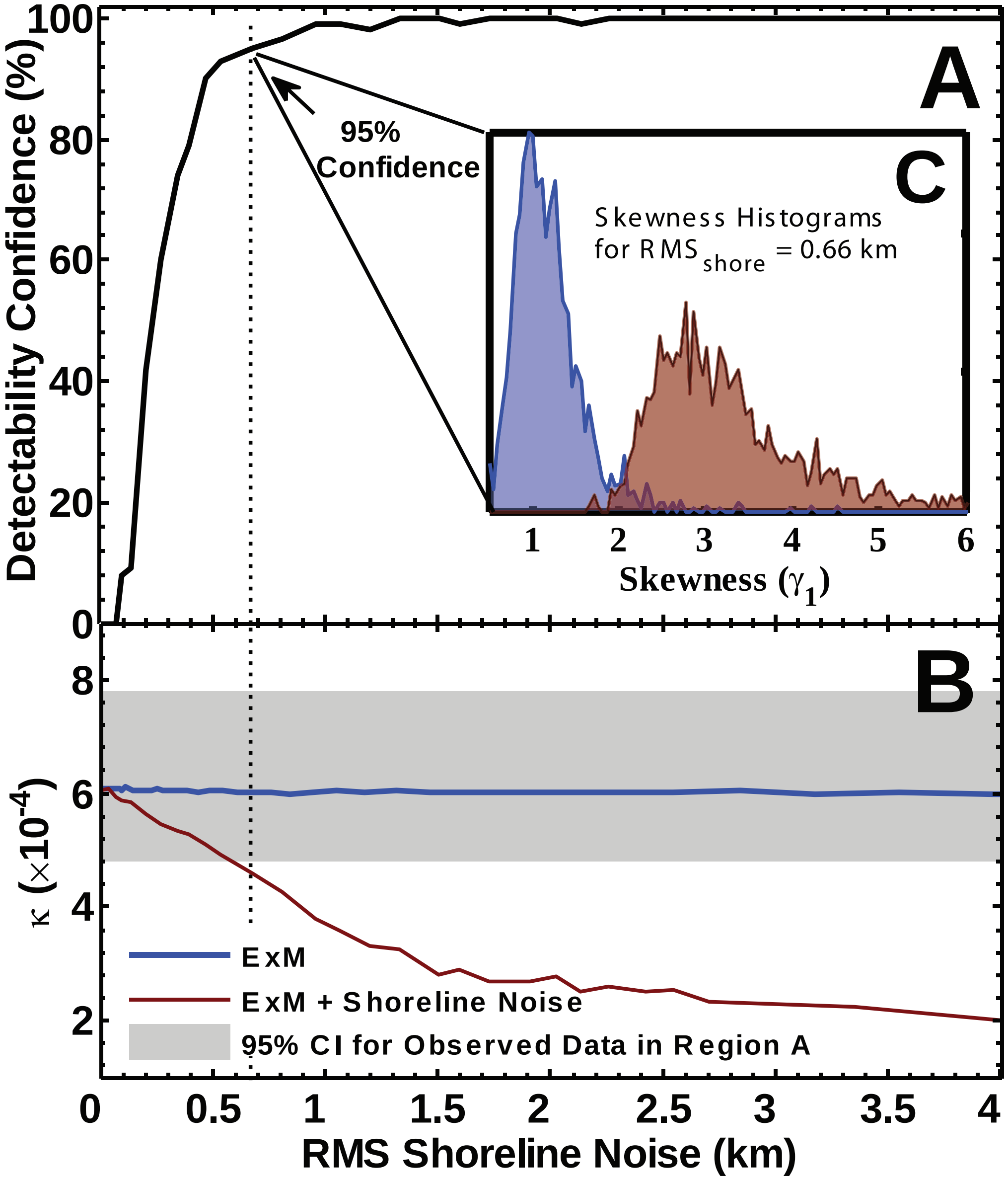

Figure 3.6: Effect of shoreline selection for region A. Abscissa denote RMS half-amplitudes of fractal error introduced into the shoreline position. Peak half-amplitudes are approximately twice the RMS. Pixel scale varies from 280-350 m. A: Detectability Confidence, defined as the fraction of analysis runs for which transition region skewness is outside the 95% CI of the expected distribution from exponential attenuation. B: Best-fit imaginary refractive index (κ) derived using the noise modified shoreline. The mean κ (dotted red line) remains above the lower 95% CI for 0 shoreline error for up to 90% Detectability Confidence, suggesting minimal error contribution from mixing in the reported $\kappa = (6.1^{+1.7}_{1.3}) \times 10\ ^{4}$. C (Inset): Distribution of skewness values from model runs with 0 and 0.67 km RMS shoreline noise (95% Detectability Confidence).

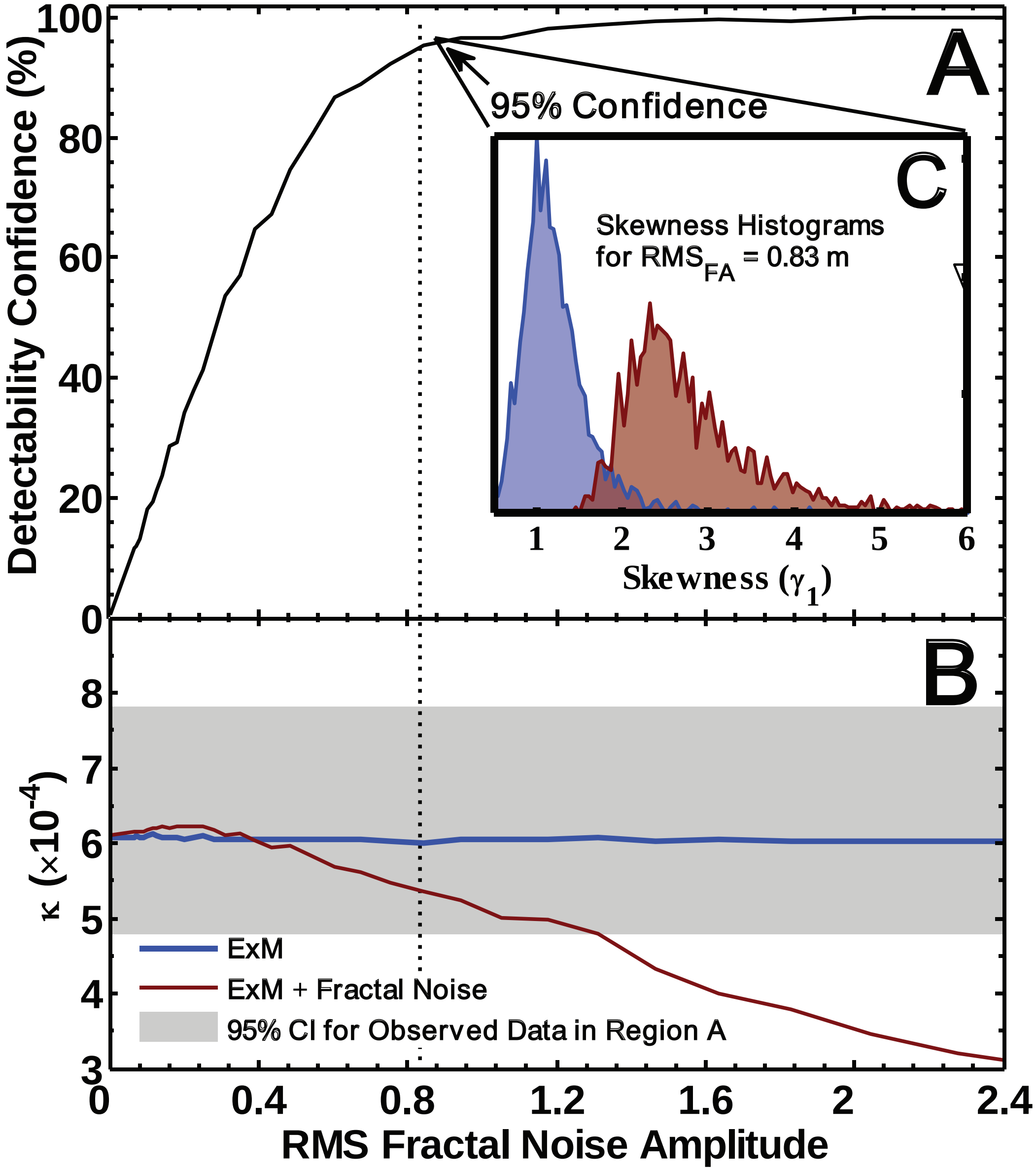

Figure 3.7: Effect of small-scale topography for region A. Abscissa denote RMS half-amplitudes of added fractal noise. Peak amplitudes are approximately five times the RMS. The noise amplitude for which there is a 95% probability of detecting an anomalous skewness is shown. A: Detectability Confidence, defined as the fraction of analysis runs for which transition region skewness is outside the 95% CI of the expected distribution from exponential attenuation assuming smooth topography. B: Best-fit imaginary refractive index (κ) using σ_{o} derived from fractal topography. The mean κ remains above the lower 95% CI of the observed data for up to 95% Detectability Confidence, suggesting minimal error contribution from small-scale topography in the reported $\kappa = (6.1^{+1.7}_{1.3}) \times 10^{\;4}$. C (Inset): Distribution of skewness values from models runs using 0 and 0.83 m RMS amplitudes (95% Detectability Confidence).

3.5 Discussion

In this chapter we find the first empirical estimate of the imaginary dielectric properties of liquid hydrocarbons on Titan using Cassini observations. Assuming a real dielectric constant of 1.75 for liquid hydrocarbon [Paillou et al., 2008a], the complex index of refraction of region A corresponds to a loss tangent $\tan\Delta = (9.2^{+2.5}_{-2.0}) \times 10^{-4}$ ($\tan\Delta \approx \frac{2k}{\sqrt{\epsilon_r}}$, where ϵ_r is the real component of the dielectric constant). This value is consistent with experimental measurements of liquid natural gas (LNG) at 13 GHz ($\tan\Delta_{\mathrm{LNG}} = 1.1 \times 10^{-3}$) [Paillou et al., 2008a] and the 10^{-3} upper limit for ethane and methane loss tangents at 1.2 GHz calculated by Sen et al. [1992]. LNG is primarily composed of methane ($> 90\%$), with smaller amounts of higher-order hydrocarbons. The measured loss tangent is inversely proportional to the average effective topographic slope, or dip, at the intersection with the altimetry profile near region A ($D_{\mathrm{A}} = (2 \pm 0.1) \times 10^{-3}$), and is consistent with a bulk composition of liquid hydrocarbons. More finely resolved along-track altimetry profiles may reveal slope breaks in the shoreline setting; such variations in slope would proportionally affect the best-fit value for κ and derived bathymetric slopes [Ford, 2010]. The low value determined for the loss tangent suggests that Ontario's margins do not have large amounts of suspended absorptive material, such as tholin ($\tan\Delta \sim 2 \times 10^{-2}$ [Paillou et al., 2008a]).

Reported values for κ and other model coefficients assume that near-shore lakebed backscatter ($\sigma_{\mathrm{o}}^{(2)}$) does not significantly vary within the regions of interest. The observed exponential drop-off in backscatter supports this assumption, as variations in $\sigma_{\mathrm{o}}^{(2)}$ would disrupt this trend. In addition, changes in study region size does not alter the best-fit model coefficients, adding further support. Lastly, $\langle\sigma_o\rangle$ values just outside Ontario's shoreline do not significantly vary within the any of the regions of interest. Given the observations of shoreline recession [Turtle et al., 2009b, Hayes et al., 2011], these regions may represent previous lakebed surfaces. However, areas of high backscatter are observed within Ontario Lacus in both T57/T58 and T65 (Figure 3.1). These features are located far from the study areas and suggest that Ontario is shallower or has significantly brighter lakebed in these regions.

The composition of Titan's lakes is likely a mixture of ethane, methane and propane, with smaller abundances of nitrogen and higher-order hydrocarbons and nitriles [Cordier et al., 2009, Lunine et al., 1983]. Assuming thermodynamic equilibrium at 90K, the methane to ethane ratio of a surface lake is 1:8 [Cordier et al., 2009]. For a raindrop or recently precipitated liquid body, the expected composition is 25% nitrogen and 75% methane [Lorenz, 1993]. While VIMS spectra confirm the presence of liquid ethane in Ontario [Brown et al., 2008], the instrument was incapable of estimating its abundance or distinguishing liquid from atmospheric methane. Measurements of the cryogenic microwave optical properties of pure methane and ethane, in additional to other Titan relevant materials, are in development [Barmatz and Mitchell, 2009]. When these measurements become available, the complex dielectric constant of various mixtures can be compared to the observed loss tangent of Ontario Lacus, providing tests for the predicted liquid compositions.

In areas where Ontario's shore does not intersect the T49 altimetry track, the coefficients of Equation (3.2) can be used to estimate local bathymetric slope, assuming uniform refractive properties for the liquid. Along the eastern shore of Ontario (regions B, C, D, E, F), bathymetric slopes are consistent within errors and similar to the measured topographic slope at A (mean values of $(2.2-2.7)\times10^{-3}$ vs. 2.0×10^{-3}, see Figure 3.1 and Table (3.1)). In this area, the shoreline is smooth and morphologically similar to a beachhead modified by either persistent wave action or periodic oscillation in lake level [Wall et al., 2010]. West of region F, bathymetric slopes shallow slightly (regions G and H) prior to increasing as the shoreline approaches intersection with the bright mountainous terrain which forms its northernmost borders. In most of this area the transition region is of order 1 pixel, hindering analysis and suggesting bathymetric slopes greater than 0.1 ($\sim \frac{d_{\mathrm{trans.}}}{\Delta x_{\mathrm{pix}}}$). The best-fit slope in region I, the only region in the area with a smooth shoreline segment and relatively low skewness, was $D_{\mathrm{I}} = (4.8^{+1.0}_{-2.0}) \times 10^{-3}$, although only three points lie within the first two exponential skin depths. Additional measurements of topographic slope will become available after stereo processing has been completed between T57/T58 and T65 SAR observations. When this data is available, the bathymetric slopes reported in Table 3.1 can be compared to the near-shore topographic slopes on the landward side of Ontario's shoreline.

The western shore of Ontario (regions J, K, L, and M) has shallower bathymetric slopes as compared to the eastern shore ($(0.4-1.2)\times10^{-3}$ vs. $(1.8-2.7)\times10^{-3}$). This observation is consistent with the larger values of shoreline recession observed between the 2005 ISS and 2009 SAR images of this coast [Hayes et al., 2011]. Region K is located near deltaic lobate structures fed by a large tributary system extending toward the lake from the west. The returned bathymetric slope near the deltaic-like features are 1.4 times lower than the effective topographic slope of $D_{\mathrm{L}} = (1\pm0.5)\times10^{-3}$, as derived from altimetry echo center-of-mass near region L. Gently sloping depth profiles near these features are consistent with a multi-lobe shallow-water delta created from distributary channel switching [Wall et al., 2010].

Region L intersects T49 and has a bathymetric slope value consistent with the topographic slope calculated using the altimetry data. The effective bathymetric slope in region M, located in Ontario's southeast corner, is 4 times shallower than the topographic slope observed at A. This region also contains a lower average $\langle \sigma_{\mathrm{o}} \rangle$ within the lake (-14 dB $\pm$ 3 dB) and is near the largest observations of shoreline recession observed between the ISS and SAR images [Hayes et al., 2011]. The inverse proportionality between local bathymetric slope and shoreline recession magnitude suggests a uniform drop in lake level.

3.6 Summary

SAR backscatter in the near-shore region of Ontario Lacus is observed to fall off exponentially with perpendicular distance from the local shoreline. Closest-approach altimetry observations suggest that Ontario lies in a shallow regional basin with slopes of $\sim 10^{-3}$. Together, these observations allow the derivation of the liquid's complex index of refraction through comparison of $\langle \sigma_{\mathrm{o}} \rangle$ to a simple two-layer model with exponential dependence on lake depth (Equation (3.2)). Model coefficients are derived using non-linear least squares minimization of reduced chi-square (Equation (3.2)). Error estimations show that the observed bathymetric slope variations are significant.

The derived imaginary component of the refractive index is $\kappa = (6.1^{+1.7}_{-1.3}) \times 10^{-4}$ and corresponds to a loss tangent of $\tan\Delta = (9.2^{+2.5}_{-2.0}) \times 10^{-4}$, supporting the prediction that Ontario is filled with liquid hydrocarbons. This value is inversely proportional to the observed near-shore altimetric slope $D_{\mathrm{A}} = (2 \pm 0.1) \times 10^{-3}$, consistent with previous laboratory estimates and model extrapolations of methane and ethane loss tangents, and will help constrain Ontario's liquid composition when additional laboratory data become available. Significant amounts of highly absorptive material, such as tholins, are inconsistent with the measured loss tangent. The loss tangent can also be used to translate temporal backscatter variations into depth changes within Titan's lakes.

In areas where altimetry does not intersect Ontario's shore the derived model coefficients imply local slopes. Absolute bathymetric slopes are calculated for eleven areas around Ontario, and a coarse bathymetry map follows by referencing to the observed on-land altimetry slopes at regions A and L (Figure 3.1). The relative variation in these slopes is independent of derived optical properties and altimetric profiles. Bathymetric slope values on the eastern shore, which exhibits a beachhead morphology, are characteristically steeper than the western shore, where a more complex shoreline exists. The shallowest bathymetric slope occurs in the southwestern tip of Ontario, where the greatest magnitude of shoreline recession has been observed [Hayes et al., 2011]. Bathymetric slope estimations are consistent with and complement observed morphology.

Acknowledgements

The authors would like to thank Bryan Stiles for helpful discussions and the Cassini engineering team, without whom the data presented here would not have been possible.

Chapter 4

Seasonal Variation

Originally published in

A. G. Hayes, O. Aharonson, J. I. Lunine, R. L. Kirk, H. A. Zebker, L. C. Wye, R. D. Lorenz, E. P. Turtle, P. Paillou, G. Mitri, S. D. Wall, E R. Stofan, K. L. Mitchell, C. Elachi, and The Cassini RADAR Team. Transient Surface Liquid in Titan's Polar Regions from Cassini. Icarus, 211, 2011. doi: 10.1016/j.icarus.2010.07.017

Abstract

Cassini RADAR images of Titan's south polar region acquired during southern summer contain lake features which disappear between observations. These features show a tenfold increases in backscatter cross-section between images acquired one year apart, which is inconsistent with common scattering models without invoking temporal variability. The morphologic boundaries are transient, further supporting changes in lake level. These observations are consistent with the exposure of diffusely scattering lakebeds that were previously hidden by an attenuating liquid medium. We use a two-layer model to explain backscatter variations and estimate a drop in liquid depth of approximately one meter-per-year. On larger scales, we observe shoreline recession between ISS and RADAR images of Ontario Lacus, the largest lake in Titan's South Polar region. The recession, occurring between June 2005 and July 2009, is inversely proportional to slopes estimated from

altimetric profiles and the exponential decay of near-shore backscatter, consistent with a uniform reduction of 4 ± 1.3 m in lake depth.

Of the potential explanations for observed surface changes, we favor evaporation and infiltration. The disappearance of dark features and the recession of Ontario's shoreline represents volatile transport in an active methane-based hydrologic cycle. Observed loss rates are compared and shown to be consistent with available global circulation models. To date, no unambiguous changes in lake level have been observed between repeat images in the north polar region, although further investigation is warranted. These observations constrain volatile flux rates in Titan's hydrologic system and demonstrate that the surface plays an active role in its evolution. Constraining these seasonal changes represents the first step toward our understanding of longer climate cycles that may determine liquid distribution on Titan over orbital time periods.

4.1 Introduction

Titan's active methane-based hydrologic cycle is unique among the extraterrestrial bodies of our solar system. As such, observing seasonal variations in Titan's volatile system is the primary goal of the Cassini spacecraft's Equinox ($2008 - 2010$) and Solstice ($2010 - 2017$) missions [Brown et al., 2010]. Herein we describe the discovery of ephemeral liquid disappearing from the surface of Titan during southern summer. Our observations include a collection of transient lacustrine features as well as a recession in the shorelines of Ontario Lacus. Observations were acquired using the Ku-Band Cassini RADAR (λ=2.2 cm) and returns are used to model liquid depths and link surface change to theoretical predictions of volatile transport in Titan's hydrologic system. These ephemeral features represent direct evidence for surface liquid playing an active role in Titan's methane cycle.

Lacustrine features identified on Titan [Stofan et al., 2007a, Hayes et al., 2008a, Mitchell et al., in preparation] have been grouped into three classes: empty lake basins, partially filled lakes, and dark or liquid-filled lakes [Hayes et al., 2008a]. Partially filled lakes have radar returns consistent with incident radiation penetrating a liquid layer and interacting with the lakebed, while dark lakes completely reflect and absorb the incident microwave energy [Hayes et al., 2008a, Paillou et al., 2008b]. Empty lakes are brighter than their exteriors in both nadir and off-nadir observations, suggesting compositional variations. Higher relative backscatter at large off-nadir angles ($\theta > 30°$) also suggests a stronger volume scattering component [Hayes et al., 2008a]. All lake classes are restricted to latitudes poleward of 55° and cover 1.5% of Titan's observed surface. There is a significant dichotomy in polar lake distributions, with dark lakes covering 10% of the area in the north but only 0.4% in the south (poleward of 55°) [Hayes et al., 2008a, Aharonson et al., 2009]. Aharonson et al. [2009] attributes this dichotomy to a seasonal asymmetry in incident flux caused by Saturn's eccentricity and Titan's solar longitude of perihelion. Observed ephemeral features are initially consistent with partially filled lakes and later transition into features similar to empty lake basins.

Ephemeral features are located in the south polar region (55°S-90°S), where 9% of the surface has been observed by multiple Synthetic Aperture Radar (SAR) swaths. Including $\sim$1 km/pixel high altitude SAR (HiSAR) measurements [West et al., 2008], the repeat coverage increases to 32%. Between October 2004 (Cassini flyby TA) and January 2010

(T65), the Cassini spacecraft has acquired SAR images, at a resolution of ∼300 m/pixel, covering 35% of Titan's surface and 45% of the areas poleward of $55°$. Including HiSAR, the global and polar coverage increases to 45% and 60%, respectively. These radar observations allow for the identification and analysis of temporal variation in the polar regions with baselines of up to three years. We identify and model examples of transient surface liquid observed by the RADAR instrument and compare estimated loss rates to global circulation models (GCM). During the observation period (September 2005 - January 2010), Titan's south polar region was in late summer and expected to be in a state of volatile evaporation [Mitchell, 2008, Newmann and Richardson, 2009]. Available repeat coverage of the north polar region allows us to identify only one area where surface change can be unambiguously separated from variations in observational geometry, although additional observations of the north are planned during Cassini's Solstice mission.

Below, we present observations, analyses, and their implications. Section 4.2 describes the analysis and modeling of the backscatter from lacustrine features in preparation for comparison against observed ephemeral features. Section 4.3 describes the details of the ephemeral feature observations and their viewing geometries, including morphologic descriptions and the implications of Ontario Lacus shoreline recession. In Section 4.3 we also develop a simple two-layer model in order to estimate the changes in lake levels required by the radar data. Potential explanations for the surface change, their implications regarding Titan's volatile system, and comparison to previous theoretical predictions are described in Section 4.4.

4.2 Radar Backscatter of Lacustrine Features on Titan

The disappearance or alteration of lacustrine features may result from two classes of explanations. The first is observational or instrumental effects; the second is physical changes on the surface of Titan. Observational effects include variation in radar backscatter due to different incidence, azimuth, and polarization angles between Titan passes. Backscatter can vary significantly as a function of these angles, depending on surface and subsurface properties such as composition, roughness, and degree of volume scattering. The possibility that these effects are the only important phenomena determining backscatter variation will be referred to as the null hypothesis. Alternatively, ephemeral observations may be due to surface changes including liquid evaporation, infiltration, freezing, wave activity, and cryovolcanism.

In order to discount the null hypothesis as an explanation for observed changes, we will review the backscatter variations from all lacustrine features on Titan and use their response as a comparison point for discussing ephemeral feature backscatter in Section 4.3. The microwave reflectivity of Titan's surface is reported using the normalized backscatter cross-section (σ_o), a non-dimensional quantity that describes received radar power as compared to an isotropically scattering surface. In order to derive σ_o, an effective area is defined that is equal to the size of the isotropic scatterer required to produce the measured power. The effective area is then divided by the imaged surface area to create a non-dimensional σ_{o} [Ulaby et al., 1982].

The normalized backscatter cross-section of the icy Galilean satellites show that they are diffusely scattering bodies dominated by complex volume scattering within a porous icy regolith [Black et al., 2001, Ostro et al., 1992]. When viewed at resolutions comparable to their radius, the Saturnian satellites Enceladus, Tethys, Dione, Rhea, Iapetus, Hyperion, and Phoebe are also dominated by diffuse scattering and have comparable electrical properties to their Galilean counterparts [Ostro et al., 2006]. Terrains on Titan, however, have a surface term which requires a Kirchhoff scattering component in addition to the expected diffuse behavior [Campbell et al., 2003, Wye et al., 2007, Janssen et al., 2009]. Sufficiently accurate high-resolution data do not exist to see if this is also true for the other Saturnian satellites. Kirchhoff scattering is common among the inner solar system bodies [Muhleman, 1995] and attributed to quasi-specular Fresnel reflection off surface facets which are oriented toward incoming radiation and smooth compared to the radar wavelength [Beckmann and Spizzichino, 1963, Wye et al., 2007].

Quasi-specular (QS) backscatter is typically modeled by a surface whose elevation departure from a smooth, perfectly conducting plane follows a Gaussian probability distribution [Elachi and van Zyl, 2006]. The horizontal structure of this surface is often described using an autocorrelation function. One commonly used autocorrelation function is also Gaussian [Hargreaves, 1959] and produces a backscatter model of the form (denoted Gaussian):

$$\sigma_{o,\text{ Guass}} = \frac{\rho C}{\cos^4 \theta} e^{-C \tan^2 \theta} \tag{4.1}$$

where ρ is the Fresnel reflection coefficient at normal incidence, $C^{-1/2}$ is the surface RMS slope, and θ is the incidence angle. The constant C is described using a tilt angle θ_{RMS} such that $C^{-1} = \tan^2 \theta_{\text{RMS}}$. Another common autocorrelation function is exponential [Daniels, 1961] and yields the Hagfors scattering model [Hagfors, 1964]:

$$\sigma_{o,\text{ Hag.}} = \frac{\rho C}{2\cos^6\theta}\left[1 + C\left(\frac{\tan\theta}{\cos\theta}\right)^2\right]^{-3/2} \tag{4.2}$$

The Hagfors model is commonly used to describe radar backscatter from the lunar surface [Hagfors, 1970, Simpson and Tyler, 1982] while the Gaussian model has been shown to fit radar returns from portions of the Venusian surface [Tyler et al., 1992, Sultan-Salem and Tyler, 2006]. The Hagfors model has also been used to model the specular portions of radar returns from Titan [Campbell et al., 2003, Wye et al., 2007]. Other quasi-specular backscatter models can be derived by assuming other forms for the autocorrelation function.

Diffuse backscatter generally dominates radar echos at large incidence angles ($\theta > 30°$) while facet scattering dominates at low incidence angles [Elachi and van Zyl, 2006]. Diffuse backscatter can arise from small-scale surface roughness and/or subsurface volume scattering and is typically modeled using a cosine to a power of the form:

$$\sigma_{o,\text{ Diff.}} = A\cos^n\theta \tag{4.3}$$

where A is a the diffuse signal power and n is the cosine power. Fits to early Cassini scatterometry observations of Titan at large incidence angles yield $A = 0.34$ and $n = 1.22$ for the combined dataset [Wye et al., 2007]. These values are consistent with previously published values for the icy Galilean and Saturnian satellites [Wye et al., 2007]. Polarization and azimuth angle effects are neglected in both the quasi-specular and diffuse models presented above.

We use two-component models consisting of quasi-specular (Hagfors or Gaussian) and diffuse components to describe radar backscatter values for both empty and partially filled lake features on Titan. Figure 4.1 shows the backscatter values for 110 empty lakes and 101 partially filled lakes distributed globally. Both distributions can be described using the sum of a Gaussian quasi-specular and a diffuse component. Because SAR data are rarely acquired much above 40° incidence, we cannot properly estimate the diffuse component from these data alone. For this reason, we presume a cosine power law of $n = 1.22$, equivalent to that estimated by Wye et al. [2007], and allow the amplitude of the diffuse term to vary. Hagfors models do not match the lake data as well as the Gaussian model at low incidence angles. Average backscatter values for the regions immediately surrounding the lake features are best-fit using a Hagfors quasi-specular component. The model parameters for the surrounding regions are found to be similar to those derived by Wye et al. [2007] using Cassini scatterometry for regions elsewhere on Titan's surface. We plot the best-fit models for lake features as dashed lines in Figure 4.1 and list model parameters in Table 4.1.

The empty lake observations are self-consistent within their feature class (as defined by the methods outlined in chapter 2) and distinct from the best-fit quasi-specular plus diffuse scattering model that describes the partially filled lake radar returns. The amplitude of the diffuse scattering term for the empty lake data ($A_{\text{emp Guass.}} = 0.55 \pm 0.07$, $A_{\text{emp Hag.}} = 0.41 \pm 0.12$) was significantly higher than the best-fit for the surrounding region ($A_{\text{sur Guass}} = 0.38 \pm 0.03$, $A_{\text{sur Hag.}} = 0.34 \pm 0.04$) and partially filled lakes ($A_{\text{par Guass}} = 0.11 \pm 0.02$, $A_{\text{par Hag.}} = 0.06 \pm 0.04$). It is important to note, however,

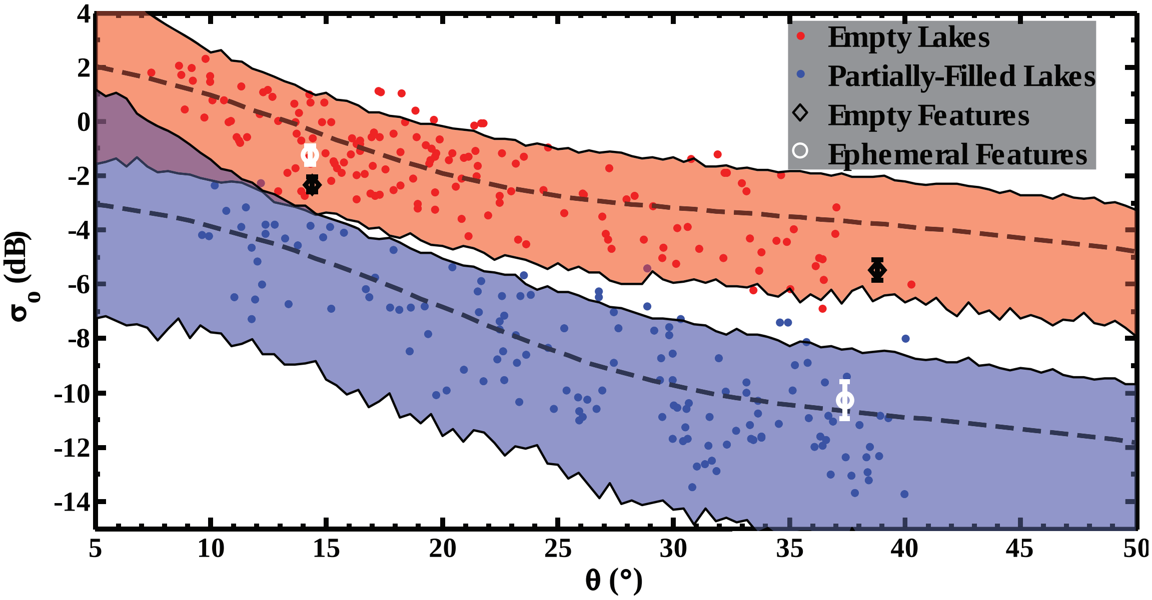

Figure 4.1: Backscatter (σ_o) values for partially filled and empty lakes observed on Titan. Red and blue shading represent 95% confidence interval in model output of the mean backscatter of pixels contained within each feature class. The dashed lines are the best-fit models. Model parameters are listed in Table 4.1. $\langle\sigma_o\rangle$ for empty and ephemeral lakes from Region 1 (T39/T55) are over-plotted in black and white, respectively. Note that ephemeral features are initially consistent with the partially filled lake class and later consistent with the empty lake class.

that a non-zero diffuse scattering component is required to accurately describe all observed features. The increase in diffuse scattering for the empty lake beds, as compared to the surrounding terrain, can be used as a constraint for formation hypothesis. One hypothesis, discussed in Mitchell et al. [in preparation], suggests that these features are formed through karstic dissolution. Dissolution chemistry would produce higher porosity and subsurface structure beneath lakebeds, enhancing their diffuse volume scattering. However other hypotheses, such as cracking in evaporative lakebed deposits, may also be consistent with the observed backscatter variations. Figure 4.2 shows backscatter values for an empty lake and a partially filled lake which were observed at multiple incidence angles. Both features were observed in the north polar region during the winter season when Mitchell [2008], Newman et al. [2008], and Graves et al. [submitted] predict evaporation and precipitation to be minimal. The predictions of Tokano [2009b] vary based on predominate liquid composition. In the case of ethane-rich seas ($< 17\%$ $\mathrm{CH_4}$), Tokano [2009b] also predicts winter evaporation over the northern lakes to be minimal. For methane-rich seas ($> 62\%$ $\mathrm{CH_4}$), however, Tokano [2009b] predicts evaporation to be at its peak during the winter season. Observations of the north polar region acquired in December 2009 (T64) show no unambiguous examples of surface change, supporting Mitchell [2008], Newman et al. [2008], and Graves et al. [submitted] (Section 4.3). Observations of the empty lake depicted in Figure 4.2 were acquired over a period of 9 months, and the best-fit model parameters (holding the cosine power constant) have values similar to the empty lake class (Table 4.1). The partially filled lake, which was observed over a period of 7 months, shows no change in its morphologic boundaries and has backscatter variation consistent with a Gaussian plus diffuse scattering model with parameters similar to that of the partially filled lake class.

The shape of the quasi-specular scattering component is determined by the roughness parameter C. For large values of C (small θ_{RMS}) the point at which the backscatter function transitions from steep to shallow dependence on incidence moves toward lower angles. For a given incidence angle, there is a maximum value of C beyond which the backscatter decreases, requiring an increase in the Fresnel reflection coefficient, and hence dielectric constant, in order to account for the increase in σ_o. To adequately match the radar returns of empty lake basins and surrounding terrain at low incidence angles, dielectric constants of $\sim$3 are required. Passive radiometry observations suggest real dielectric constants $\epsilon_{\mathrm{r}} = 1.7 \pm 0.2$ for most of the equatorial and polar regions of Titan [Elachi et al.,

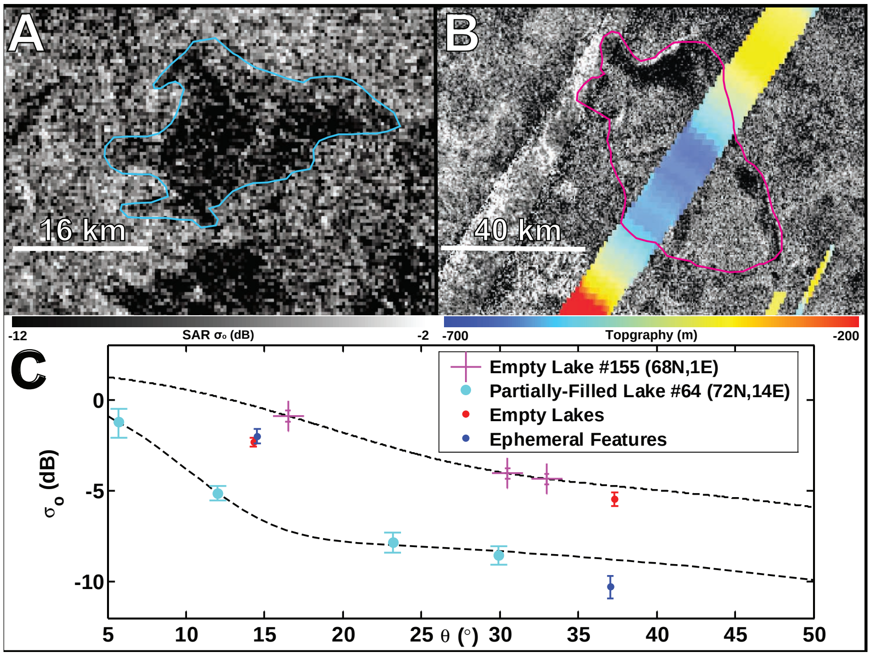

Figure 4.2: Backscatter (σ_o) variation for an individual partially filled (cyan) and empty (magenta) lake observed at multiple incidence angles. Images are equidistant cylindrical projections with a logarithmic stretch from -20 to 2 dB. A: partially filled lake feature ($\#64$). B: Empty lake feature ($\#155$). C: Backscatter (σ_o) values for partially filled lake $\#64$ and empty lake $\#155$ with best-fit Gaussian scattering models depicted by dashed black lines. Red and blue dots represent empty lakes and ephemeral features in Region 1 (T39/T55). All error bars represent 95% confidence on mean backscatter. Fit parameters are listed in Table 4.1.

2005, Janssen et al., 2009]. The Permittivity, Waves, and Altimetry (PWA) instrument onboard the Huygens probe also found a surface dielectric constant of $\sim$2 [Grard et al., 2006]. While the PWA operate at kilohertz as opposed to gigahertz frequencies, the real dielectric constant of most Titan-relevant materials, including water ice and hydrocarbon, is relatively consistent over this range at 95 K [Grard et al., 2006, Sen et al., 1992]. The composition of terrain in Titan's polar regions is expected to be a porous mixture of water ice ($\epsilon_{\mathrm{r}} = 3.13$), tholin ($\epsilon_{\mathrm{r}}$=2.0-2.4), and liquid hydrocarbon (ϵ_{r}=1.7-1.9) [Lunine, 1993, Paillou et al., 2008a, Thompson and Squyres, 1990]. While model parameters derived here are consistent with the upper end of dielectric constants for these materials, they should not be taken at face value given that we lack very low-angle data ($\theta < 10^{\circ}$) and proper estimates of the diffuse component. Composite dielectric constants greater than 3 are not expected and the quasi-specular scattering models considered may be oversimplified and unrepresentative. Complex scattering effects or multi-layer models, such as subsurface ice cylinders observed in Greenland [Rignot et al., 1993] or Mie scattering from cm-scale cobbles [Le Gall et al., 2010], may be required to explain the low incidence angle behavior of backscatter on Titan. However, deriving a more complex model for radar backscatter of Titan's hydrologic features is beyond the scope of this work. The purpose of backscatter modeling herein is to verify that the observed backscatter variations described in the following sections represent temporal surface change and cannot be explained by variations in incidence, azimuth, or polarization angles (null hypothesis).

Table 4.1: Model parameters for empty and partially filled lake observations. Parameters that were held constant during fitting are denoted with a *. Dielectric constant (ϵ_r) is held constant and model preferences are not reported for Regions 1 and 2 because there are only two independent data points. The Hagfors model could not be used to model Empty Lakes $\#34-36$, as it required non-physical values for the Fresnel reflection coefficient. The model which best-fit each data set are emphasized with a †. Errors represent 95% confidence intervals. No errors are reported for fits with zero degrees of freedom.

Feature [Number of Data Points]	QS Model	Parameters			
		ϵ_r	θ_RMS	A	n^*
Empty Lake Class [110]	Gaussian†	2.74 ± 0.30	$12.88 \pm 1.60°$	0.55 ± 0.07	1.22
	Hagfors	5.36 ± 1.58	$12.56 \pm 2.58°$	0.41 ± 0.12	1.22
Partially Filled Lake Class [101]	Gaussian†	2.09 ± 0.16	$15.84 \pm 2.00°$	0.11 ± 0.02	1.22
	Hagfors	3.49 ± 1.00	$15.52 \pm 4.52°$	0.06 ± 0.04	1.22
Background. Regions [211]	Gaussian	1.78 ± 0.20	$9.01 \pm 4.01°$	0.38 ± 0.03	1.22
	Hagfors†	2.26 ± 0.20	$6.18 \pm 4.01°$	0.34 ± 0.04	1.22
Empty $\#155$ [3]	Gaussian†	3.20	16.10°	0.44	1.22
	Hagfors	10.01	5.13°	0.36	1.22
Partially Filled $\#64$ [4]	Gaussian†	1.78 ± 0.26	$8.74 \pm 2.90°$	0.17 ± 0.10	1.22
	Hagfors	2.18 ± 0.05	$6.70 \pm 0.44°$	0.14 ± 0.01	1.22
Region 1 Empty	Gaussian	2.74*	9.80°	0.38	1.22

continued on next page

continued from previous page

Feature [Number of Data Points]	QS Model	Parameters			
		ϵ_{r}	θ_{RMS}	A	n^*
[2]	Hagfors	2.74^*	$9.20°$	0.38	1.22
Region 1 Background [2]	Gaussian	1.78^*	$14.40°$	0.30	1.22
	Hagfors	2.26^*	$9.50°$	0.28	1.22
Region 2 Empty [2]	Gaussian	2.74^*	$12.0°$	0.44	1.22
	Hagfors	2.74^*	$10.9°$	0.45	1.22
Region 2 Background [2]	Gaussian	1.78^*	$18.2°$	0.38	1.22
	Hagfors	2.26^*	$12.6°$	0.38	1.22
Empty Lakes $\#34 - \#36$ [3]	Gaussian†	4.43	$18.8°$	0.27	1.22
	Hagfors	N/A	N/A	N/A	N/A
Partially Filled Lake $\#100$ [3]	Gaussian†	2.69^*	$20.76°$	0.084	1.22
	Hagfors	6.19	$19.24°$	-0.04	1.22

4.3 Observations of Change

4.3.1 South Polar Region

SAR images of Titan's south polar region were acquired during 10 flybys dating between September 2005 and January 2010 (Table 4.2). Overlapping coverage is predominantly between two northwest-southeast trending swaths (T36 and T39) and five more recent southwest-northeast trending swaths (T55-T59). Also significant is a west-northwest to east-southeast swath (T49, Figure 4.3). The largest baseline for observing potential change among these observations is $\sim$2 yrs. Additional radar swaths of the South Polar region will be obtained during Cassini's Solstice Mission in July 2010 (T71), October 2013 (T95), February 2014 (T98), and July 2016 (T120).

For the majority of overlapping coverage, changes in appearance can be readily explained by variations in observational geometry. Morphologic features including bright hummocky terrain associated with topographic highs [Lopes et al., 2010], dendritic channel networks, and lacustrine features near the pole (70°S-90°S), appear unchanged (Figure 4.3). Persistent lacustrine features include filled lakes in the vicinity of the pole and dark areas, morphologically similar to terrestrial mud flats [Lopes et al., 2010], found near (150°E,80°S) and (0°E,75°S). Limited topography from SAR-Topo measurements [Stiles et al., 2009, Zebker et al., 2009] suggests these features are located in the lowest elevations of the south polar region (Figure 4.3). When referenced to estimates of Titan's geoid [Iess et al., 2010], these areas have comparable elevations to north polar mare shorelines reported in Kirk et al. [submitted].

Unambiguous changes in radar reflectivity are observed within three regions on the surface: (60°S, 150°E) and (70°S, 260°E), where ephemeral lacustrine features are observed, and Ontario Lacus, a large lake centered at (72°S, 175°E). In the first two regions, partially filled lake features are observed to transition over time into features morphologically consistent with empty lake basins. Some partially filled features remain radar-dark relative to their surroundings, but show an increase in backscatter that cannot be explained by incidence angle variations using common scattering models. Ontario Lacus shows evidence for shoreline recession between initial ISS observations in July 2004 / June 2005 [Turtle et al.,

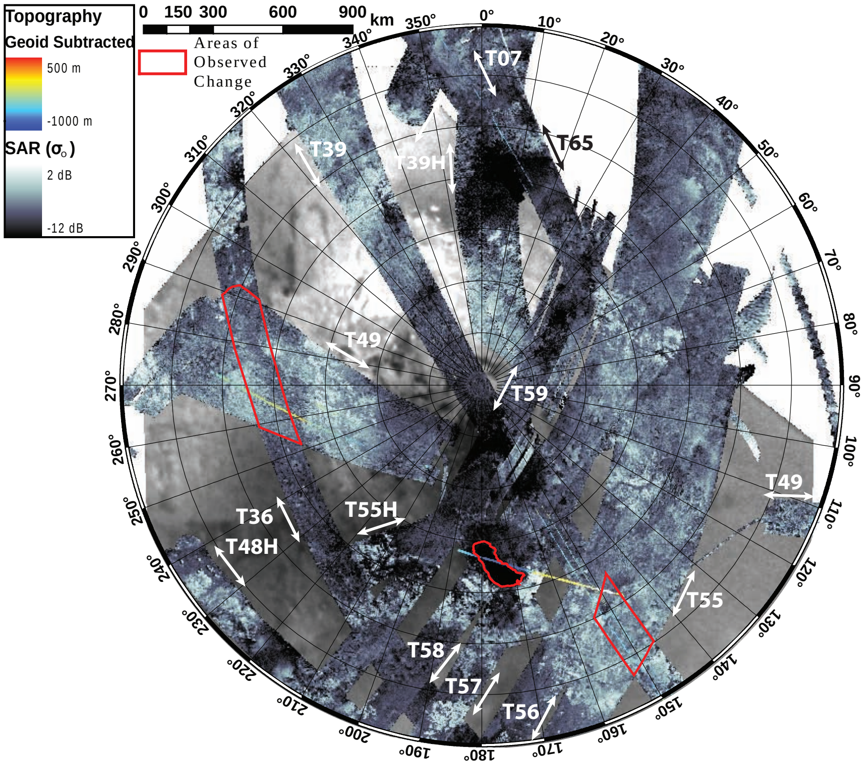

Figure 4.3: SAR mosaic of Titan's south polar region ($90°\mathrm{S} - 55°\mathrm{S}$) for Sep. 2005 through January 2010 (TA-T65). SAR data has been noise subtracted and corrected for bulk incidence angle effects. The June 2005 (Rev09) ISS observation is used as a background. The three areas which include ephemeral features are outlined in red. Geoid-subtracted topography is overlayed using the depicted colormap.

2009a] and recent SAR images obtained in July 2009 [Wall et al., 2010]. In addition to these observations, the appearance of dark features, interpreted as standing bodies of liquid hydrocarbon, has been previously documented by Cassini's Imaging Science Subsystem (ISS) at Arrakis Planitia between July 2004 and June 2005 [Turtle et al., 2009a, 2011].

4.3.1.1 Ephemeral Lacustrine Features

Ephemeral lacustrine features with areas of $\sim 100\ \mathrm{km}^2$ were observed in two portions of Titan's south polar terrain. SAR images of Region 1 (63°S-58°S, 144°E-153°E) were obtained in December 2007 (T39) and May 2009 (T55) (Figure 4.4ABC). In general, the T39

Table 4.2: South polar SAR swaths acquired between September 2005 and January 2010. H denotes HiSAR (low resolution SAR acquired outside 25 minutes from closest approach). ISS observations of the south polar region acquired between July 2004 and March 2009 are also included.

Swath	Acquisition Date	L_s	Overlapping Observations
T07	Sep. 7, 2005	309°	T36H
T36	Oct. 2, 2007	337°	T49,T55-T59
T39	Dec. 20, 2007	339°	T55-T59
T49	Dec. 21, 2008	352°	T36
T55	May 21, 2009	357°	T36,T39,T56
T56	June 6, 2009	358°	T36,T39,T55
T57	June 22, 2009	358°	T36,T39,T58
T58	July 8, 2009	359°	T36,T39,T57
T59	July 24, 2009	359°	T36,T39,T55H
T65	January 12, 2010	5.5°	T07,T39,T57-T59
Rev0A (ISS)	July 3, 2004	293°	T7-T59
Rev09 (ISS)	June 6, 2005	306°	T7-T59
T51 (ISS)	March 27, 2009	355°	T7-T59

SAR image shows lower σ_o values than T55, likely associated with the higher incidence angle for this pass. A collection of features which have morphologies consistent with hydrologic origin, however, have a significantly lower σ_o as compared to their surroundings. In the area of interest, the incidence angles for T39 and T55 are $\sim$37° (32°-41°) and $\sim$14° (11°-18°), respectively. The look direction azimuths vary by 160°, and the electric field vector of the incident wave was within 20° of horizontal polarization. The ratio between the backscatter cross-section of ephemeral features in T55 vs. T39 is 6-10, while the ratios for most other features in the image are 1.5-4 (Figure 4.4C). A purely diffuse cosine scattering law would produce a ratio of 1.26 for a cosine power of 1.22 [Wye et al., 2007], suggesting that there is a strong non-diffusive component in σ_o for the observed areas, which is consistent with observations of other surfaces on Titan [Wye et al., 2008]. Table 4.3 lists the average σ_o and incidence, azimuth, and polarization angles within the outlined features (Figure 4.4AB). The three dark features in T39 (outlined in cyan in Figure 4.4A) are nested within empty lake features (outlined in red) and have morphologic borders with similar complexity to partially filled lakes. In T55 (Figure 4.4B) the boundary between the previously dark features and the surrounding empty lake basins has disappeared, supporting the case that temporal surface change has taken place. Moreover, this argues that the change is such that the lake interior transitioned to resemble the surrounding terrain, as would be expected if the lake drained or evaporated. Other areas in the study region are dark in both observations, but show similar variation in backscatter between passes. These features are consistent with partially filled lakes whose liquid levels have changed (Section 4.3.1.2).

Region 2, located further south from the T39/T55 overlap area (72°S-63°S, 252°E-290°E), also shows large backscatter variations in lacustrine features (Figure 4.4DEF). This area was first imaged in early October 2007 (T36) and then in late December 2008 (T49), providing a 1.25 yr baseline. The differences in look direction azimuth and polarization angle are 60° and 25°, respectively. The backscatter and observational geometry of this study region is similar to the T39/T55 observations. Incidence angles for T36 and T49 are $\sim$35° (30°-40°) and $\sim$13° (10°-24°), respectively, and the ratios of backscatter cross-sections of the background and ephemeral features in T36 vs. T49 range from 1.5-4 and 6-11 (Figure 4.4F). The area of change is limited to the western section of the overlap area between 252°E and 270°E. The brightening of empty lake features in the eastern half of the overlap region is indistinguishable from the brightening of the background, since both are explained by incidence angle variations. The absolute σ_o values for bright features in the eastern half of the overlap region are higher than their western counterparts in T36, but similar in T49, consistent with the presence of an attenuating liquid layer in the western

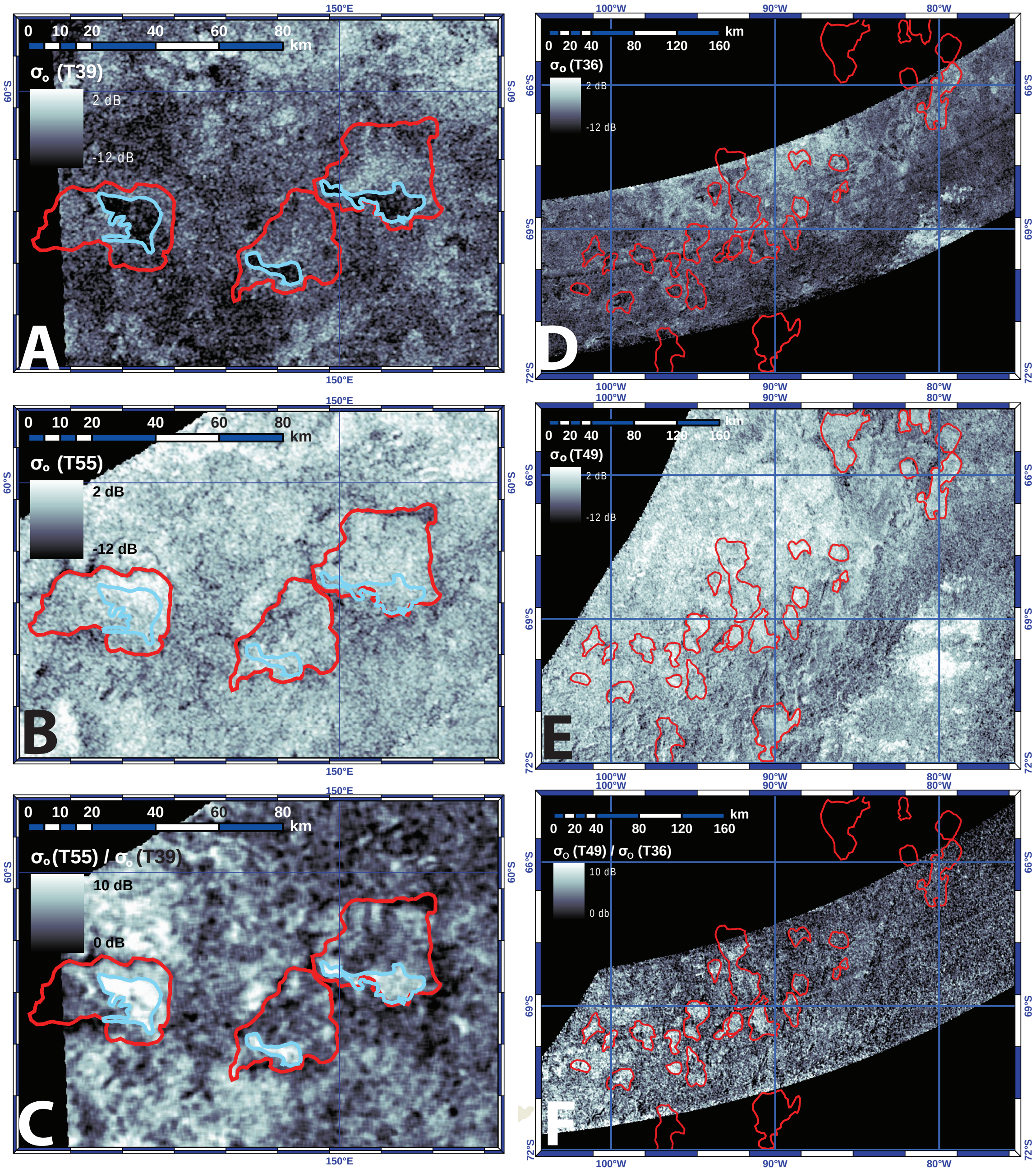

Figure 4.4: Ephemeral Observations. The left-hand column shows images of Region 1 while the right-hand column shows images of Region 2 (Section 4.3.1); A: T39; B: T55; C: σ_o ratio of T55/T39; D: T36; E: T49; F: σ_o ratio of T49/T36; SAR images are displayed from -12 to 2 dB. Ratio images are displayed from 0 to 10 dB. Lacustrine features are outlined in red. Partially filled lakes in T39 are outlined in cyan. Full resolution versions of these images are available in the supplementary online material to Hayes et al. [2011].

T36 features that was not present in the T49 observations. The variations in incidence angle between the western and eastern lake features within T36 is less than $4°$, too small to account for the σ_o differences if backscatter from these features is similar to empty or partially filled lake basins observed in other areas of Titan (Section 4.2).

The quasi-specular plus diffuse model presented in Section 4.2 for classes of empty and partially filled lakes can not be used to describe the backscatter variations in the ephemeral features located in Regions 1 and 2 without modifying the model coefficients between observations. In the absence of surface change, incidence angle variation would produce a backscatter ratio of $\sim$1.3 between observations, assuming a diffuse scattering law with a cosine power of $n = 1.22$. While the quasi-specular component preferentially increases backscatter at low incidence angles, the combined model cannot reproduce the ratio of $\geq$6 observed for the ephemeral features without increasing the amplitude of the diffusive component of later observations. The required increase would need to be roughly a factor of 3 for the mean of the return from the dark features, and a factor of 10 for the lowest backscatter values found within the features. The quasi-specular plus diffuse model can, however, be used to explain the non-ephemeral and background backscatter using parameters similar to those for the empty and partially filled lake classes (Figure 4.5).

The initial σ_o values for the ephemeral features in both areas of change (T36 and T39) fall within the class of partially filled lakes. Later observations of some ephemeral features (T55 and T49), along with the non-ephemeral features, fall within the class of empty lakes. Other ephemeral features, which have similar relative backscatter variation between observations, remain dark relative to their surroundings. This is consistent with these features re-

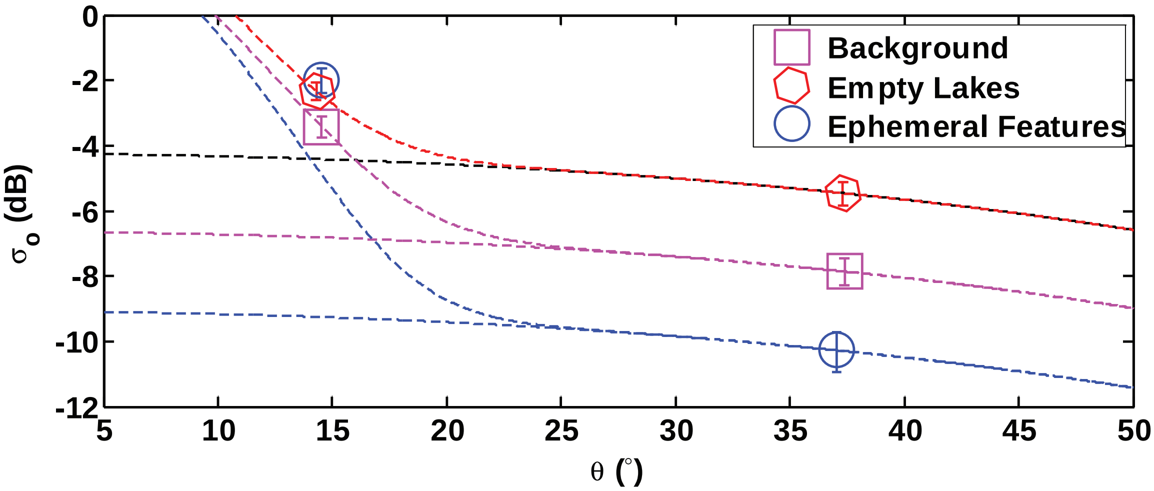

Figure 4.5: Backscatter (σ_o) values for the ephemeral features in Region 1 (T39/T55). Dashed curves depict the best-fit diffuse and quasi-specular plus diffuse scattering models for the ephemeral features, empty lakes, and background in Region 1 (T39/T55). Fit parameters and model definitions are listed in Table 4.1.

maining partially filled, although with a lower liquid level. Some backscatter models, such as a small perturbation model [Rice, 1951] for Bragg wave backscatter using the empirical Pierson-Moskowitz wave power spectrum [Pierson and Moskowitz, 1964], can match the backscatter curves for some of the ephemeral features. These models, however, require significant surface roughness on the liquid and would present backscatter functions which cross between the empty and partially filled lake classes. None of the features observed on Titan have such scattering properties, including lakes observed at multiple incidence angles (Figure 4.2).

Several arguments oppose simple surface scattering as the cause for ephemeral feature backscatter. Scattering models which fit the ephemeral features forbid a significant diffuse component and would require a highly variable surface environment over short length scales as, in each region, transitions are observed from partially filled to both partially filled and empty lake classes. In addition, surface waves on the lake do not naturally explain transient morphologic boundaries and are inconsistent with backscatter variations of other filled or partially filled lakes observed at multiple incidence angles. While the wave power spectrum and wave-wind interaction properties of liquid hydrocarbon on Titan are not well understood, the root-mean-square (RMS) wave height required to reproduce the ephemeral backscatter variations is $\sim$9 mm using parameters defined in Pierson and Moskowitz [1964], larger than the 3 mm RMS height limitation imposed on Ontario Lacus roughness by recent radar data [Wye et al., 2009]. Atmospheric scaling arguments suggest that the threshold wind speed required to produce capillary waves in liquid hydrocarbon is $\sim$0.5-1 m/s [Lorenz et al., 2010b]. For the planetocentric solar longitude (L_s) range of ephemeral feature observations ($337° \leq L_s \leq 359°$), global circulation model (GCM) estimations of wind speed remain below this threshold [Lorenz et al., 2010b]. In addition, average σ_o decreases with lake size [Paillou et al., 2008b], consistent with a rough lakebed contributing to backscatter in an environment where larger lakes are deeper. If backscatter from surface waves were primarily responsible for lake σ_o, larger lakes with greater fetch would produce bigger waves and greater off-nadir backscatter [Lorenz et al., 2010b].

The Cassini RADAR is linearly polarized and the electric field vector is oriented approximately parallel to Titan's surface during SAR operation. Deviations from horizontal polarization are less than 40° for the areas studied, and polarization effects are not expected to produce significant changes in observed backscatter. In quasi-specular facet scattering, where contributing surface elements are assumed to be oriented perpendicular to the illumination direction, and coherent diffuse scattering polarization effects are negligible. In non-coherent diffuse backscatter, polarization is randomized. For multiple scattering and wavelength-scale rough surfaces, where polarization effects can be important, the maximum potential change in reflected energy between observations from polarization effects alone is 16% for Region 1 and 45% for Region 2. These maxima, which are far less than the observed tenfold change in backscatter, occur when there is no return for parallel polarization, such as would be the case for a corner reflector oriented at the Brewster angle. Empirically, there are no obvious correlations between polarization angle and backscatter cross-section in SAR images of Titan's polar regions.

Observed σ_o values for the empty lake features in Regions 1 and 2 are consistent with the σ_o values for all empty lakes observed to date. The σ_o values for ephemeral features in Regions 1 and 2 are initially consistent with partially filled lake backscatter and a year later consistent with empty lake returns. Ephemeral features are inconsistent with the presented model using constant coefficients. Explaining them using incidence angle variations requires backscatter behavior not observed on Titan. Polarization and azimuth angle effects alone cannot explain the differences. Coupling these radiometric arguments to the transient borders between the ephemeral observations supports the conclusion that temporal change has taken place. The most probable candidate for this surface change is a reduction in the liquid level of partially filled lakes. In the next section, a two-layer model is developed to estimate the liquid level reduction required to explain observed backscatter variations.

Table 4.3: Ephemeral feature $\langle\sigma_o\rangle$ values and observational geometries. Ephemeral features refer to partially filled to empty lake transitions while partially filled features correspond to changes in lake depth without complete drying. Incidence angles are measured from the local surface normal. Azimuth angles are measured counterclockwise positive from east. Polarization angles represent the angle between the electric field vector and the plane of incidence, measured counterclockwise positive from perpendicular (horizontal polarization) when looking down the wave vector. Error bars in $\langle\sigma_o\rangle$ represent 95% confidence intervals (CI) obtained using a boot-strap Monte Carlo technique as described in Press et al. [1992]

Swaths		Feature	Incidence Angle		Azimuth Angle		Polarization Angle		$\langle\sigma_o\rangle$ (dB)	
T39	T55	Background	36.8°	14.2°	165°	320°	195°	177°	-7.86 ± 0.44	-3.43 ± 0.34
T39	T55	Empty Lake	38.8°	14.4°	166°	328°	199°	170°	-5.46 ± 0.38	-2.33 ± 0.27
T39	T55	Ephemeral	37.4°	14.3°	166°	327°	197°	170°	-10.27 ± 0.66	-1.24 ± 0.34
T39	T55	Partially Filled	36.5°	18.6°	166°	327°	196°	175°	-13.00 ± 0.39	-5.70 ± 0.28
T36	T49	Background	33.0°	21.4°	316°	20°	159°	140°	-6.50 ± 0.41	-3.10 ± 0.24
T36	T49	Empty Lake	34.0°	17.3°	308°	10°	165°	140°	-4.60 ± 0.32	-2.20 ± 0.20
T36	T49	Ephemeral	35.7°	13.0°	293°	6°	166°	142°	-8.00 ± 0.67	-0.80 ± 0.45
T36	T49	Partially Filled	34.2°	13.2°	302°	8°	163°	142°	-12.0 ± 0.90	-5.10 ± 0.33

4.3.1.2 Two-Layer Model

In order to understand the ephemeral lake features observed in the south polar region, we use a simple two-layer model to estimate the ratio between partially filled ($\sigma_{o,\text{ fil}}$) and empty ($\sigma_{o,\text{ emp}}$) lake backscatter, deriving a lower limit on liquid depth changes from radar-returns:

$$\sigma_{o,\text{ fil}} = T_{\perp}(\theta)T_{\perp}(\theta_{\text{liq}})A^2(\theta_{\text{liq}}, \Delta d)\frac{\sigma_{o,\text{ bed}}(\theta_{\text{liq}}, n_{\text{liq}})}{\sigma_{o,\text{ bed}}(\theta_{\text{atm}}, n_{\text{atm}})}\sigma_{o,\text{ emp}} \tag{4.4}$$

where $T_{\perp}(\theta)$ is the Fresnel transmission coefficient for perpendicular polarization, $A(\theta_{\text{liq}}, \Delta d)$ is the attenuation coefficient, $\sigma_{o,\text{ bed}}(\theta_{\text{liq}}, n_{\text{liq}})$ is the interaction with the lake floor in the liquid medium, and $\sigma_{o,\text{ bed}}(\theta_{\text{atm}}, n_{\text{atm}})$ is the empirical backscatter function for exposed lakebeds. This model consists of three main components (Figure 4.6): signal interaction with the liquid surface, attenuation through the liquid layer, and interaction with the lake bottom. For the purposes of this work, the liquid surface was assumed to be smooth at the radar wavelength, allowing wave transmission to be determined by the Fresnel transmission for an interface between atmosphere ($n_{\text{atm}} \sim 1$) and liquid hydrocarbon ($n_{\text{liq}} \sim 1.3$). The real part of the index of refraction for liquid hydrocarbon was derived from the dielectric constant measurement of $\epsilon_{\text{r}} = 1.75$ performed by Paillou et al. [2008b] using liquid natural gas (LNG). Any additional backscatter from the liquid surface would tend to decrease the percentage of transmitted radiation and increase the calculated depth change. One-way attenuation is calculated using the attenuation coefficient for a complex medium:

$$A(\theta_{\text{liq}}) = e^{-4\pi\kappa\Delta d \sec\theta_{\text{liq}} \,/\, \lambda} \tag{4.5}$$

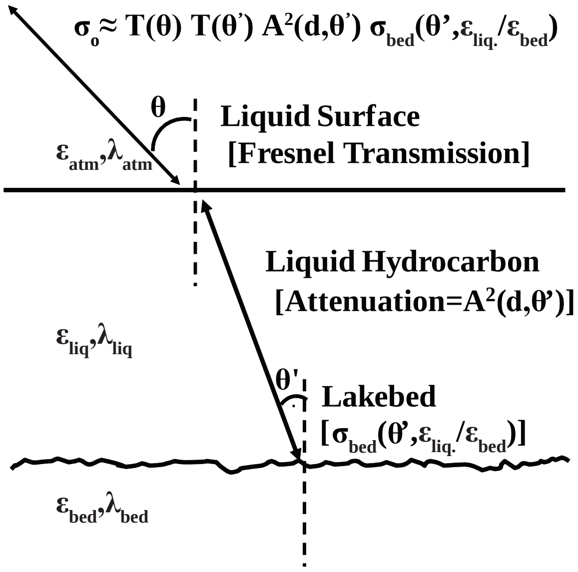

Figure 4.6: Schematic of two-layer model.

where θ_{liq} is the incidence angle within the liquid medium from Snell's law, λ is the free-space SAR wavelength, κ is the imaginary component of the complex index of refraction, and Δd is the change in depth of the liquid layer.

The difference in lakebed backscatter between filled and empty states results from a brightening associated with the decreased incidence angle (θ_{liq} vs. θ_{atm}) at the liquid interface, and a potential darkening from decreased dielectric contrast ($\epsilon_{\mathrm{liq}}/\epsilon_{\mathrm{bed}}$ vs. $\epsilon_{\mathrm{atm}}/\epsilon_{\mathrm{bed}}$) at the lakebed interface. The importance of the decreased dielectric contrast can vary. For a diffusely scattering lakebed with a saturated subsurface the effect would be small. For a completely dry lakebed, however, the effect can be large. In the case of an impermeable lakebed surface, the backscatter decrease would approximate the ratio of the normal-incidence Fresnel reflection coefficients for quasi-specular facet scattering. For surface dielectric constants varying between water-ice (ϵ_{r} =3.16) and tholin (ϵ_{r} =2.0-2.4), the reduction in the reflection coefficient is between a factor of 3 and 10. For the case of a permeable lakebed, the effect of the decreased dielectric contrast is difficult to model because of the unknown nature of Titan's regolith structure. In the simplest model for a diffusely scattering lakebed, Mie theory can be used to approximate an ensemble of irregular scatterers which are on the order of, or smaller than, the wavelength [Black et al., 2001, Pollack and Cuzzi, 1980]. For this scenario, backscatter reductions are similar in magnitude to those modeled by the Fresnel reflection coefficient. However Mie theory, which usually refers to non-interacting separable particles, has limited use when applied to dense aggregates such as planetary regoliths. The effect we are discussing, namely a change in radar reflectivity between saturated vs. unsaturated regolith, is a well known terrestrial phenomenon. For liquid water on Earth, which has an index of refraction of $(76 - 2.3i)$ at a wavelength of 2.2 cm and ambient conditions [Barthel and Buchner, 1991], soil moisture can increase (as opposed to decrease, as would occur on Titan) σ_o by a factor of $\sim$5 for volumetric water content of 0.6 $\mathrm{g/cm^3}$ [Dobson et al., 1985]. When calculating liquid depth variations using the two-layer model, we neglect the decreased dielectric contrast and provide a constraint on the maximum liquid depth. However, as shown below, there is evidence that the measurements of relative liquid depth are robust with respect to this effect.

If permeable, the pore space below a filled lake will contain liquid hydrocarbon, saturating the regolith [Hayes et al., 2008a]. This saturated medium can take decades to centuries to radially flow away from the lake (Section 4.4). If the liquid in the lake is removed, evaporation from the saturated regolith will proceed more slowly than for the exposed lake, limited by the diffusivity and permeability of the porous medium [Saravanapavan, 2000]. It is therefore possible for the regolith below an empty lakebed to remain saturated for some time after the lake itself has evaporated. In this case the subsurface scattering component of the radar return will not be strongly affected by decreased dielectric contrast at the lakebed interface. The lack of a significant increase in σ_o just outside of the near-shore region of Ontario Lacus (Section 4.3.1.2), where a shallow regional slope provides a gradual transition between saturated and potentially unsaturated regolith, is consistent with this hypothesis.

As discussed above, Figure 4.2 shows the backscatter variation for an empty and a partially filled lake observed at multiple incidence angles. Both features were located in the north polar region and observed during northern winter, when minimal evaporation and precipitation are expected [Mitchell, 2008, Newman et al., 2008, Newmann and Richardson, 2009, Graves et al., submitted]. Backscatter models for the σ_o variations in these two observations show that the partially filled lake has a more pronounced dependence on low-angle incidence as compared to empty lake backscatter, consistent with the increased incidence angle within the liquid medium. The overall lower σ_o values are consistent with attenuation through a liquid layer. The collective set of empty and filled lake σ_o values (Figure 4.1) also shows steeper incidence dependence for the partially filled lakes at low angles. Arguably, the inflection point between quasi-specular and diffuse scattering exists at $\sim 20^\circ$ in the empty lake class and $\sim 30^\circ$ in the partially filled lake class (Figure 4.1). If these inflection points indeed both represent the transition between quasi-specular and diffuse backscatter at the lakebed interface, then that suggests an incidence angle shift due to Snell's Law for an overlying medium with a real dielectric constant of ~ 2, consistent with liquid hydrocarbon.

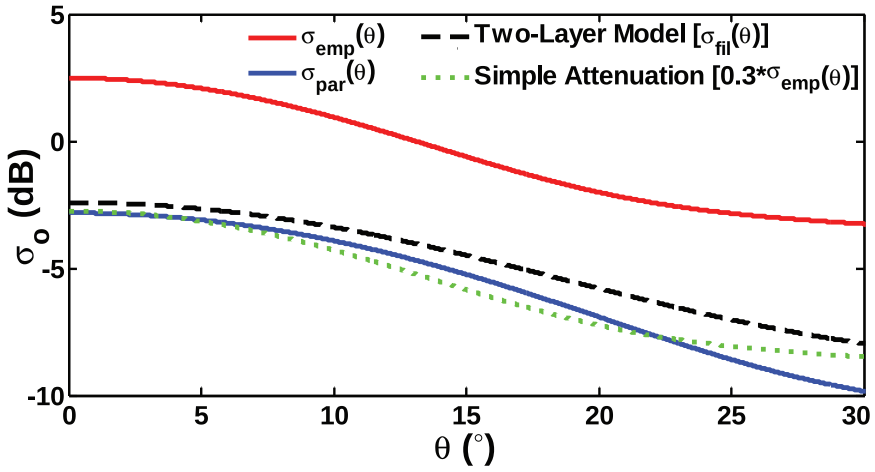

Figure 4.7: Best-fit backscatter models for empty (red) and partially filled (blue) lake classes. The black dashed line represents the empty lake backscatter modified by the two-layer model (Equation 4.4) and the green dotted line is the empty lake backscatter multiplied by a constant attenuation factor.

The best-fit model for the partially filled lake class is similar to the best-fit model for the empty lake class modified by the assumptions of the two-layer model presented above (Figure 4.7). After evaluating the empty lake backscatter at θ_{liq} and multiplying by the transmission and attenuation (Equation 4.5) coefficients, using a best-fit depth of 1.2 m, the shape and magnitude of the resulting backscatter is very similar to the partially filled lake class. We did not account for the effect of decreased dielectric contrast at the lakebed interface, but it is indistinguishable from liquid attenuation in this model. Simply multiplying the empty lake backscatter by a constant attenuation factor also produces a similar result, although it does not match the shape of the profile as well at low incidence angles (Figure 4.7). Overall, the backscatter functions observed for both single features and the collective set of empty and partially filled lakes is consistent with the presented two-layer model.

Changes in lake depth can be calculated from the backscatter ratio of subsequent observations using Equation 4.4 for partially filled to empty lake transitions and Equation 4.5 for lakes which remain partially filled, as a liquid layer is present in both observations. In both cases, the calculated liquid depth is inversely proportional to the complex index of refraction or loss tangent of the liquid. Ignoring the possible affects of the decreased dielectric contrast, we calculate $\sigma_{o,\text{ bed}}(\theta_{\text{liq}}, n_{\text{liq}})/\sigma_{\text{bed}}(\theta, n_{\text{atm}})$ using best-fit Gaussian scattering model through the observed empty-lake backscatter. Typical values for $30^\circ < \theta < 40^\circ$, where the ephemeral lakes are observed, are $\sim$1.2 and do not vary significantly. The brightening effect is more apparent for lower incidence angles, where $\sigma_{o,\text{ bed}}(\theta_{\text{liq}})/\sigma_{\text{bed}}(\theta_{\text{atm}})$ can grow up to a factor of 3 for a realistic parameter space. However, the observational geometry of ephemeral features is such that the earlier observations (T36 and T39) were acquired at larger incidence, where the brightening effect is less significant. For incidence angles less than 40°, $T(\theta)$ varies from 98$\%$ to 100$\%$ for parallel polarization and 96$\%$ to 98$\%$ for perpendicular polarization. Thus, reflection loss at the atmosphere/liquid interface is minimal. In the model, the dominant term, by roughly an order of magnitude, is the observed value $\sigma_{o,\text{ fil}}/\sigma_{o,\text{ emp}}$.

Using the average σ_o values listed in Table 4.3 and a loss tangent of $\tan\Delta = (9.2^{+2.5}_{-2.0}) \times 10^{-4}$ [Hayes et al., 2010, Paillou et al., 2008a] Equations 4.4 and 4.5 yield depths of $0.7 - 1.0$ m for ephemeral lake depths in the T39/T55 and T36/T49 overlap areas. These values are consistent for both partially filled to partially filled and partially filled to empty lake transitions. The effect of a decreased dielectric contrast at the lakebed interface could decrease estimated depth changes, but Ontario Lacus and other potentially shallow liquid basins do not show the significant increase in σ_o just outside the lake that would be expected

Table 4.4: Two-layer model loss rate results for ephemeral lake features. Modeled Depth Change and Flux Rates are proportional to $(9.2 \times 10^{(-4)})/\tan\Delta$.

Swaths		Transition	Modeled Depth Change	Flux
T39	T55	Partially Filled to Empty	1.00 ± 0.33 m	0.71 ± 0.23 m/yr
T39	T55	Partially Filled to Partially Filled	0.98 ± 0.26 m	0.69 ± 0.19 m/yr
T36	T49	Partially Filled to Empty	0.74 ± 0.30 m	0.61 ± 0.24 m/yr
T36	T49	Partially Filled to Partially Filled	0.78 ± 0.38 m	0.64 ± 0.31 m/yr

in this scenario. Additionally, consistency between partially filled to partially filled and partially filled to empty lakes transitions would not be expected if the affect of the decreased dielectric contrast were significant. We list model results for each ephemeral lake region and transition type in Table 4.4. As we will see in the following section, model results agree with the estimated reduction in the depth of Ontario Lacus from shoreline recession measurements.

4.3.1.3 Ontario Lacus [72°S, 175°E]

Ontario Lacus, with a surface area of 15,600 km^2 as of July 2009, is the largest lacustrine feature in the south polar region. It is interpreted as a liquid hydrocarbon lake and was originally observed by ISS in July 2004 and June 2005 [Turtle et al., 2009a]. Subsequent observations by the Visual and Infrared Mapping Spectrometer (VIMS) in December 2007 demonstrated liquid ethane was present in the lake [Brown et al., 2008]. Additional analysis of VIMS data led to the identification of annuli surrounding the feature that Barnes et al. [2009] interpreted as past shorelines. Recent RADAR data of Ontario Lacus have been acquired in the form of altimetry measurements in December 2008 (T49) and SAR images in June 2009 (T57), July 2009 (T58), and January 2010 (T65) [Wall et al., 2010]. The altimetry measurements show that the lake surface was smooth and specular during the

T49 flyby, with a RMS height variation of less than 3 mm over the 100 m Fresnel zone of the radar footprints [Wye et al., 2009]. SAR imagery shows Ontario Lacus as a complex feature with multiple inlets, shoreline features, and contributing channel networks [Wall et al., 2010]. Lorenz et al. [2010a] discuss morphologic similarities between Ontario and the transient lake at Racetrack Playa, Death Valley National Park, CA USA.

Comparison between the June 2005 ISS and July 2009 SAR data shows a difference in the shorelines of Ontario (Figure 4.8). While the northern borders match within the $\sim$1 km resolution of the ISS data [Turtle et al., 2009a], the southern borders show up to a 20 km recession of the shoreline between ISS and RADAR images. While registration accuracy (2 km RMS) between the datasets is sufficient to support the interpretation of temporal surface change additional ISS data, obtained in March 2009 (T51) at a resolution of $\sim$5 km, confirm the observed shoreline recession at the southernmost end of the lake [Turtle et al., 2011]. Furthermore, the 2009 ISS shoreline matches the 2009 SAR shoreline to within the expected registration error [Turtle et al., 2011]. Lastly, the 2005 ISS border roughly correlates with a narrow bright rim observed in the SAR data (Figure 4.8) [Wall et al., 2010]. This rim is consistent with a previous shoreline and approximately coincides with the annuli observed by Barnes et al. [2009] using VIMS images acquired in the 5 μm band.

Although cross-instrument comparisons can be awkward, there are several lines of evidence that support the interpretation of shoreline recession at Ontario Lacus. First, as stated above, the shorelines at the northern-most end of the lake match to within the limits of ISS resolution, while there is a $\sim$10 km recession in the southwest corner. Second, altimetry

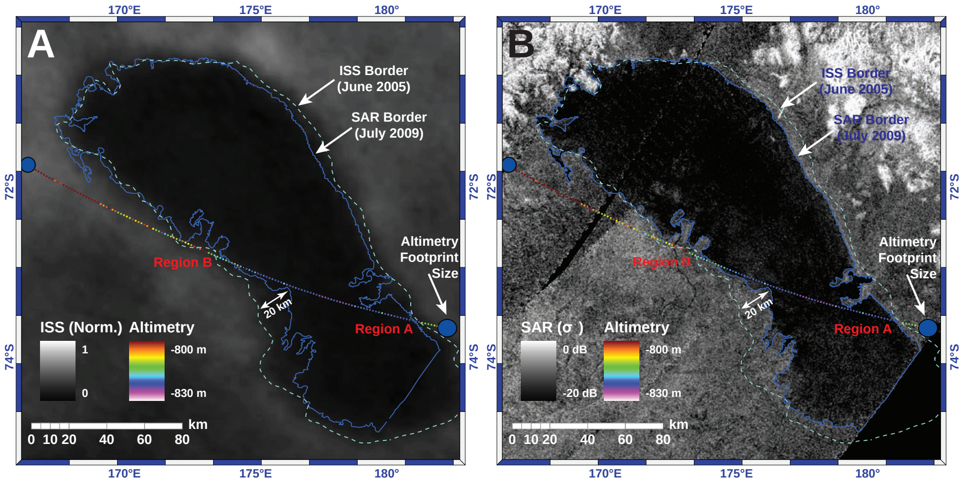

Figure 4.8: Equidistant cylindrical projection of Ontario Lacus. The lake border from the 2005 ISS image is shown in cyan, while the 2009 SAR border is blue. T49 altimery data is overlain. Heights are calculated from echo center-of-mass and referenced to Titan's geoid as presented in Iess et al. [2010]. Altimetry footprint size is shown using blue circles; A: ISS image obtained in June 2005 (Rev09). ISS shoreline is defined by following a constant contour of relative brightness referenced to local offshore pixel intensity; B: SAR image obtained in June and July 2009 (T57/T58).

measurements obtained in December 2008 (T49) show that there is a consistent slope for 100 km leading up to the southeast corner of the lake (Figure 4.9). At the resolution of the available data, there is no break in slope or bench in the topography that could support a vast expanse of mm-deep liquid which would be transparent to radar and opaque to ISS. Third, the two-way dispersion length, or *e*-folding attenuation depth, of the near-shore liquid in Ontario is ~ 1 m [Hayes et al., 2010, Paillou et al., 2008a], suggesting that cross-instrument comparison can, at most, account for $\sim 25\%$ of the observed four meter depth change in Ontario (see below). The average loss rate of ∼1 m/yr is also consistent with depth changes derived from backscatter modeling of nearby ephemeral lacustrine features. Lastly, there is no significant change in σ_o for pixels outside the 2005 ISS shoreline in the 2009 SAR image. If ISS observed a saturated mud flat around Ontario, one might expect it to be distinguishable from dry regolith based on the difference in dielectric contrast between saturated and unsaturated pore space (see previous section). Combined with the 2009 ISS observations of Ontario described in Turtle et al. [2011], these arguments make a compelling case in support of lateral shoreline regression over the observed period.

The average backscatter cross-section ($\langle\sigma_o\rangle$) within Ontario Lacus is approximately equal to the average noise equivalent backscatter ($\sigma_{o,\text{ ne}} = -20 \pm 1$ dB). However, the average backscatter in the southwest portion of the lake, where the largest shoreline recession is observed, is above this noise floor and yields $\langle\sigma_o\rangle = -14 \pm 2$ dB. At an incidence angle of 30° (geometry of T58 near Ontario), a normalized backscatter cross-section of -14 ± 2 dB is consistent with the backscatter from the class of partially filled lakes, suggesting that Ontario Lacus is shallow enough in this region for the RADAR to penetrate the liquid layer [Hayes et al., 2008a, 2010, Paillou et al., 2008a]. Around the entire lake, near-shore $\langle\sigma_o\rangle$ values are also consistent with partially filled lake backscatter and observed to exponentially decrease in the off-shore direction [Hayes et al., 2010]. In Hayes et al. [2010] we use the exponential decay of $\langle\sigma_o\rangle$ as a function of distance from the shoreline to derive relative near-shore bathymetry slopes in different regions around Ontario. When coupled to nadir-looking altimetry measurements obtained in December 2008, these relative slopes can be used to generate a near-shore bathymetry map and derive a value for the imaginary component of the liquid's complex index of refraction ($n + i\,\kappa$) of $\kappa = (6.1^{+1.7}_{-1.3}) \times 10^{-4}$. The relative differences in lake bathymetry derived in Hayes et al. [2010] correlate with the relative differences in shoreline recession observed between the 2004 and 2009 observations of Ontario, further supporting an interpretation of uniform reduction in lake depth

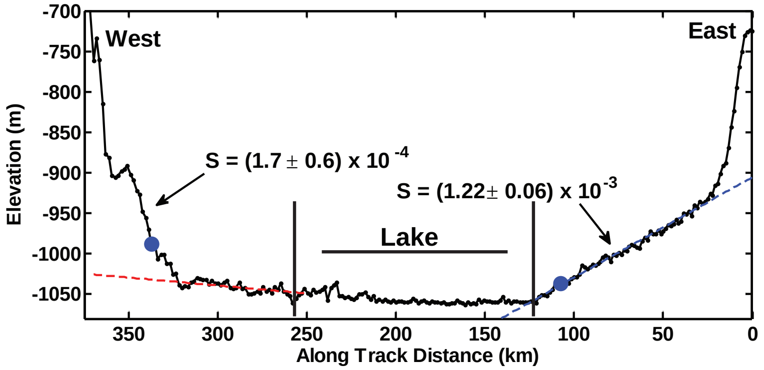

Figure 4.9: Analysis of December 2008 (T49) altimetry track. Blue circles correspond to positions marked in Figure 4.8. Values represent geoid subtracted altimetry using radar echo center of mass. Geoid values obtained from Iess et al. [2010]. Local slopes (S) near altimetry intersections with Ontario Lacus are shown in blue (Region A) and red (Region B). Local slopes are converted to topographic slopes (D) assuming the direction of steepest descent is toward the shoreline [Hayes et al., 2010]

(Figure 4.10).

The areal difference between the 2005 ISS and 2009 SAR borders of Ontario Lacus is $3200 \pm 200\ \mathrm{km}^2$. In region A (Figure 4.8) the average shoreline recession is 2.0 ± 0.2 km. Using a topographic slope $D_{\mathrm{A}} = (2 \pm 0.1) \times 10^{-3}$ (Hayes et al. [2010]), this recession distance corresponds to a vertical elevation of 4.0 ± 0.5 m. In region B, where $D_{\mathrm{B}} = (1 \pm 0.6) \times 10^{-3}$ (Hayes et al. [2010]) and shoreline recession is 3.8 ± 0.2 km, the resulting elevation change is 3.8 ± 2.6 m. Using the near-shore bathymetry map derived in Hayes et al. [2010], shoreline recession in all regions suggests an average depth change of 4.0 ± 1.3 m (Figure 4.10). This average value is consistent with the local results derived in regions A and B using direct altimetry measurements. When comparing recession magnitude to local near-shore slope, shoreline position is determined by examination of average backscatter vs. depth and selecting the region where the exponential decay transitions into

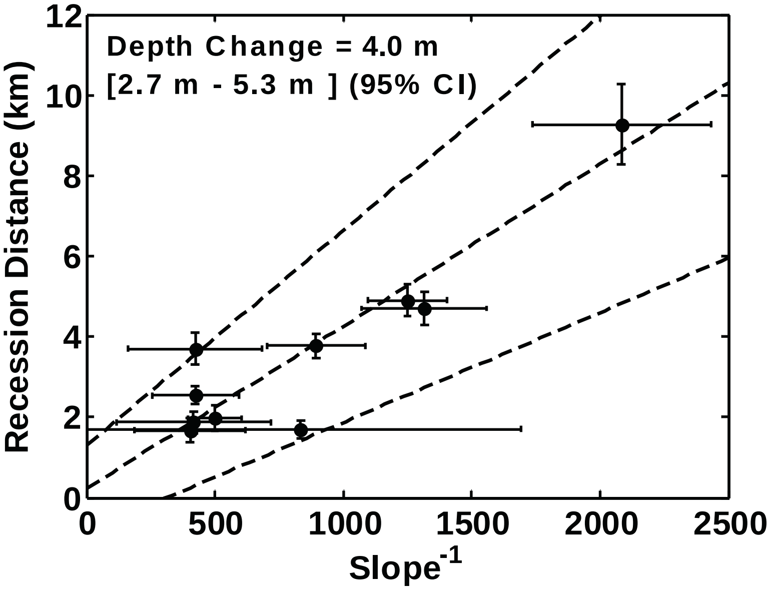

Figure 4.10: Scatter plot of recession distance vs. inverse bathymetry slope of Ontario Lacus. Bathymetry values were obtained in ten areas around the lake by fitting the exponential attenuation of nearshore backscatter. A detailed description of these calculations can be found in Hayes et al. [2010]. Errors represent 95% confidence intervals (CI) and the dashed lines are the best-fit and 95% CI for a linear fit.

shoreline backscatter. The slope of a plot of inverse near-shore bathymetry versus shoreline recession is the depth change, $\Delta d = 4.0 \pm 1.3$ m, and the offset, $d_{\text{off}} = 0.2 \pm 1.2$ m, is consistent with zero (Figure 4.10). To within errors, these three estimates are equivalent and suggest an average loss rate of 1.0 ± 0.3 m/yr during the 4 years between observations. Using an area of $18,700\ \mathrm{km}^2$ for Ontario in 2005, this loss rate corresponds to $19 \pm 6\ \mathrm{km}^3/\mathrm{yr}$ and $(7.9 \pm 2.6) \times 10^{12}\ \mathrm{kg/yr}$ assuming the removed material is liquid methane.

Changes in tidal acceleration from Saturn during Titan's 16-day orbital period may affect the shoreline of Ontario. To first order in $R_\mathrm{T}/a_\mathrm{T}$, where R_T is Titan's radius and a_T is its semimajor axis, the tangential tidal acceleration (f), assuming Titan acts as a rigid sphere, is [Lorenz, 1994]:

$$f = (3/2)GM_{\rm s}R_{\rm T}\left[a_{\rm T}\frac{(1-e_{\rm T}^2)}{(1+e_{\rm T}\cos\nu_{\rm TA})}\right]^{-3}\sin 2\phi \tag{4.6}$$

where G is the gravitational constant, $M_{\rm s}$ is the mass of Saturn, $e_{\rm T}$ is Titan's eccentricity, $\nu_{\rm TA}$ is Titan's true anomaly, and ϕ is the Titanocentric angle between the sub-Saturn point $(0°{\rm E}, 0°{\rm S})$ and Ontario Lacus $(175°{\rm E}, 72°{\rm S})$. The vertical deviation of the local equipotential surface is $d_{\rm tide} = R_{\rm lake}f/g_{\rm T}$ [Lorenz, 1994], where $g_{\rm T}$ is Titan's gravitational acceleration and $R_{\rm lake}$ is Ontario's north-south radius (∼125 km). Tidal forcing on Titan is slow enough that there is no resonant amplification of the tides [Lorenz, 1994]. For the 2005 ISS (Rev09) and 2009 Radar (T57/T58) observations Titan's true anomaly was $277°$ and $146°$, respectively. The corresponding vertical change in the extremes of the shoreline is ~ 0.4 m, smaller than the observed 4.0 ± 1.3 m depth change. This tidal amplitude is similar to that reported by Barnes et al. [2009]. In addition, shoreline recession measurements suggest a constant depth change around the lake while tidally induced changes would vary in magnitude with north-south distance from Ontario's center of mass. We therefore conclude that the tide is not a dominant contributor to the observed change.

The chemical composition of lakes on Titan is expected to be a mixture of ethane, methane, and propane, with trace amounts of higher-order hydrocarbons and nitriles [Cordier et al., 2009]. At 92 K, methane is greater than four orders of magnitude more volatile than ethane and propane, suggesting that available methane will evaporate prior to any significant ethane [Fairall et al., 1996, Mitri et al., 2007]. If evaporation is responsible for the depth change, the observed rate of 1.0 ± 0.3 m/yr favors a high methane fraction near the surface of the lake. Ethane would impede methane evaporation if the liquid were well mixed. If Ontario were solely composed of ethane/propane, the observed evaporation rate would require non-physical advection rates to move enough dry air over the lake surface to remove equivalent amounts of liquid.

4.3.2 North Polar Region

Titan's hydrocarbon lakes were first identified by Stofan et al. [2007a] using SAR data from the north polar region ($55°$N-$90°$N) acquired on July 22, 2006 (T16). Since T16, the north polar region has been imaged by 7 additional SAR passes (Figure 4.11) dating between September 2006 (T18) and December 2009 (T64). All but one of these observations were obtained over the course of a nine-month period between July 2006 and May 2007, presenting only a short baseline for change detection relative to Titan's 29.5 year seasonal cycle (Table 4.5). The latest observation of the north polar region (T64), acquired in December 2009, provides up to a 3.5 year baseline between overlapping passes. While there are differences in the appearance of lacustrine features imaged in both T64 and previous passes, initial analysis suggests that, to within observational errors, they can all be explained by variations in viewing geometry. Additional observations of the north polar region, which specifically target areas of expected change, are planned during Cassini's Solstice Mission in May 2012 (T83), September 2012 (T86), May 2013 (T91), July 2013 (T92), October 2013 (T95), August 2014 (T104), and February 2015 (T109).

The T64 SAR pass was acquired at an average incidence angle of $38°$ (95% of the distribution of incidence angles is between $24°$ and $51°$). For the primary areas of overlap

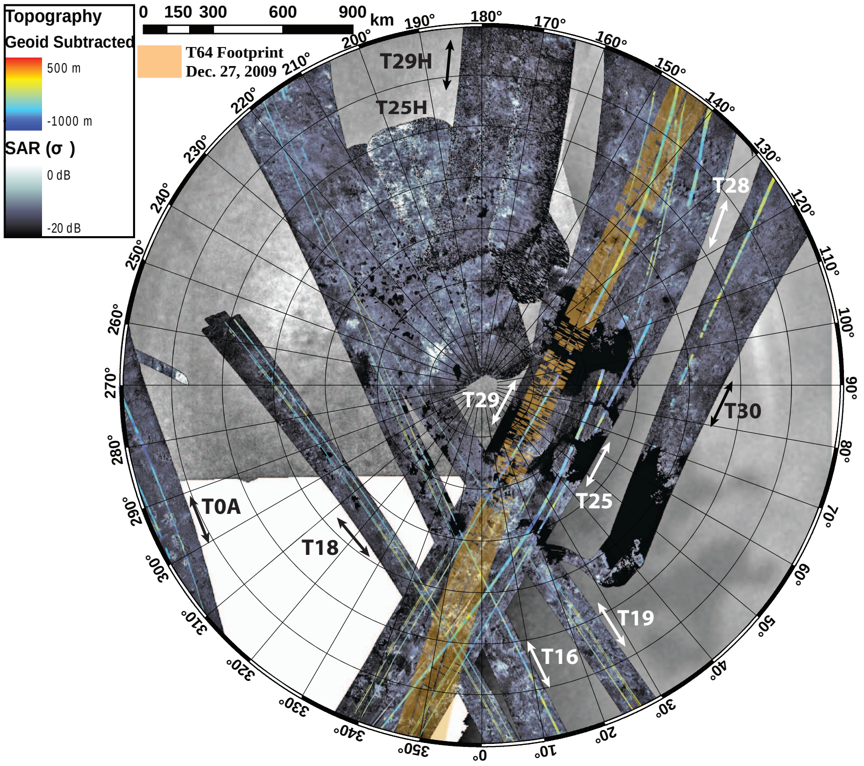

Figure 4.11: SAR mosaic of Titan's north polar region (55°S 90°S) for July 2006 through December 2009 (T16-T64). SAR data has been noise subtracted and corrected for bulk incidence angle effects. Beam positions for T64 repeat coverage is highlighted in orange. ISS observations 1984, 5696, and 6813 are used as a background.

Table 4.5: North polar SAR swaths between July 2006 and Dec. 2009. H denotes HiSAR (low resolution SAR acquired outside 25 minutes from closest approach). * All observations overlapping T30 are with altimetry data, repeat SAR coverage is currently not available for this pass.

Swath	Acquisition Date	L_s	Overlapping Observations
T16	July 22, 2006	321°	T19,T25,T28
T18	Sep. 23, 2006	323°	T25,T28
T19	Oct. 9, 2006	324°	T16,T25,T28,T25H,T28H
T25	Feb. 22, 2007	328°	T16,T19,T28,T64
T28	April 10, 2007	330°	T16,T19,T25,T64
T29	April 26, 2007	331°	T16,T18,T19,T25,T28,T64
T30*	May 12, 2007	331°	T16,T18,T19,T25,T28,T64
T64	Dec. 28, 2009	5°	T25, T28

with T25 and T28 (Figure 4.11), this corresponds to an average 19° ($8^\circ - 29^\circ$) and 14° ($4^\circ - 23^\circ$) higher incidence angle, respectively. As backscatter steeply decreases with increasing incidence in this range, detecting increases in liquid depth on top of backscatter reductions from geometrical variations between T25/T28 and T64 is difficult. As a consequence, backscatter from both empty and partially filled lakes which exist in the overlap area exhibit incidence angle behavior consistent with the models and lake classifications presented in Section 4.2 (Figure 4.12). To further complicate matters, heavy weather at the Deep Space Network station in Madrid, Spain, during downlink from the spacecraft resulted in partial data loss of T64. While these observations do not unambiguously identify change in lake depth in the north, they do strengthen our confidence in the detectability of change by confirming the incidence angle variation seen in the partially filled and empty classes discussed in Section 4.2. In addition, the morphologic boundaries of lake and mare shorelines remain unchanged between T64 and earlier observations (Figure 4.13). Repeat coverage of the north obtained using the ISS instrument also shows no unambiguous changes in lake distribution as of late 2009 [Turtle et al., 2011].

While the majority of overlapping coverage prior to T64 shows no obvious examples of surface change, there are two features that stand out as having significant backscatter and morphologic differences between passes that may represent temporal variations. In both cases, however, incidence angle variations and opposite side look directions complicate analysis. The first case is a small lake located in the overlap area between T16 and T19. This lake shows an increase of $6 - 7$ dB between incidence angles of 31° (T16) and 16° (T19), but it remains to be seen if this ratio significantly differs from that expected due to geometric effects which are similar in magnitude ($3.4 - 5.4$ dB). Mitchell et al. [in preparation] examine this feature in more detail. Additional partially filled lake features in the T16/T19 overlap area also show backscatter ratios ranging between 3 and 7 dB. Separating out potentially subtle variations due to surface change from incident and azimuth angle variations for these partially filled lakes will require more complex backscatter models than those presented in Section 4.2 and is the subject of future work.

The second area of significant variation is located in the northern shores of Kraken Mare (Figure 4.14). Between February (T25) and April (T28) 2007 this estuary-like morphologic feature, henceforth referred to as Kraken North, exhibits an average backscatter ratio of $\sigma_{o,\ T25}/\sigma_{o,\ T28} \sim 11\ dB$ (Figure 4.14; solid red arrow), with nearby sections of the same feature showing $\sim$ 2 dB of change (Figure 4.14; dashed blue arrows). The incidence angles in this region are $12^\circ \pm 2^\circ$ for T25 and $16^\circ \pm 4^\circ$ for T28. Using the best-fit models presented in Section 4.2, these angles suggest an expected backscatter ratio of 1.26 ± 0.40 for the background and 1.33 ± 0.45 for the shallow areas of Kraken North. While the average ratio of the surrounding region ($\sigma_{o,\ T25}/\sigma_{o,\ T28} = 1.56$) and areas of 2 dB change in Kraken North agree with these predictions, the backscatter ratio of $\sim$11 dB in the central region of Kraken North does not. If incident angle effects can be ruled out, additional explanations for the observed backscatter that can be considered include SAR processing artifacts, look azimuth effects, a deepening of the liquid level, wetting of marshy areas, transient surface roughening by wind or rain, and/or a surface layer with distinct dielectric properties.

The natural shape of the anomalous area argues against radar beam registration errors, boundary effects, or other potential processing artifacts (Figure 4.14). Look direction

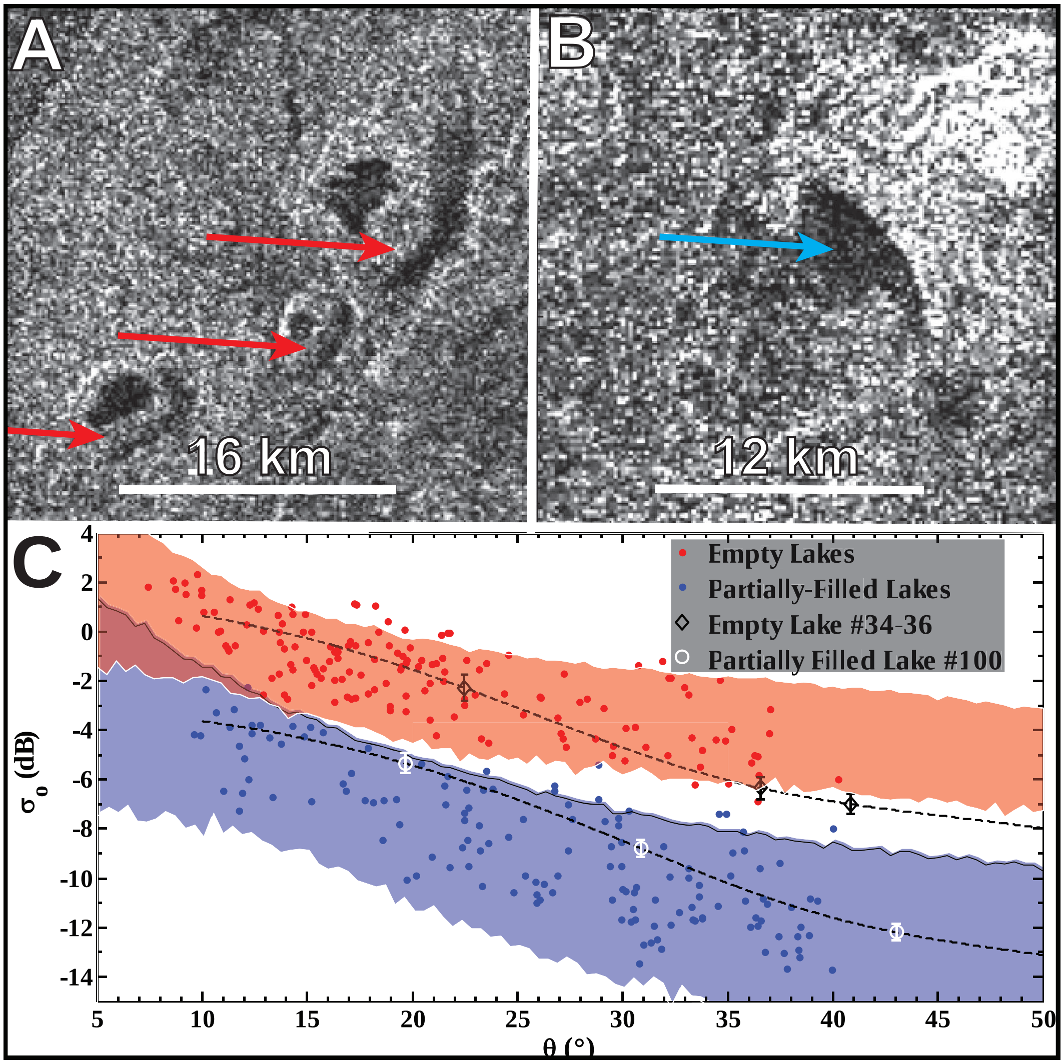

Figure 4.12: Backscatter (σ_o) values for empty and partially filled lakes observed during T16, T25, and T28 over a 3.5 year baseline in the north polar region. Images are equicylindrical projections with a logarithmic stretch from -20 dB to 0 dB. A: Empty lake features (#34 #36) with dark lakes partially filling the basin floor. Red arrows indicate areas of empty lake features used in backscatter calculations. The morphologic borders of the dark lakes were invariant across all three observations. B: Partially filled lake (#100) with blue arrow indicating area used in backscatter calculations. C: σ_o values for Empty Lakes #34 #36 and Partially Filled Lake #100 plotted on top of empty and partially filled lake classes (see Figure 4.1). Dashed lines represent the best-fit Gaussian plus diffuse scattering models for each feature. Model coefficients are listed in Table 4.1. Note that both features lie within their respective feature classes, unlike the ephemeral features observed in the south polar region.

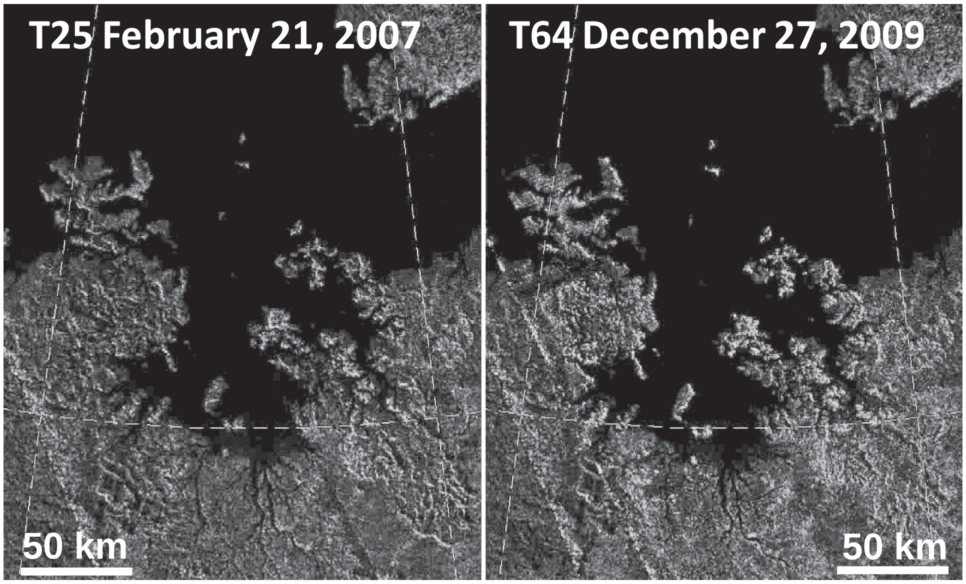

Figure 4.13: Stereographic polar projection of the southeast shoreline of Ligea Mare acquired in February 2007 (T25) and December 2009 (T64). North is up. Note that there is no visible change in shoreline position or channel morphology. Images are corrected for bulk incidence angle variations and presented in a logarithmic stretch from -20 to 0 dB.

variations are hard to rule out completely, but the homogenous appearance of the various subregions within Kraken North argue against their importance. A meter-scale deepening of a uniform liquid layer could produce an average backscatter reduction of $\sim$11 dB (see above), although there is only weak correlation among σ_o values across the feature (Figure 4.14). If the liquid level had changed, σ_o should have been reduced by a fixed ratio. Wetting of initially dry areas in a swamp like environment can also produce significant reductions in backscatter. However, the anomalous region of Kraken North is still darker than the surrounding terrain and located in the middle of the feature with even darker pixels surrounding it on all sides. Coupling this with the morphology of the drainage network suggests it is unlikely that the anomalous region is dry and topographically above its immediate surroundings. Wind roughening, while appealing because it can influence different sections of a complex shoreline morphology in different ways, would require wind patterns to be restricted to the anomalous region of Kraken North. In addition, empirical studies on Earth show that radar backscatter acquired near $\sim 10^\circ$ incidence is relatively insensitive to wind roughening [Hasselmann et al., 1978]. Hasselmann et al. [1978] find that wind roughening decreases σ_o for $\theta <\sim 10^\circ$ and increases it for $\theta >\sim 10^\circ$. Furthermore, an increase of ~ 11 dB would require RMS wave heights of cm-scale or larger, which have yet to be confirmed on Titan [Wye et al., 2009, Barnes et al., submittedb].

The remaining candidate for explaining the backscatter ratio of Kraken North is a transient surface layer with distinct dielectric properties, such as a layer of suspended or floating organic debris present in T25, but not in T28. The suspended or floating (frothy) organic debris causing the higher the σ_o in T25 would then have to sink or disperse by T28, roughly 6 weeks later. The observed differences are difficult to interpret because of the lower resolution of T25 and the fact that much of Kraken North is below the radar noise floor in T28. Future observations of Kraken Mare and detailed modeling of the effects of organic debris will help to further constrain this hypothesis.

4.4 Discussion

If the null hypothesis (change in observational geometry) and wave activity are rejected as explanations for ephemeral lake features in Titan's South Polar region, remaining possibilities that can explain observed surface changes include evaporation, infiltration, freezing, and cryovolcanism. No evidence for cryovolcanic features has been identified near the study regions [Stofan et al., 2008], so we dismiss this possibility here.

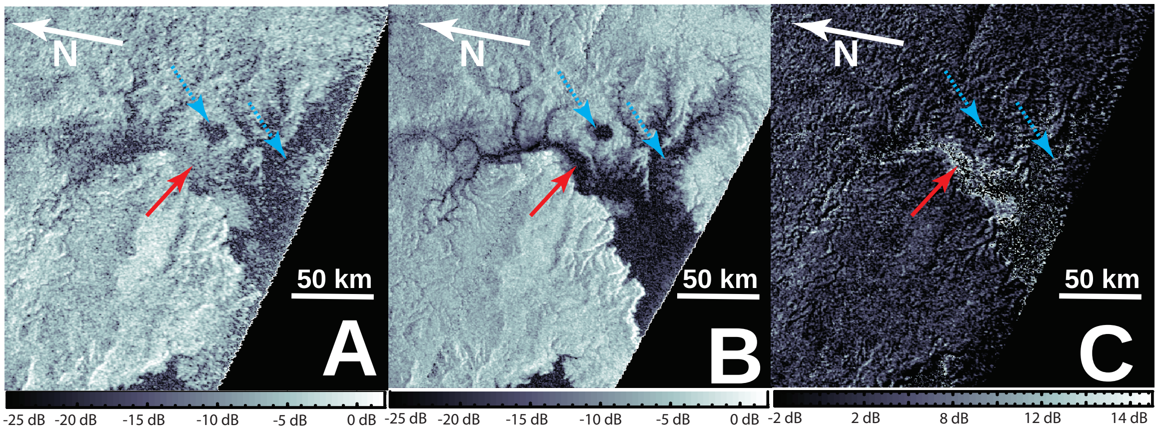

Figure 4.14: Stereographic polar projection of Kraken North, an estuary morphology in the northeastern shore of Kraken Mare. A: Logarithmic stretch of T25 (February 21, 2007) B: Logarithmic stretch of T28 (April 10, 2007) C: σ_o ratio of T25/T28 expressed in dB. Images were projected at a resolution of 128 pixels per degree and convolved with a two-pixel diameter box to reduce speckle noise. Areas outside the estuary feature have an average σ_o ratio of 1.57 dB while valid pixels within the estuary have average σ_o ratios of $\sim$11 dB (solid red arrow) and $\sim$2 dB (dashed cyan arrow), with individual pixels of up to 18 dB. However, large portions of Kraken North are below the noise floor in the T28 observation, making interpretation difficult.

Freezing may occur for a pure methane lake if the temperature of the liquid falls below 91 K [Tokano, 2009a], but this temperature is unlikely near Titan's summer pole. Cassini's Composite Infrared Spectrometry (CIRS) has not observed temperatures below 91 K in the southern high latitudes during summer [Jennings et al., 2009]. A recent GCM of Titan predicts physical temperatures remain above 91 K for the latitudes and times of the studied observations [Richardson et al., 2007]. While evaporative cooling could further reduce the temperature of the lake, it is highly unlikely that a pure methane lake would be stable long enough to completely freeze [Cordier et al., 2009]. Nitrogen would dissolve into the lake from the atmosphere, reducing the freezing temperature by up to 6 K [Lunine, 1993], below the minimum expected temperature reached through evaporative cooling [Mitri et al., 2007]. The freezing point is also reduced below the minimum expected temperature if there is a significant fraction of ethane present in the lake [Lunine, 1993].

We prefer liquid evaporation and infiltration as explanations for observed surface change. This hypothesis is supported by the recent discovery of ground fog in the vicinity of Ontario Lacus, a phenomenon which Brown et al. [2009b] argues can only exist in the presence of volatile evaporation. Mitri et al. [2007] suggest methane evaporation rates of 0.3-10 m/yr can be achieved through advective transport of subsaturated air over a lake surface, assuming horizontal wind speeds of 0.1-1 m/s. Mitchell [2008] estimates that the maximum evaporative flux during southern summer is ~2 $\mathrm{W/m^2}$, corresponding to a methane evaporation rate of ~0.3 m/yr. Newmann and Richardson [2009] find a maximum evaporation rate of ~1.6 m/yr and an average evaporation rate of ~0.5 m/yr for the time periods ($340° < L_s < 360°$) and latitudes ($60°S - 70°S$) in question. Graves et al. [submitted] find maximum evaporation rates of ~1 m/yr and average rates of ~0.5 m/yr in the south polar region between winter solstice and vernal equinox. Graves et al. [submitted] further predicts that any liquid remaining in the south polar region during southern winter is predominantly ethane, as the southern methane reservoir is exclusively seasonal in their model. These GCM results, however, represent zonally averaged evaporation. Given that only 0.4% of the observed south polar region is covered in liquid, atmospheric transport could focus available energy over the lakes by warming air parcels and increasing local evaporation. In three-dimensional GCMs, local areas within a latitude bin can typically have evaporation rates a few times higher than the zonal average [Graves and Schneider, 2009].

The average 1.0 ± 0.3 m/yr loss rate of Ontario Lacus between winter solstice and vernal equinox is inconsistent with an ethane-rich composition ($\leq 17\%$ $\mathrm{CH_4}$) according to the coupled GCM-sea model presented in Tokano [2009b]. A methane-rich composition ($\geq 62\%$ $\mathrm{CH_4}$) is consistent with the observed reduction, although Tokano [2009b] estimates a seasonal amplitude of 1-2 m as opposed to the observed 4.0 ± 1.3 m change. The observed ephemeral feature loss rates are also consistent with a predominantly methane composition. In general, the two-layer model fitting and analysis of receding shorelines at Ontario Lacus result in a liquid loss rate of order one meter-per-year, roughly consistent with the range of theoretical estimates of methane evaporation.

Available GCMs do not consider flow within a porous medium. However, data returned from the Huygens Probe suggests the presence of a damp porous regolith in Titan's equatorial region, consisting of loosely packed particles ranging in size from silt to medium sand [Lorenz et al., 2006, Zarnecki et al., 2005]. Permeability values for these particle sizes, assuming a porosity of $20\% - 30\%$, can vary by up to six orders of magnitude from 10^{-10} (silt) to 10^{-4} (medium sand) cm^2. Assuming methane as a working fluid, these permeabilities result in hydraulic conductivities (K) varying from 1 to 10^6 m/yr.

Vertical infiltration rates, which describe the rate at which liquid is absorbed into the regolith and are approximated by the hydraulic conductivity, are significantly faster than horizontal seepage rates [Hayes et al., 2008a]. Complete vertical infiltration would occur on a timescale of $\sim H/K$, where H is the liquid depth. For a 1 m deep lake on Titan, this would correspond to a timescale of 10^{-6} to 1 yr for the conductivity range above. Hence, the presence of a lake suggests that the regolith is either impermeable or the methane table exists close to the surface. When the methane table is located below the lakebed, we assume that the liquid will vertically infiltrate to the phreatic surface, creating a cylindrical column that will radially flow into the surrounding regolith [Hayes et al., 2008a].

The timescale for emptying a lake by radial flow was discussed in Hayes et al. [2008a] and can be approximated by $\tau \approx (RD)/(4KH)$, where R is the radius of the liquid and D is the distance it must travel. For a lake depth (H) of 1 m and radius (R) of 5 km, the characteristic time for emptying a lake into the regolith is ~150 years for $K = 10^4$ m/yr and ~1.5 years for $K = 10^6$ m/yr. For the time difference between T36/T49 (1.2 yr) and T39/T55 (1.5 yr), horizontal infiltration can only explain the surface change for permeabilities greater than 10^{-4} cm^2, or situations where the methane table is at a distance of order the depth of the lake or greater below the surface. The characteristic separation of features in the ephemeral regions is ~50 km. Horizontal travel over this distance corresponds to timescales of $10^2 - 10^8$ years for the expected permeability range, suggesting these features are not required to coevolve through subsurface communication, although a common alkanofer table reduction may influence all features by vast vertical infiltration.

In the presence of a porous regolith, infiltration and evaporation are interconnected. While evaporation through a saturated regolith will proceed more slowly than for an exposed lake [Saravanapavan, 2000], the interaction area is significantly greater. Depending on the diffusivity and porosity of the regolith, evaporative loss from the regional alkanofer could be greater than the loss from a lake's surface. If a lake is in interaction with an alkanofer system, its liquid level will drop through vertical infiltration as the volume of material stored in the subsurface reduces. Distinguishing between the importance of interaction with the atmosphere as compared to interaction with a regional subsurface reservoir requires additional observation, particularly the evolution of local clusters of lakes with varying size [Hayes et al., 2008a]. Observations designed to provide this information have been included in the Cassini Solstice Mission.

4.5 Summary

Ephemeral surface features have been observed in Titan's south polar region during southern summer. Two regions of overlapping coverage (T39/T55 and T36/T49) contain shallow lakes that transition into features consistent with empty lake basins. On larger scales, the shorelines of Ontario Lacus are observed to recede between ISS and RADAR imagery obtained over a baseline of four years. As of December 2009, no unambiguous changes in liquid level have been observed in the north polar region. While The northern shoreline of Kraken Mare does exhibit backscatter variations that can not be explained by geometric effects alone, the spatial variation of these changes suggest explanations other than varying liquid depth. These observations represent hydrocarbon transport in Titan's dynamic hydrologic system as Saturn approaches vernal equinox.

Backscatter cross-sections for empty and partially filled lakes on Titan form consistent and distinct feature classes that can be fit using common backscatter functions. The observed backscatter ratios between T39/T55 and T36/T49, in areas outside the ephemeral features, are consistent with an incidence angle variation produced by these models. The ephemeral features, however, have backscatter variations that are inconsistent with the models and previously observed radar returns without invoking temporal change. Morphologic variations between the observations also imply that ephemeral features in T36/T49 and T39/T55 represent physical surface change.

Liquid reductions of $\sim$1 m/yr are derived from the observations using a simple two-layer model. The shape of the backscatter function for empty and partially filled lake classes supports the use of a simple model to estimate transient liquid depth. Our calculations of liquid loss by evaporation and infiltration are consistent with changes both in the depth of partially filled lakes and complete drying of other lakes.

Analysis of shoreline recession around Ontario Lacus provides an independent measure of loss that is consistent with the modeled ephemeral features. Altimetry profiles intersecting Ontario Lacus provide topographic information used to calculate a loss tangent of $\tan\Delta = (9.2^{+2.5}_{-2.0}) \times 10^{-4}$ for the liquid mixture and generate a near-shore bathymetry map [Hayes et al., 2010]. Bathymetry slopes inversely correlate to observed shoreline recession magnitudes and suggest 1.0 ± 0.3 m/yr loss rates of Ontario Lacus between winter solstice and vernal equinox.

Theoretical estimation of methane evaporation rates for the latitudes ($60°\mathrm{S} - 70°\mathrm{S}$) and times ($340° < L_s < 360°$) of the ephemeral observations are consistent with the value of $\sim$1 m/yr estimated from SAR returns. The reduction in the level of Ontario Lacus agrees with the methane-rich sea model presented in Tokano [2009b]. Possible explanations for the observed changes include liquid evaporation and infiltration. Freezing is unlikely given the temperatures and constituents known or suspected to be present in and above the lakes, and there are no cyrovolcanic features identified in the study region. Infiltration into a static hydrologic system is unlikely given the timescales involved. However, infiltration into a dynamic hydrologic system with a regionally varying phreatic surface is possible. These observations demonstrate that Titan’s surface plays an active role in its methane cycle and can be used to further constrain volatile transport estimates and describe the evolution of Titan’s hydrologic system over both seasonal and orbital time frames.

Acknowledgements

The authors would like to thank Dr. Jakob Van Zyl of the Jet Propulsion Laboratory for helpful discussions, and the Cassini engineering team, without whom the data presented here would not have existed. This work was supported by the Cassini Project, managed by the Jet Propulsion Laboratory, California Institute of Technology, under a contract with the National Aeronautics and Space Administration, as well as by NASA’s Graduate Student Researchers Program.

Chapter 5

Upcoming Observations

The discovery of lakes, channels, and active atmospherically mediated hydrology arguably makes Titan the most Earth-like planetary body in the solar system, with a volatile cycle which incorporates solid, liquid, and gaseous phases of methane. Understanding the nature of Titan's hydrologic system will teach us about the history of volatile compounds across the solar system and the development and evolution of Earth-like planets both in our own solar system and around other stars. This research presented in this thesis has investigated the distribution, physical properties, and seasonal variation of lacustrine features on Titan. The key questions addressed include

[1] *How does methane transport vary seasonally and geographically on Titan?*

[2] *What is the importance of subsurface transport, relative to atmospheric and surface processes, in Titan's methane cycle?*

[3] *What are the differences and similarities between Titan and Earth's hydrologic cycles, and how can we use aspects of Titan's methane cycle to learn more about volatile cycles and their evolution on planets in general?*

This chapter will both review and expand upon the foundations of the research presented in preceding chapters and describe how upcoming opportunities during the Cassini Solstice Mission (Figure 5.1 will further illuminate the questions posed above.

Chapter 2 described the evolutionary lake classification performed in Hayes et al. [2008a]. Lacustrine features identified on Titan are currently grouped into three evolutionary classes: empty lake basins, partially filled lakes, and dark or liquid filled lakes [Stofan et al., 2007a, Hayes et al., 2008a]. Partially filled lakes have radar returns consistent with incident radiation penetrating a liquid layer and interacting with the lakebed, while dark lakes completely reflect and absorb the incident microwave energy from the Ku-Band Cassini RADAR [Paillou et al., 2008b, Hayes et al., 2008a]. Empty lakes are brighter than their exteriors in both nadir and off-nadir radar observations, suggesting compositional variations. Higher relative backscatter at large off-nadir angles ($> 30^\circ$) also suggests a stronger volume scattering component. All lake classes are restricted to latitudes poleward of 55° and cover 1.5% of Titan's observed surface. There is a significant dichotomy in polar lake distributions, with liquid filled lakes covering 10% of the area in the north but only 0.4% in the south (poleward of 55°) [Hayes et al., 2008a, Aharonson et al., 2009]. Aharonson et al. [2009]

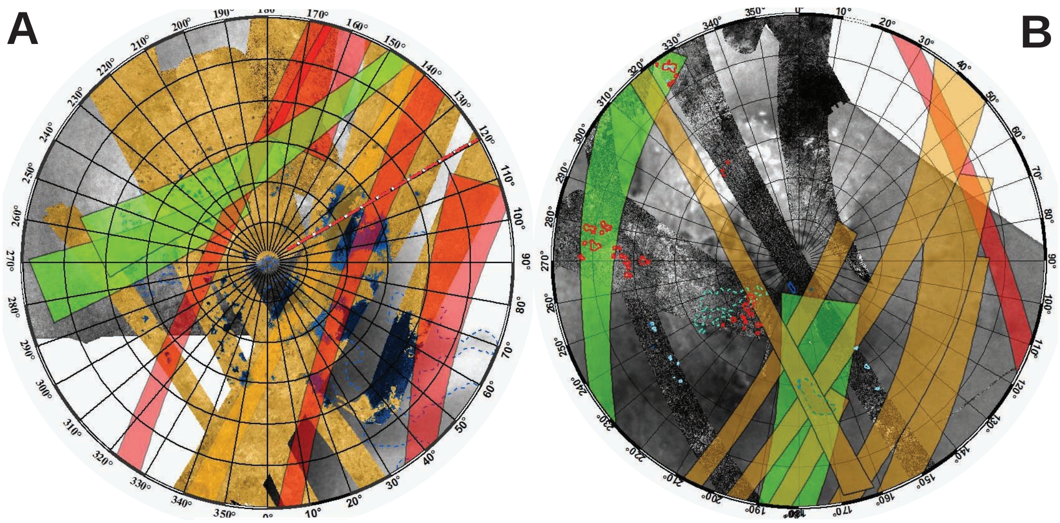

Figure 5.1: Planned polar coverage for the RADAR instrument during the Cassini Solstice Mission. A: North polar region. B: South polar region.

has attributed this dichotomy to a seasonal asymmetry in incident solar flux resulting from Saturn's eccentricity and Titan's solar longitude at perihelion. In Chapter 4, ephemeral features were described in the south which were initially consistent with partially filled lakes and later transitioned into empty lake basins [Hayes et al., 2011]. These transient features represent direct evidence for surface liquid playing an active role in Titan's methane cycle.

The morphologies of lakes on Titan spans the range of observed morphologies on Earth. Lakes with distinctly polygonal shapes, complex shoreline geometries, and associated channels are similar to terrestrial drainage lakes dominated by surface flow. Comparatively smooth lake boundaries with distinct shorelines and no associated channel networks are consistent with seepage lakes interacting predominantly with a local alkanofer system (the hydrocarbon-based analogy to a groundwater system on Earth) [Hayes et al., 2008a]. Future work will expand this evolutionary classification into morphologic categories. As the boundaries between morphologic classifications are overlapping, features will be cataloged using specific observables such as presence or absence of observable channel networks, circularity, topographic signature, and degree of isolation. Understanding the geographic correlations between morphologic indicators present in the observed lakes will help to determine which features are dominated by subsurface hydrology and provide information regarding regional methane transport, addressing all three of the key science questions listed above.

For the majority of the Cassini mission, the north polar region has been in complete darkness and observations of the north polar lake district have been restricted to the RADAR instrument. As Titan passes through vernal equinox and heads toward summer solstice, the north is revealed to the Imaging Science Subsystem (ISS) and Visual and Infrared Mapping Spectrometer (VIMS), which view of Titan's surface in the near and mid-infrared, respectively. While the SAR data provide the highest resolution (~ 300 m/pixel) views of Titan's surface, the ISS and VIMS instruments provide spectral information and observations of areas not covered by the RADAR. The near-global coverage of the ISS instrument will allow updated estimates of the total surface liquid reservoir. The VIMS instrument, which recently obtained high-resolution observations of the area surrounding Kraken Mare (Figure 5.2), provides a new view of the lakes which will permit a better understanding of their role in the hydrologic system. Preliminary results from the first inter-comparison between VIMS and RADAR in the north polar lake district shows that some empty lake features have a high 5 $\mu\mathrm{m}$ albedo while others do not. The initial interpretation of these features are that the 5 $\mu\mathrm{m}$ bright reflections arise from evaporite deposits, suggesting some empty lakes have a more active role in the surface hydrology than others [Barnes et al., submitteda]. Correlations of these observations against available topography derived from the RADAR data will provide additional information. The combination of spatial resolution from RADAR and spectral information from VIMS is a powerful and new tool for studying Titan's lakes. VIMS observations of additional areas in the north polar regions will be acquired over the next two years and inter-comparisons with RADAR and ISS data are planned.

In addition to providing spectral information and filling in gaps in RADAR coverage, VIMS and ISS observations of Titan's lakes also provide repeat observations that can be used to study seasonal change [Barnes et al., 2009, Turtle et al., 2009a]. The area surrounding Kraken Mare, where recent VIMS and ISS images have been targeted, were taken inbetween RADAR observations of the area obtained in early 2007 (Titan flybys T25 and T28) and late 2009 (T64). As discussed in Chapter 4, the RADAR observations show no evidence for unambiguous surface change in the north polar region [Hayes et al., 2011]. In region surrounding Kraken Mare, the RADAR data can be used to calibrate inter-comparisons between RADAR and ISS / VIMS. Initial work on these comparisons suggest that there is a strong correlation between resolvable lacustrine features amongst all three instruments (Figures 5.2 and 5.3). Calibrating the inter-comparability of RADAR, ISS, and VIMS will lead to a much larger dataset for studying seasonal change on Titan and help constrain the methods and volume of methane transport both between and within the polar regions. This capability will directly address key question [1].

An example of RADAR and ISS data being used to study seasonal change on Titan

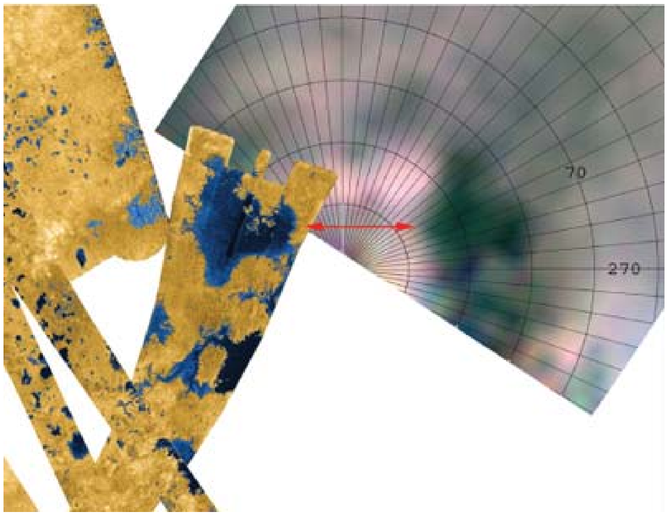

Figure 5.2: Preliminary comparison between VIMS and SAR data of Titan's Lakes. Newly acquired high-resolution VIMS images of this area are discussed in Barnes et al. [submittedb]. VIMS spectral information was able to deduce that ethane was present in the liquid composition [Brown et al., 2008].

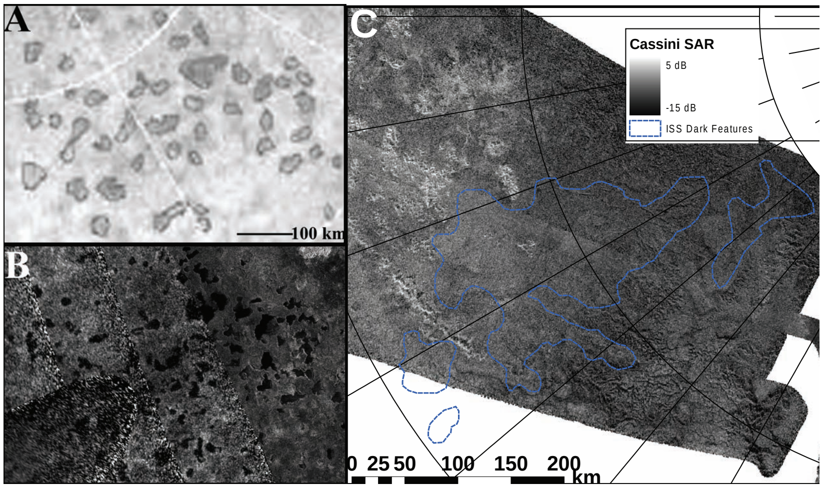

Figure 5.3: Preliminary comparison between ISS and SAR data of hydrologic features on Titan. A: ISS view of North Polar Lakes. B: SAR view of North Polar Lakes. C: SAR image of Arrakis Planitia obtained in December 2008 with outline of ISS dark albedo region from June 2005. No evidence for surface liquid is present in the SAR image, although the western border of the ISS feature lines up with bright humocky terrain shown to be topographically raised in other areas of Titan.

was presented in Chapter 4 and recently published in Hayes et al. [2011], which discusses observations of shoreline recession between ISS and RADAR images of Ontario Lacus (Figure 5.4). Ontario Lacus is the largest known lake in south polar region. The recession, occurring between June 2005 and July 2009, is shown in Chapter 3 to be inversely proportional to near-shore slopes estimated from altimetric profiles and the exponential decay of radar backscatter by Hayes et al. [2010]. This analysis was able to constrain the average depth reduction of Ontario Lacus to 4 ± 1.3 m over the four years between observations. An additional example of RADAR / ISS change detection is Arrakis Planitia (Figure 5.3), an area of $\sim 30,000\ \mathrm{km}^2$ located near (80°S,120°W) which was observed to be ISS dark in June 2005. Initial observations of Arrakis Planitia, however, showed that it had similar albedo to the surrounding terrain in June 2004 [Turtle et al., 2009a]. Subsequent SAR images of the area obtained in December 2008 show no evidence for surface liquid, suggesting that any liquid present in June 2005 has since evaporated into the atmosphere or infiltrated into the subsurface [Turtle et al., 2011]. In addition, the border of Arrakis Planitia as observed by ISS in June 2005 correlates with the morphologic boundaries of mountainous terrain and topographic depressions observed by the RADAR (Figure 5.3). Examples of change detection measurements and inter-instrument comparison such as these will address key questions [1] and [2].

Topographic data of Titan's surface is currently available from three techniques; altimetry, SAR topography, and stereogrammetry. The altimetry mode of the Cassini RADAR provides only limited coverage and does not always intersect SAR data [Elachi et al., 1991]. SAR-Topography, or SAR-Topo, is a processing technique which makes use of the overlapping beam patterns of the Cassini RADAR [Stiles et al., 2009]. The average height in the area of overlap between adjacent beams can be estimated by comparing the relative return measured in each beam to their known gain patterns. SAR-Topo results are available for nearly every SAR swath and provide thin strips of topographic measurements throughout the north and south polar regions. Stereogrammetry requires a detailed sensor model to reliably estimate three-dimensional coordinates from matching tie points in coincident SAR swaths [Kirk et al., 2007]. Such a model has been developed by the U.S. Geological Survey (USGS) and is currently being used to generate the first DEMs of Titan's surface [Kirk et al., submitted].

Preliminary analysis of the SAR-Topo and Stereogrammetry datasets reveal that the northern seas, or mare, are located in the lowest topographic regions and that their shorelines elevations are consistent to within the $\sim$ 150 m absolute accuracy of the current technique [Kirk et al., submitted]. The area of empty and partially filled lakes, which flank the mare to the south, lie ∼400 m above the mare shorelines [Hayes et al., 2008b]. An area of small lakes that are consistent with a seepage-dominated morphology, which are located

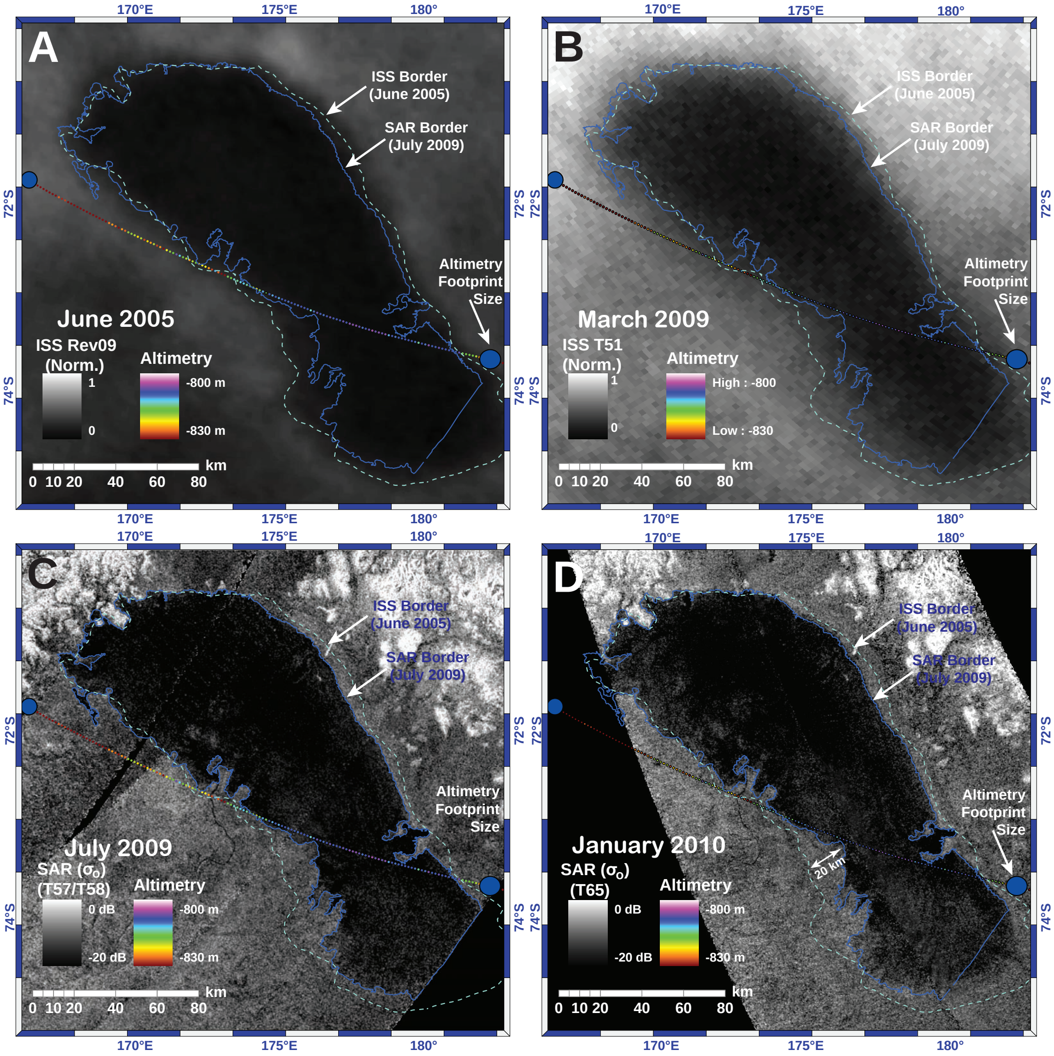

Figure 5.4: Equidistant Cylindrical projections of Ontario Lacus. The lake border from the 2005 ISS image is shown in cyan, while the 2009 SAR border is blue. T49 altimery data is overlain. Heights are calculated from echo center-of-mass and referenced to Titan's geoid as presented in Iess et al. [2010]. Altimetry footprint size is shown using blue circles; A: ISS image obtained in June 2005 (Rev09). ISS shoreline is defined by following a constant contour of relative brightness referenced to local offshore pixel intensity; B: ISS image obtained in March 2009 (T51). C: SAR image obtained in June and July 2009 (T57/T58). D: SAR image obtained in January 2010 (T65).

between 120°W and 160°W, lie 600-800 m above the mare, producing a potential hydrologic head for subsurface transport [Hayes et al., 2008b]. Empty lakes observed in varying locations throughout the north polar regions are seen as 150-300 m depressions by all three topographic techniques [Hayes et al., 2008a,b]. While lakes near the mare arguably lie at similar elevations to the sea shorelines distant lakes, on the other hand, lie topographically elevated by 400-800 m. In some cases, these lakes lie in a state of local hydrologic disequilibrium, a configuration which requires an active hydrologic system. These observations suggest that the lakes may be interacting with a subsurface alkanofer. If present, such an alkanofer could represent the dominant component of Titan's liquid reservoir and play an important role in the hydrologic system. Targeted observations of these areas are planned during the Cassini Solstice mission in order to see how they temporally evolve. The evolution of lakes of difference sizes in these areas can provide constraints on the properties of the local porous regolith and importance of subsurface transport in Titan's hydrologic system. As shown in Chapter 2, small lakes will be dominated by interaction with the subsurface while larger lakes will be dominated by interaction with the atmosphere [Hayes et al., 2008a]. Observations of these areas and their temporal evolution will directly address key question [2].

The rate of liquid inflow or outflow from a lake through the subsurface is governed by topography and the properties of the local porous medium. The Huygens Probe provided information constraining soil properties near Titan's equator (10°S) and suggested the presence of a damp porous medium consisting of loosely packed particles between the size of silt to medium sand [Lorenz et al., 2006, Zarnecki et al., 2005]. The material properties observed by Huygens can be used as a starting point to model subsurface transport in Titan's northern latitudes. Fluid migration, which is driven by changes in the hydrologic head, can be represented using the ground water flow equation:

$$\frac{\partial h}{\partial t} = \frac{1}{\phi}\nabla \left[K \cdot h\nabla h\right] + P \tag{5.1}$$

where h is the height of the alkanofer surface, t is time, ϕ is porosity, P is the net loss/gain from precipitation and evaporation, and K is the hydraulic conductivity ($K = \kappa\rho g/\mu$). Hydraulic conductivity, which describes the ability of a liquid to flow through pore space, depends on the permeability of the porous medium (κ), liquid density (ρ), gravity (g), and dynamic viscosity (μ). Interaction between a single hydrocarbon lake and its local porous medium was investigated by Hayes et al. [2008a] using the Boussinesq equation, which is a one-dimensional form of Equation 5.1 assuming cylindrical symmetry (Figure 2.8). Results suggested that the evolution of lakes of varying size will provide constraints on the properties of the local porous medium and potentially describe the importance of subsurface flow in Titan's hydrologic cycle. The results of Hayes et al. [2008a] can be expanded by solving the three-dimensional form of the groundwater flow equation (Equation 5.1) using high-resolution DEMs created from SAR Stereogrammetry.

Digital Elevation Models (DEMs), created using the commercial software package Socet Set marketed by BAE Systems, can be tied to SAR-Topo and Altimetry data, allowing for the generation of and comparison between high-resolution topography in areas of interest. Such DEMs can be used to find local solutions to Equation 5.1 using finite-element analysis for a range of material properties. An important region to be analyzed is located in the area immediately surrounding the southernmost shore of Kraken Mare depicted in Figure 5.2. This region will be reobserved by the RADAR in May (T83) and September (T86) 2012, providing a five-year baseline for temporal evolution since the original observations in 2007. The observations obtained in 2012 can be compared to subsurface flow models in order to constrain the material properties of the local regolith and define the required importance of subsurface transport of liquid methane and ethane. Of the remaining regions of interest specific to this analysis, the highest priority is an area of small lakes consistent with a seepage dominated morphology located between 120°W and 160°W. This region with be reobserved by the RADAR in May (T91) and July (T92) of 2013, providing both a six-year baseline for temporal evolution and overlapping data from which to derive stereo DEMs. Depending on the results of data inter-comparison, VIMS, ISS, and IRTF data may provide additional regions of interest where overlapping SAR swaths provide the required DEM and VIMS/ISS data provide information regarding temporal evolution. The results of this modeling will directly address key questions [1] and [2].

The fundamental goal of the presented research is to understand the role of methane and ethane in Titan's hydrologic system. Observed seasonal changes will provide information regarding lake composition because, while methane is volatile over seasonal timescales, ethane can only be transported over orbital timescales and other proposed lake constituents are stable over geologic time [Lunine, 1993, Aharonson et al., 2009, Cordier et al., 2009]. Constructed DEMs and the results of the hydrologic modeling can provide information regarding the importance of subsurface transport and constrain regolith properties when compared against the T83 and T86 SAR observations. When combined with the morphologic classification scheme outlined above such modeling will also provide information regarding the extent of a regional subsurface reservoir. On Earth non-oceanic crustal water accounts for a small fraction of the total supply. On Titan the situation could be reversed, with significantly more liquid stored in the regolith than in the lakes. The results of this study can also be used as initial conditions for future Global Climate Models (GCMs) of Titan' methane cycle. The current generation of GCMs do not include a spatially varying methane lake distribution, model flow and loss through a subsurface regolith, or topographic variation. They also do not, as of yet, incorporate observations of seasonal variation in lake depth and distribution which can be used for model calibration and verification. Thus, upcoming research opportunities will not only substantially increase our knowledge of Titan's hydrologic cycle, but also provide atmospheric scientists with the tools they need to adequately model Titan's climate.

The upcoming research opportunities provided by the Cassini Solstic mission will compliment the work presented in the preceding chapters of this thesis and result in a better understanding of Titan's hydrologic system by addressing all three of the key questions mentioned above. Methane transport models derived from lacustrine feature distribution and relative topography can be used to predict timescales for change and help verify GCMs. Observations of lake distribution and seasonal variation will help to constrain Titan's hydrocarbon inventory and the methods and volumes of transport both between and within the polar regions. Titan's methane cycle represents the only known extraterrestrial volatile system that currently incorporates solid, liquid, and gaseous phases. Studying the differences and similarities between Titan's methane cycle and Earth's water cycle will ultimately teach us about the development and evolution of volatile cycles on any planetary body, as well as provide context for future discoveries in the field of extrasolar planets.

Appendix A

Software for Cassini RADAR Data Manipulation

When working with any new dataset, a significant amount of effort must be invested in order to understand and manipulate the released data. In an effort to make the Cassini SAR dataset more accessible to the community, I have made many of my data manipulation and management scripts publicly available at the following web address:

`www.gps.caltech.edu/~hayes/Public/Matlab_Code/`

The files are also available from the Caltech thesis repository:

`thesis.library.caltech.edu/`

The scripts are written in Matlab and compatible with versions 7 and above. A list of provided functions, alongside brief descriptions, is presented below. Each script includes a full header and a list of any required toolboxes, data files, or subscripts.

read_isis.m	Reader for PDS, ISIS band sequential and tiled data cubes.
replace_isis.m	Writer for PDS and ISIS data formats.
pds_labelparsef_v2.m	Parses PDS/ISIS cube labels and returns keyword values in a structure.
sar_readsbdr.m	Reader for Cassini SBDR and LBDR data products.
sar_readabdr.m	Reader for Cassini ABDR data products.

shp_find_swaths.m	Find SAR BIDR cubes which contain overlap with input lat/lon polygons.
shp_find_shp.m	Find overlap between two sets of lat/lon polygons.
analyze_shp.m	Calculate average SAR backscatter within set of lat/lon polygons.
analyze_shp_manual.m	Calculate average SAR backscatter within set of lat/lon polygons using manual area selection.
shptogrid.m	Create gridded raster from a set of lat/lon polygons.
sartopo_make_shapefile.m	Create shapefile from input sartopo data file.
radiometry_make_shapefile.m	Create shapefile from input radiometry data file.
sbdr_make_shapefile.m	Create shapefile from specified keywords in SBDR data.
bidr_proj_v2.m	Calculate line/sample positions for lat/lon values in PDS or ISIS cubes.
bidr_proj_inv_v2.m	Calculate lat/lon values for line/sample positions in PDS or ISIS cubes.
calc_insolation.m	Calculate insolation at the top of the atmosphere for a given set of orbital parameters.
orbelm_swift.m	Calculate Saturn's orbital elements using the results of the SWIFT integrator.
orbelm_secular.m	Calculate Saturn's orbital elements using secular theory presented in Murray and Dermott [1999].
orbelm_jpl.m	Calculate Saturn's orbital elements using the JPL Horizons database.
orbelm_xv2orbelm.	Calculate orbital elements from position and velocity.

Bibliography

O. Aharonson, Hayes, A.G., J.I. Lunine, R.D. Lorenz, M.D. Allison, and C. Elachi. An asymmetric distribution of lakes on Titan as a possible consequence of orbital forcing. Nature Geosciences, 2:851–854, November 2009. doi: 10.1038/ngeo698.

M. Barmatz and K. L. Mitchell. personal communication, 2009.

J. W. Barnes, R. H. Brown, J. M. Soderblom, L. A. Soderblom, R. Jaumann, B. Jackson, S. Le Mouélic, C. Sotin, B. J. Buratti, K. M. Pitman, K. H. Baines, R. N. Clark, P. D. Nicholson, E. P. Turtle, and J. Perry. Shoreline features of Titan's Ontario Lacus from Cassini/VIMS observations. Icarus, 201:217–225, May 2009. doi: 10.1016/j.icarus.2008.12.028.

J. W. Barnes, J. Bow, J. Schwartz, R. H. Brown, J. Soderblom, A. G. Hayes, S. Le Mouélic, S. Rodriguez, C. Sotin, R. Jaumann, K. Stephan, L. A. Soderblom, R. N. Clark, B. J. Buratti, K. H. Baines, and P. D. Nicholson. Widespread organic evaporite deposits on Saturn's moon Titan. Icarus Notes, submitteda.

J. W. Barnes, J. M. Soderblom, R. H. Brown, L. A. Soderblom, R. Jaumann, B. Jackson, S. Le Mouélic, S. Rodriguez, C. Sotin, B. J. Buratti, K. H. Baines, R. N. Clark, and P. D.

Nicholson. Wave Constraints for Titan's Jingpo Lacus and Kraken Mare from VIMS Specular Reection Lightcurves. Icarus, submittedb.

J. Barthel and R Buchner. High frequency permittivity and its use in the investigation of solution properties. Pure and Applied Chemistry, 63:1473–1482, 1991.

P. Beckmann and A. Spizzichino. The scattering of electromagnetic waves from rough surfaces. Norwood, MA, Artech House, Inc., 1987, 511 p., 1963.

G. J. Black, D. B. Campbell, and P. D. Nicholson. Icy Galilean satellites: Modeling radar reflectivities as a coherent backscatter effect. Icarus, 151:167–180, June 2001. doi: 10.1006/icar.2001.6616.

M. E. Brown, E. L. Schaller, H. G. Roe, C. Chen, J. Roberts, R. H. Brown, K. H. Baines, and R. N. Clark. Discovery of lake-effect clouds on Titan. Geophysical Research Letters, 36:L1103–L1108, January 2009a. doi: 10.1029/2008GL035964.

M. E. Brown, A. L. Smith, C. Chen, and M. Ádámkovics. Discovery of fog at the south pole of Titan. Atrophysical Journal Letters, 706:L110–L113, November 2009b. doi: 10.1088/0004-637X/706/1/L110.

R. Brown, J. P. Lebreton, and W. Hunter. Titan from Cassini-Huygens. Springer, 2010. ISBN 9781402092145.

R. H. Brown, L. A. Soderblom, J. M. Soderblom, R. N. Clark, R. Jaumann, J. W. Barnes, C. Sotin, B. Buratti, K. H. Baines, and P. D. Nicholson. The identification of liquid ethane in Titan's Ontario Lacus. Nature, 454:607–610, July 2008. doi: 10.1038/nature07100.

G. J. Brunskill and D. W. Schindler. Geography and bathymetry of selected lake basins, Experimental Lakes Area, northwestern Ontario. J. Fish Research Board Canada, 28: 139–155, 1971.

D. B. Campbell, G. J. Black, L. M. Carter, and S. J. Ostro. Radar Evidence for Liquid Surfaces on Titan. Science, 302:431–434, October 2003. doi: 10.1126/science.1088969.

D. Cordier, O. Mousis, J. I. Lunine, P. Lavvas, and V. Vuitton. An Estimate of the Chemical Composition of Titan's Lakes. The Astrophysical Journal Letters, 707:L128–L131, December 2009. doi: 10.1088/0004-637X/707/2/L128.

F. B. Daniels. A theory of radar reflection from the Moon and planets. Journal Of Geophysical Research, 66:1781–1788, June 1961. doi: 10.1029/JZ066i006p01781.

M.C. Dobson, F.T. Ulaby, M.T. Hallikainen, and M.A. El-Rayes. Microwave dielectric behavior of wet soil-part ii: Dielectric mixing models. Geoscience and Remote Sensing, IEEE Transactions on, GE23(1):35–46, January 1985. ISSN 0196-2892. doi: 10.1109/TGRS.1985.289498.

C. Elachi and J. van Zyl. Introduction to the Physics and Techniques of Remote Sensing: Second Edition. John Wiley, 2006. ISBN 100471475696.

C. Elachi, E. Im, L. E. Roth, and C. L. Werner. Cassini titan radar mapper. Proceedings of the IEEE, 79(6):867 –880, June 1991. ISSN 0018-9219. doi: 10.1109/5.90164.

C. Elachi, M. D. Allison, L. Borgarelli, P. Encrenaz, E. Im, M. A. Janssen, W. T. K. Johnson, R. L. Kirk, R. D. Lorenz, J. I. Lunine, D. O. Muhleman, S. J. Ostro, G. Picardi,

F. Posa, C. G. Rapley, L. E. Roth, R. Seu, L. A. Soderblom, S. Vetrella, S. D. Wall, C. A. Wood, and H. A. Zebker. Radar: The Cassini Titan Radar Mapper. Space Science Reviews, 115:71–110, December 2004. doi: 10.1007/s11214-004-1438-9.

C. Elachi, S. Wall, M. Allison, Y. Anderson, R. Boehmer, P. Callahan, P. Encrenaz, E. Flamini, G. Franceschetti, Y. Gim, G. Hamilton, S. Hensley, M. Janssen, W. Johnson, K. Kelleher, R. Kirk, R. Lopes, R. Lorenz, J. Lunine, D. Muhleman, S. Ostro, F. Paganelli, G. Picardi, F. Posa, L. Roth, R. Seu, S. Shaffer, L. Soderblom, B. Stiles, E. Stofan, S. Vetrella, R. West, C. Wood, L. Wye, and H. Zebker. Cassini Radar Views the Surface of Titan. Science, 308:970–974, May 2005. doi: 10.1126/science.1109919.

C. W. Fairall, E. F. Bradley, D. P. Rogers, J. B. Edson, and G. S. Young. Bulk parameterization of air-sea fluxes for Tropical Ocean-Global Atmosphere Coupled-Ocean Atmosphere Response Experiment. Journal of Geophysical Research, 101:3747–3764, February 1996. doi: 10.1029/95JC03205.

P. Ford. personal communication, 2010.

T. Gehrels, L. R. Baker, E. Beshore, C. Blenman, J. J. Burke, N. D. Castillo, B. Dacosta, J. Degewij, L. R. Doose, J. W. Fountain, J. Gotobed, C. E. Kenknight, R. Kingston, G. McLaughlin, R. McMillan, R. Murphy, P. H. Smith, C. P. Stoll, R. N. Strickland, M. G. Tomasko, M. P. Wijesinghe, D. L. Coffeen, and L. W. Esposito. Imaging photopolarimeter on Pioneer Saturn. Science, 207:434–439, January 1980. doi: 10.1126/science.207.4429.434.

J. W. Goodman. Some fundamental properties of speckle. Journal of the Optical Society of America (1917-1983), 66:1145–1150, November 1976.

R. Grard, M. Hamelin, J. J. López-Moreno, K. Schwingenschuh, I. Jernej, G. J. Molina-Cuberos, F. Simões, R. Trautner, P. Falkner, F. Ferri, M. Fulchignoni, R. Rodrigo, H. Svedhem, C. Béghin, J.-J. Berthelier, V. J. G. Brown, M. Chabassière, J. M. Jeronimo, L. M. Lara, and T. Tokano. Electric properties and related physical characteristics of the atmosphere and surface of Titan. Planetary and Space Science, 54:1124–1136, October 2006. doi: 10.1016/j.pss.2006.05.036.

S. Graves and T. Schneider. personal communication, 2009.

S. D. Graves, T. Schneider, E. L. Schaller, and M. E. Brown. Causes of titan's lake asymmetry and cloud distribution and prediction of future changes. Journal of Geophysical Research: Planets, submitted.

T. Hagfors. Backscattering from an undulating surface with applications to radar returns from the Moon. Journal Of Geophysical Research, 69:3779–3784, September 1964. doi: 10.1029/JZ069i018p03779.

T. Hagfors. Remote probing of the moon by infrared and microwave emission and by radar. Radio Science, 5:189–227, 1970. doi: 10.1029/RS005i002p00189.

J.K. Hargreaves. Radio Observations of the Lunar Surface. Proceedings of the Physical Society of London, B73:536–537, May 1959.

K. Hasselmann, W. Alpers, D. Barick, D. Crombie, C. Flachi, A. Fung, H. van Hutten, W. Jones, G. P. de Loor, B. Lipa, R. Long, D. Ross, C. Rufenach, W. Sandham, O. Shemdin, C. Teague, D. Trizna, G. Valenzuela, E. Walsh, F. Wentz, and J. Wright. Radar measurements of wind and waves. Boundary-Layer Meteorology, 13:405–412, January 1978. doi: 10.1007/BF00913885.

A. G. Hayes, O. Aharonson, P. Callahan, C. Elachi, Y. Gim, R. Kirk, K. Lewis, R. Lopes, R. Lorenz, J. Lunine, K. Mitchell, G. Mitri, E. Stofan, and S. Wall. Hydrocarbon lakes on Titan: Distribution and interaction with a porous regolith. Geophysical Research Letters, 35:9204–9208, May 2008a. doi: 10.1029/2008GL033409.

A. G. Hayes, O. Aharonson, D. Stevenson, J. Lunine, R. Lorenz, R. Kirk, B. Stiles, K. Mitchell, R. Lopes, and S. Wall. Titan's global lake distribution and implied hydrocarbon hydrology from Cassini SAR imagery and topography. AGU Fall Meeting Abstracts, page D7, December 2008b.

A. G. Hayes, A. S. Wolf, O. Aharonson, H. Zebker, R. Lorenz, R. L. Kirk, P. Paillou, J. I. Lunine, L. Wye, P. Callahan, S. Wall, and C. Elachi. Bathymetry and Absorptivity of Titan's Ontario Lacus. Journal of Geophysical Research: Planets, 115:E09009, 2010. doi: 10.1029/2009JE003557.

A. G. Hayes, O. Aharonson, J. I. Lunine, R. L. Kirk, H. A. Zebker, L. C. Wye, R. D. Lorenz, E. P. Turtle, P. Paillou, G. Mitri, S. D. Wall, E R. Stofan, K. L. Mitchell, C. Elachi, and The Cassini RADAR Team. Transient Surface Liquid in Titan's Polar Regions from Cassini. Icarus, 211, 2011. doi: 10.1016/j.icarus.2010.07.017.

Hayes, A. G. Exploring Lakes on Titan. Astronomy Beat, Astronomy Society of the Pacific, 20, September 2010.

D. M. Hunten. A Titan atmosphere with a surface temperature of 200K. In D. M. Hunten & D. Morrison, editor, NASA Conference Publication, volume 2068 of NASA Conference Publication, pages 127–140, December 1978.

Christopher Huygens. In: Systema saturnium. Hauge, 1659.

L. Iess, N. J. Rappaport, R. A. Jacobson, P. Racioppa, D. J. Stevenson, P. Tortora, J. W. Armstrong, and S. W. Asmar. Gravity Field, Shape, and Moment of Inertia of Titan. Science, 327:1367–1369, March 2010. doi: 10.1126/science.1182583.

M. A. Janssen, R. D. Lorenz, R. West, F. Paganelli, R. M. Lopes, R. L. Kirk, C. Elachi, S. D. Wall, W. T. K. Johnson, Y. Anderson, R. A. Boehmer, P. Callahan, Y. Gim, G. A. Hamilton, K. D. Kelleher, L. Roth, B. Stiles, A. Le Gall, and the Cassini Radar Team. Titan's surface at 2.2-cm wavelength imaged by the cassini radar radiometer: Calibration and first results. Icarus, 200:222–239, March 2009. doi: 10.1016/j.icarus.2008.10.017.

D. E. Jennings, F. M. Flasar, V. G. Kunde, R. E. Samuelson, J. C. Pearl, C. A. Nixon, R. C. Carlson, A. A. Mamoutkine, J. C. Brasunas, E. Guandique, R. K. Achterberg, G. L. Bjoraker, P. N. Romani, M. E. Segura, S. A. Albright, M. H. Elliott, J. S. Tingley, S. Calcutt, A. Coustenis, and R. Courtin. Titan's Surface Brightness Temperatures. Astrophysical Journal, 691:L103–L105, February 2009. doi: 10.1088/0004-637X/691/2/L103.

Junwei Jiang and Roy Plotnick. Fractal analysis of the complexity of united states coastlines. Mathematical Geology, 30(5):535–546, July 1998.

D. W. Johnson. Shore processes and shoreline development. John Wiley & Sons, Inc., London: Chapman & Hall, Limited., 1919.

R. L. Kirk, E. Howington-Kraus, B. L. Redding, T. L. Becker, E. M. Lee, B. W. Stiles, S. Hensley, A. G. Hayes, R. M. Lopes, K. L. Lorenz, K. L. Mitchell, J. Radebaugh, F. Paganelli, L. A. Soderblom, E. R. Stofan, C. A. Wood, S. D. Wall, and the Cassini Radar Team. First stereoscopic radar images of titan. In Lunar and Planetary Institute Conference Abstracts, volume 38 of Lunar and Planetary Institute Conference Abstracts, page 1427, March 2007.

R. L. Kirk, E. Howington-Kraus, B. L. Redding, T. L. Becker, E. M. Lee, B. W. Stiles, S. Hensley, A. G. Hayes, R. M. Lopes, K. L. Lorenz, K. L. Mitchell, J. Radebaugh, F. Paganelli, L. A. Soderblom, E. R. Stofan, C. A. Wood, S. D. Wall, and the Cassini Radar Team. High resolution topographic models of Titan's surface derived by radar stereogrammetry with a rigorous sensor model. Icarus, 112, submitted.

B. Klinkenberg and M. F. Goodchild. The fractal properties of topography: A comparison of methods. Earth Surface Processes and Landforms, 17, 1992. doi: 10.1002/esp.3290170303.

J. Korcak. Deux Types Fondamentaux de Distribution Statistique. Bulletin de l'Institut International de Statistique, 30:295–299, 1940.

G. P. Kuiper. Titan: a satellite with an atmosphere. The Astrophysical Journal, 100, November 1944. doi: 10.1086/144679.

A. Le Gall, M. A. Janssen, P. Paillou, R. D. Lorenz, S. D. Wall, and the Cassini Radar

Team. Radar-bright channels on Titan. Icarus, 207:948–958, June 2010. doi: 10.1016/j.icarus.2009.12.027.

K. Levenberg. A Method for the Solution of Certain Problems in Least-Squares. Quarterly Applied Math, 2:164–168, 1944.

G. F. Lindal, G. E. Wood, H. B. Hotz, D. N. Sweetnam, V. R. Eshleman, and G. L. Tyler. The atmosphere of Titan - an analysis of the Voyager 1 radio occultation measurements. Icarus, 53:348–363, February 1983. doi: 10.1016/0019-1035(83)90155-0.

R. M. C. Lopes, E. R. Stofan, R. Peckyno, J. Radebaugh, K. L. Mitchell, G. Mitri, C. A. Wood, R. L. Kirk, S. D. Wall, J. I. Lunine, A. Hayes, R. Lorenz, T. Farr, L. Wye, J. Craig, R. J. Ollerenshaw, M. Janssen, A. Legall, F. Paganelli, R. West, B. Stiles, P. Callahan, Y. Anderson, P. Valora, L. Soderblom, and Cassini RADAR Team. Distribution and interplay of geologic processes on Titan from Cassini radar data. Icarus, 205:540–558, February 2010. doi: 10.1016/j.icarus.2009.08.010.

R. D. Lorenz. The life, death and afterlife of a raindrop on Titan. Planetary and Space Science, 41:647–655, September 1993. doi: 10.1016/0032-0633(93)90048-7.

R. D. Lorenz. Crater lakes on Titan: Rings, horseshoes and bullseyes. Planetary and Space Sciences, 42:1–4, January 1994. doi: 10.1016/0032-0633(94)90134-1.

R. D. Lorenz. Thermal interactions of the Huygens probe with the Titan environment: Constraint on near-surface wind. Icarus, 182:559–566, June 2006. doi: 10.1016/j.icarus.2006.01.009.

R. D. Lorenz, H. B. Niemann, D. N. Harpold, S. H. Way, and J. C. Zarnecki. Titan's damp ground: Constraints on Titan surface thermal properties from the temperature evolution of the Huygens GCMS inlet. Meteoritics and Planetary Science, 41:1705–1714, November 2006.

R. D. Lorenz, B. Jackson, and A. Hayes. Racetrack and Bonnie Claire: southwestern US playa lakes as analogs for Ontario Lacus, Titan. Planetary and Space Science, 58:724–731, March 2010a. doi: 10.1016/j.pss.2009.05.012.

R. D. Lorenz, C. Newman, and J. I. Lunine. Threshold of wave generation on Titan's lakes and seas: Effect of viscosity and implications for Cassini observations. Icarus, 207: 932–937, June 2010b. doi: 10.1016/j.icarus.2009.12.004.

J. I. Lunine. Does Titan have an ocean? A review of current understanding of Titan's surface. Reviews of Geophysics, 31:133–149, May 1993. doi: 10.1029/92RG02794.

J. I. Lunine, D. J. Stevenson, and Y. L. Yung. Ethane ocean on Titan. Science, 222:1229–1230, December 1983. doi: 10.1126/science.222.4629.1229.

B. Mandelbrot. How Long Is the Coast of Britain? Statistical Self-Similarity and Fractional Dimension. Science, 156:636–638, May 1967. doi: 10.1126/science.156.3775.636.

B. B. Mandelbrot. The fractal geometry of nature. San Francisco: W.H. Freeman, 1982, Revised edition of: Fractals (1977), 1977.

B. B. Mandelbrot and C. Mulvey. Book-Review - Fractals: Form Chance and Dimension. The Observatory, 100:13, February 1980.

B. B. Mandelbrot and J. A. Wheeler. The Fractal Geometry of Nature. American Journal of Physics, 51:286–287, March 1983. doi: 10.1119/1.13295.

D. Marquardt. An Algorithm For Least-Sqaures Estimation of Nonlinear Parameters. SIAM Journal Applied Math, 11:431–444, 1963.

J. L. Mitchell. The drying of Titan's dunes: Titan's methane hydrology and its impact on atmospheric circulation. Journal of Geophysical Research (Planets), 113(E12):E8015:1–22, August 2008. doi: 10.1029/2007JE003017.

K. L. Mitchell, E. R. Stofan, J. Radebaugh, P. H. Paillou, A. G. Hayes, R.L. Lopes, M.A. Janssen, P.S. Callahan, R.D. Lorenz, J.L. Lunine, O. Aharonson, and the Cassini Radar Team. Titan's North Polar Lake District: Insights From the Cassini Titan Radar Mapper. Icarus, in preparation.

G. Mitri, A. P. Showman, J. I. Lunine, and R. D. Lorenz. Hydrocarbon lakes on Titan. Icarus, 186:385–394, February 2007. doi: 10.1016/j.icarus.2006.09.004.

D. O. Muhleman. Earth-based remote sensing of solar system objects. Reviews of Geophysics, 33:477–480, 1995. doi: 10.1029/95RG00555.

C. D. Murray and S. F. Dermott. Solar system dynamics. Cambridge University Press, 1999.

C. E. Newman, M. I. Richardson, C. Lee, A. D. Toigo, and S. P. Ewald. The TitanWRF Model at the end of the Cassini Prime Mission. AGU Fall Meeting Abstracts, page A2, December 2008.

C. Newmann and M. Richardson. personal communication, 2009.

S. J. Ostro, D. B. Campbell, R. A. Simpson, R. S. Hudson, J. F. Chandler, K. D. Rosema, I. I. Shapiro, E. M. Standish, R. Winkler, D. K. Yeomans, R. Velez, and R. M. Goldstein. Europa, Ganymede, and Callisto: New radar results from Arecibo and Goldstone. Journal of Geophysical Research, 97:18277–18244, November 1992.

S. J. Ostro, R. D. West, M. A. Janssen, R. D. Lorenz, H. A. Zebker, G. J. Black, J. I. Lunine, L. C. Wye, R. M. Lopes, S. D. Wall, C. Elachi, L. Roth, S. Hensley, K. Kelleher, G. A. Hamilton, Y. Gim, Y. Z. Anderson, R. A. Boehmer, W. T. K. Johnson, and the Cassini RADAR Team. Cassini RADAR observations of Enceladus, Tethys, Dione, Rhea, Iapetus, Hyperion, and Phoebe. Icarus, 183:479–490, August 2006. doi: 10.1016/j.icarus.2006.02.019.

P. Paillou, M. Crapeau, C. Elachi, S. Wall, and P. Encrenaz. Models of synthetic aperture radar backscattering for bright flows and dark spots on Titan. Journal of Geophysical Research (Planets), 111(E10):E11011:1–6, November 2006. doi: 10.1029/2006JE002724.

P. Paillou, J. Lunine, G. Ruffié, P. Encrenaz, S. Wall, R. Lorenz, and M. Janssen. Microwave dielectric constant of Titan-relevant materials. Geophysical Research Letters, 35:L18202:1–4, September 2008a. doi: 10.1029/2008GL035216.

P. Paillou, K. Mitchell, S. Wall, G. Ruffié, C. Wood, R. Lorenz, E. Stofan, J. Lunine, R. Lopes, and P. Encrenaz. Microwave dielectric constant of liquid hydrocarbons: Application to the depth estimation of Titan's lakes. Geophysical Research Letters, 35: L05202:1–5, March 2008b. doi: 10.1029/2007GL032515.

Jonathan D. Phillips. Spatial analysis of shoreline erosion, delaware bay, new jersey. Annals of the Association of American Geographers, 76(1):50–62, 1986. ISSN 00045608. URL `http://www.jstor.org/stable/2562872`.

W. J. Pierson, Jr. and L. Moskowitz. A Proposed Spectral Form for Fully Developed Wind Seas Based on the Similarity Theory of S. A. Kitaigorodskii. Journal of Geophysical Research, 69:5181–5190, December 1964. doi: 10.1029/JZ069i024p05181.

J. B. Pollack and J. N. Cuzzi. Scattering by nonspherical particles of size comparable to wavelength - A new semi-empirical theory and its application to tropospheric aerosols. Journal of Atmospheric Sciences, 37:868–881, 1980. doi: 10.1175/1520-0469(1980) 037.

William Press, Brian Flannery, Saul Teukolsky, and William Vetterling. Numerical Recipes in C: The Art of Scientific Computing. Cambridge University Press, oct 1992. ISBN 0521431085.

S. O. Rice. Small Perturbation Method. Commun.Pure Applied Math, 4:251–378, 1951.

M. Richardson, A. Toigo, and Newman C. PlanetWRF: A general purpose, local to global numerical model for planetary atmospheric and climate dynamics. Journal of Geophysical Research, 112:E09001:1–29, 2007.

E. J. Rignot, S. J. Ostro, J. J. van Zyl, and K. C. Jezek. Unusual Radar Echoes from the Greenland Ice Sheet. Science, 261:1710–1713, September 1993.

S. O. Saravanapavan. Molecular Diffusivity. Commun.Pure Applied Math, 4:251–378, 2000.

Dietmar Saupe. Algorithms for random fractals. In The Science of Fractal Images, pages 71–113. Springer-Verlag New York, Inc., 1988.

Reed A. Schwimmer. A temporal geometric analysis of eroding marsh shorelines: Can fractal dimensions be related to process? Journal of Coastal Research, 24(1):152–158, January 2008. ISSN 0749-0208. URL `http://dx.doi.org/10.2112/06-0644.1`.

A. D. Sen, V. G. Anicich, and T. Arakelian. Dielectric constant of liquid alkanes and hydrocarbon mixtures. Journal of Applied Physics, 25:512–521, 1992.

P. Sharma and S. Byrne. Constraints on Titan's Topography Through Fractal Analysis of Shorelines. In Lunar and Planetary Institute Science Conference Abstracts, volume 39 of Lunar and Planetary Institute Science Conference Abstracts, page 2145, March 2008.

P. Sharma and S. Byrne. Constraints on Titan's topography through fractal analysis of shorelines. Icarus, 209:723–737, October 2010. doi: 10.1016/j.icarus.2010.04.023.

R. A. Simpson and G. L. Tyler. Radar scattering laws for the lunar surface. IEEE Transactions on Antennas and Propagation, 30:438–449, May 1982. doi: 10.1109/TAP.1982.1142803.

B. A. Smith, L. Soderblom, R. F. Beebe, J. M. Boyce, G. Briggs, A. Bunker, S. A. Collins, C. Hansen, T. V. Johnson, J. L. Mitchell, R. J. Terrile, M. H. Carr, A. F. Cook, J. N. Cuzzi, J. B. Pollack, G. E. Danielson, A. P. Ingersoll, M. E. Davies, G. E. Hunt, H. Masursky, E. M. Shoemaker, D. Morrison, T. Owen, C. Sagan, J. Veverka, R. Strom, and V. E. Suomi. Encounter with Saturn - Voyager 1 imaging science results. Science, 212:163–191, April 1981. doi: 10.1126/science.212.4491.163.

J. C. Sola. La sincérité scientifique. Annals of the Observatory of Lucien Libert, 18:51–53, December 1904.

B. W. Stiles, S. Hensley, Y. Gim, D. M. Bates, R. L. Kirk, A. Hayes, J. Radebaugh, R. D. Lorenz, K. L. Mitchell, P. S. Callahan, H. Zebker, W. T. K. Johnson, S. D. Wall, J. I. Lunine, C. A. Wood, M. Janssen, F. Pelletier, R. D. West, C. Veeramacheneni, and the Cassini RADAR Team. Determining Titan surface topography from Cassini SAR data. Icarus, 202:584–598, August 2009. doi: 10.1016/j.icarus.2009.03.032.

E. R. Stofan, C. Elachi, J. I. Lunine, R. D. Lorenz, B. Stiles, K. L. Mitchell, S. Ostro, L. Soderblom, C. Wood, H. Zebker, S. Wall, M. Janssen, R. Kirk, R. Lopes, F. Paganelli, J. Radebaugh, L. Wye, Y. Anderson, M. Allison, R. Boehmer, P. Callahan, P. Encrenaz, E. Flamini, G. Francescetti, Y. Gim, G. Hamilton, S. Hensley, W. T. K. Johnson, K. Kelleher, D. Muhleman, P. Paillou, G. Picardi, F. Posa, L. Roth, R. Seu, S. Shaffer, S. Vetrella, and R. West. The lakes of Titan. Nature, 445:61–64, January 2007a. doi: 10.1038/nature05438.

E. R. Stofan, C. Elachi, J. I. Lunine, R. D. Lorenz, B. Stiles, K. L. Mitchell, S. Ostro,

L. Soderblom, C. Wood, H. Zebker, S. Wall, M. Janssen, R. Kirk, R. Lopes, F. Paganelli, J. Radebaugh, L. Wye, Y. Anderson, M. Allison, R. Boehmer, P. Callahan, P. Encrenaz, E. Flamini, G. Francescetti, Y. Gim, G. Hamilton, S. Hensley, W. T. K. Johnson, K. Kelleher, D. Muhleman, P. Paillou, G. Picardi, F. Posa, L. Roth, R. Seu, S. Shaffer, S. Vetrella, and R. West. The lakes of Titan. Nature, 445:61–64, January 2007b. doi: 10.1038/nature05438.

E. R. Stofan, C. Elachi, J. I. Lunine, R. D. Lorenz, R. L. Kirk, R. M. C. Lopes, C. A. Wood, J. Radebaugh, S. D. Wall, K. L. Mitchell, L. A. Soderblom, P. Paillou, T. Farr, B. Stiles, P. Callahan, and Cassini Radar Team. Varied Geologic Terrains at Titan's South Pole: First Results from T39. In Lunar and Planetary Institute Science Conference Abstracts, volume 39 of Lunar and Planetary Institute Science Conference Abstracts, page 1491, March 2008.

A. K. Sultan-Salem and G. L. Tyler. Generalized fractal-based laws for scattering from planetary surfaces: A unifying scale-explicit paradigm. Journal of Geophysical Research (Planets), 111:E06S08:1–6, April 2006. doi: 10.1029/2005JE002540.

W. R. Thompson and S. W. Squyres. Titan and other icy satellites - Dielectric properties of constituent materials and implications for radar sounding. Icarus, 86:336–354, August 1990. doi: 10.1016/0019-1035(90)90224-W.

T. Tokano. Limnological Structure of Titan's Hydrocarbon Lakes and Its Astrobiological Implication. Astrobiology, 9:147–164, March 2009a. doi: 10.1089/ast.2007.0220.

T. Tokano. Impact of seas/lakes on polar meteorology of Titan: Simulation by a coupled

GCM-Sea model. Icarus, 204:619–636, December 2009b. doi: 10.1016/j.icarus.2009.07.032.

M. G. Tomasko, B. Archinal, T. Becker, B. Bézard, M. Bushroe, M. Combes, D. Cook, A. Coustenis, C. de Bergh, L. E. Dafoe, L. Doose, S. Douté, A. Eibl, S. Engel, F. Gliem, B. Grieger, K. Holso, E. Howington-Kraus, E. Karkoschka, H. U. Keller, R. Kirk, R. Kramm, M. Küppers, P. Lanagan, E. Lellouch, M. Lemmon, J. Lunine, E. McFarlane, J. Moores, G. M. Prout, B. Rizk, M. Rosiek, P. Rueffer, S. E. Schröder, B. Schmitt, C. See, P. Smith, L. Soderblom, N. Thomas, and R. West. Rain, winds and haze during the Huygens probe's descent to Titan's surface. Nature, 438:765–778, December 2005. doi: 10.1038/nature04126.

DL Turcotte. Fractals and chaos in geology and geophysics. Cambridge Univ Pr, 1997.

E. P. Turtle, J. E. Perry, A. S. McEwen, A. D. DelGenio, J. Barbara, R. A. West, D. D. Dawson, and C. C. Porco. Cassini imaging of Titan's high-latitude lakes, clouds, and south-polar surface changes. Geophysical Research Letters, 36:L2204:1–6, January 2009a. doi: 10.1029/2008GL036186.

E. P. Turtle, J. E. Perry, A. S. McEwen, A. D. DelGenio, J. Barbara, R. A. West, and A. G. Hayes. Seasonal changes in Titan's meteorology and surface features. American Geophysical Union, 2009b.

E. P. Turtle, J. E. Perry, A. G. Hayes, and A. S. McEwen. Shoreline Retreat at Titan's Ontario Lacus and Arrakis Planitia from Cassini Imaging Science Subsystem Observations. Icarus, 2011. doi: 10.1016/j.icarus.2011.02.005.

G. L. Tyler, R. A. Simpson, M. J. Maurer, and E. Holmann. Scattering properties of the Venusian surface - Preliminary results from Magellan. Journal Of Geophysical Research, 97:13,115–139, August 1992.

F. T. Ulaby, R. K. Moore, and A. K. Fung. Microwave Remote Sensing: Active and Passive, Vol. 2 by F. T. Ulaby. Artech House, Norwood, Mass., 1982.

Coastal & Marine Geology (CMG) USGS. Multibeam mapping of lake tahoe, california-nevada from field activity: L-1-98-lt. Technical report, United States Geological Survey, 2001.

B. Ventura, C. Notarnicola, D. Casarano, M. Janssen, and F. Posa. Characterization of Titan surface scenarios combining Cassini SAR images and radiometry data. European Geophysical Union, 2009.

S. Wall, A. Hayes, C. Bristow, R. Lorenz, E. Stofan, J. Lunine, A. Le Gall, M. Janssen, R. Lopes, L. Wye, L. Soderblom, P. Paillou, O. Aharonson, H. Zebker, T. Farr, G. Mitri, R. Kirk, K. Mitchell, C. Notarnicola, D. Casarano, and B. Ventura. Active shoreline of Ontario Lacus, Titan: A morphological study of the lake and its surroundings. Geophysical Research Letters, 37:L5202:1–5, March 2010. doi: 10.1029/2009GL041821.

J. Waples, R. Paddock, J. Janssen, D. Lovalvo, B. Schulze, J. Kaster, and J. Klump. High resolution bathymetry and lakebed characterization in the nearshore of western lake michigan. Journal of Great Lakes Research, 31:64–74, 2005.

R. D. West, Y. Anderson, R. Boehmer, O. Bombaci, L. Borgarelli, P. Callahan, C. Elachi, Y. Gim, G. Hamilton, S. Hensley, M. Janssen, W. T. K. Johnson, K. Kelleher, S. Ostro, L. Roth, S. Shaffer, S. Stiles, B. Wall, L. Wye, and H. Zebker. Cassini RADAR sequence planning and instrument performance. IEEE Trans. Geosci. Remote Sensing, pages 1777–1795, February 2008. doi: 10.1109/TGARS.2008.2007217.

J. W. Wright. A New Model For Sea Clutter. IEEE Trans. Antennas Propagat., 16:217–223, 1968.

L. C. Wye, H. A. Zebker, S. J. Ostro, R. D. West, Y. Gim, R. D. Lorenz, and The Cassini Radar Team. Electrical properties of Titan's surface from Cassini RADAR scatterometer measurements. Icarus, 188:367–385, June 2007. doi: 10.1016/j.icarus.2006.12.008.

L. C. Wye, H. A. Zebker, R. M. Lopes, R. Peckyno, A. Le Gall, and M. A. Janssen. Surface Parameters of Titan Feature Classes From Cassini RADAR Backscatter Measurements. AGU Fall Meeting Abstracts, page A1318, December 2008.

L. C. Wye, H. A. Zebker, and R. D. Lorenz. Smoothness of Titan's Ontario Lacus: Constraints from Cassini RADAR specular reflection data. Geophysical Research Letters, 36:L16201:1–5, August 2009. doi: 10.1029/2009GL039588.

Y. L. Yung, M. Allen, and J. P. Pinto. Photochemistry of the atmosphere of Titan - Comparison between model and observations. Astrophysics Journal, 55:465–506, July 1984. doi: 10.1086/190963.

J. C. Zarnecki, M. R. Leese, B. Hathi, A. J. Ball, A. Hagermann, M. C. Towner, R. D. Lorenz, J. A. M. McDonnell, S. F. Green, M. R. Patel, T. J. Ringrose, P. D. Rosenberg,

K. R. Atkinson, M. D. Paton, M. Banaszkiewicz, B. C. Clark, F. Ferri, M. Fulchignoni, N. A. L. Ghafoor, G. Kargl, H. Svedhem, J. Delderfield, M. Grande, D. J. Parker, P. G. Challenor, and J. E. Geake. A soft solid surface on Titan as revealed by the Huygens Surface Science Package. Nature, 438:792–795, December 2005. doi: 10.1038/nature04211.

H. A. Zebker, B. Stiles, S. Hensley, R. Lorenz, R. L. Kirk, and J. Lunine. Size and Shape of Saturn's Moon Titan. Science, 324:921–923, May 2009. doi: 10.1126/science.1168905.

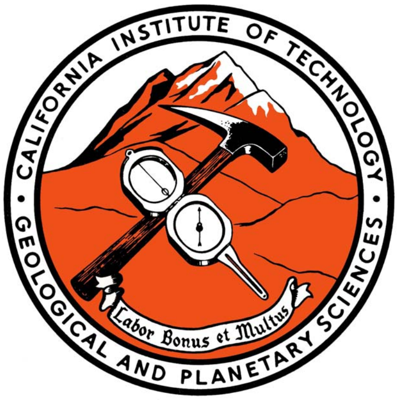
CALIFORNIA INSTITUTE OF TECHNOLOGY
GEOLOGICAL AND PLANETARY SCIENCES
Labor Bonus et Multus

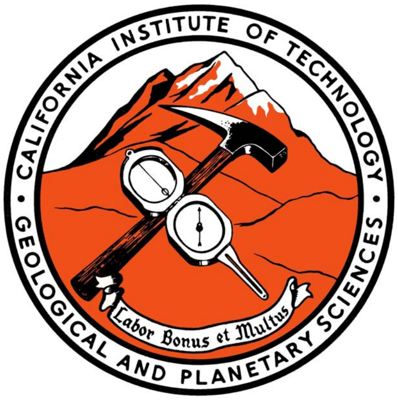
CALIFORNIA INSTITUTE OF TECHNOLOGY
GEOLOGICAL AND PLANETARY SCIENCES
Labor Bonus et Multus